Some Statistics for Combining Radiosonde Soundings with Satellite Images for Estimating Rainfall

A Final Report for

NOAA Contract NA-80-SAC-00721

Development of Techniques for Estimating Precipitation in Agricultural Areas

Donald P. Wylie
Space Science and Engineering Center
The University of Wisconsin-Madison
1225 West Dayton Street
Madison, Wisconsin 53706

May 1982

Summary

Thirteen parameters measured by radiosonde soundings, the hourly Service-A network, or the satellite images themselves, were collected over a one year period and studied as sources of information that could be used to help satellite techniques estimate rain rates. The intent was to collect a body of statistics that could be used for combining the *in situ* weather data available from radiosondes and surface observations with satellite imagery for making rain estimations. The most useful parameters tested were the vertically integrated precipitable water vapor from radiosondes, the cloud top temperature or height from satellite infrared images, the cloud top brightness from satellite visible images, and the moisture convergence from the surface observations.

Statistically significant correlations with the six hour rainfall reports were found indicating that some information is available from these data. However, a large scatter in the rain reports also was present. The reason is that the parameters were measured on the synoptic scale and the smaller scale dynamics of the clouds were not monitored or explained. Thus, these parameters can be useful for estimating broad changes in rain rates caused by changes in air masses but they cannot describe the full details of cloud development and their rain intensity. Other measurements of convective intensity are needed. Anvil expansion measurements used with the radionsonde data is suggested for the intense storm systems.

Satellite infrared sounding estimates of precipitable water vapor were compared to radiosonde measurements on two days over the United States. The satellite products produced patterns similar to the radiosondes but under estimated the moist areas by 25% and over estimated the dry areas. These products could be useful if the biases were understood so that they could be removed.

For the strong storm systems with large anvils, we found that the rain areas were from 10 to 25% of the cloud area. Heavy rain covered 1 to 5% of the cloud area.

1. Introduction

Most experiments in using satellite visible and infrared imagery for estimating rainfall were developed in the tropics and were targeted for regional programs such as hydrological studies (Barrett, 1976), the GATE program (Giffith et al., 1978, Woodley et al., 1980, and Stout et al., 1979) and the interannual variability of the Intertropical Convergence Zone (Kilonsky and Ramage, 1976). Outside of the tropics, lower rainfall rates were found and adjustments had to be made to make these techniques work.

The most popular method of adjusting rain rates has been to compare radiosonde soundings from the region where the rain estimation technique was developed with soundings taken in the new area where rain estimates are being made (Wylie, 1979, and Griffith et al., 1981). The sounding comparison has usually been made by running the cloud model of Simpson and Wiggert (1969) to stimulate the differences in cloud precipitation production between the two areas. It has also been used to account for the daily changes in the air masses that reside in mid-latitude areas.

The main reason for using the model and sounding data has been the need for more information on the probable rain rates of clouds. The visible and infrared imagery can locate raining clouds but they give little information on rain rates. The wavelengths used respond to all sizes of droplets, both the precipitating droplets and the smaller non-precipitating cloud droplets. Rain rate information has been indirectly inferred by a variety of methods such as following the life history of the cloud, the rate of cirrus anvil growth, or by a meteorologist subjectively judging the convective intensities from an "eyeball" examination of the satellite pictures.

To search for other information that may be used for inferring rain rates, we collected data on 13 parameters measured by radiosondes or the surface service-A network. All of these have been related to cloud growth or severe storms in the past. They are as follows:

1) the vertically integrated precipitable water vapor,
2) the parcel stability lifted index,
3) the height of the highest cloud top,
4) the temperature advection at three levels, 700 mb, 850 mb, and the ground level,
5) the 500 mb vorticity advection,
6) the wind field convergence at the ground level,
7) the moisture convergence (ground level),
8) the vertical wind shear (sfc-500 mb),
9) the condensation estimated from a simple one-dimensional bubble model, and
10) the cloud top temperature and brightness measured on the satellite images.

We collected these parameters daily in areas where rain occurred. In the next section the rainfall amounts will be discussed to illustrate how some of these parameters can be used to improve satellite-based techniques.

Also of interest is the question "Can these parameters be measured from satellite-based sensors?" The two most useful parameters are the precipitable water vapor and cloud top height or temperature measurements. The cloud top temperature can be extracted from satellite infrared imagery. To see if precipitable water information could be extracted from the satellite infrared soundings, two analyses were made over the United States

and compared to the radiosonde derived fields. The comparison is discussed in Section 2.

Equal in importance to estimating rain rates, is estimating the area of the rain. Cirrus cloud cover often extends far beyond the areas of rain and thus satellite schemes based on cloud top temperature may overestimate the area of the rain. To gather some information on the magnitude of this problem, radar echo areas were compared to satellite measured cloud areas on four strong convective storms in Oklahoma. The results of this comparison are discussed in Section 3.

Finally, as a carry-over from a previous program, a paper was written describing a rain estimation technique for severe storms. A preprint of this paper, "An Estimation of the Condensation Rates in Three Severe Storm Systems from Satellite Observations of the Convective Mass Flux," (Monthly Weather Review) is enclosed in the appendix. It discusses an extension of the Sikdar (1970) technique of measuring the rate of expansion of the cirrus anvils seen on satellite images. This paper describes a diagnostic model that uses the anvil expansion rate measured from satellite pictures to calculate the vertical mass flux and water budgets of the storm system. It combines satellite measurements with the vertical moisture profiles from radiosonde data to describe the dynamics of the cloud system. It is only applicable to cloud systems where expanding anvils are seen on satellite images. For summer convection, a large number of these anvils can typically be seen and it could provide a great deal of information especially where heavy rains occur.

2. Rain rate estimation

Most rain estimation experiments have been limited in the number of days they studied because of the problems in obtaining archived data and manipulating it into useable formats. To keep this study from being bound by the same handicap, we used the data accessed in real-time by our McIDAS, obtaining data from a wide range of weather situations.

a. Area examined

Rain events in the Great Plains and Mid-Western areas of the United States were selected from the archived data from 27 February 1981 through 4 January 1982. The number of days examined at each radiosonde station is shown in Figure 1.

On each day we obtained the precipitation totals reported by the service-A network from 12Z - 18Z. These data were used as a measure of rain rates. We were aware that the spacing of these stations was inadequate for resolving single rain cells. Had we chosen to use a local rain gauge network or radar cite, the number and variety of situations would have been severely limited. By using a large area of the United States, we usually found some precipitation each day.

In past studies the majority of our time was spent in preparing the radar data while time spent studying satellite imagery has been only a minority of the total effort. By using the McIDAS data base we were able to concentrate on the parameters of interest, spending only a small fraction of our time on quality control of the precipitation data.

b. Rain measurements

We knew that the service-A network would miss the small cell precipitation, so we restricted our data gathering to areas where large-scale cloud cover occurred, and where the gauge reports agreed within 20%. The intent was to focus on areas where the precipitation was widespread so that the service-A reports were representative of what occurred. Further, we concentrated on the reports of heavier rain ignoring the lighter reports on the fringes of the rain area.

c. Variables compared to rain rates

The 13 parameters compared to the rainfall measurements are summarized in Table 1. Most of these parameters have been indicated by past studies as having some relationship to rainfall rates, although few of these studies have made quantitative attempts to do so. This is the case for the vertically integrated precipitable water vapor (PW), the cloud top temperature or height, the cloud top brightness, moisture convergence, and the bubble model. Other parameters have been used for predicting of severe storms such as the lifted index and the vertical wind shear. Temperature advection and 500 mb positive vorticity advection (commonly called PVA) were added because they are used to predict cloud growth by weather forecasters.

In picking storms for study on rain-days, preference was given to areas between the Rocky Mountains and the Mississippi River. On occassion, data also were taken from Illinois, Ohio, Indiana, Tennessee, Louisiana, and Mississippi east of the river when heavy rains moved into those states.

The morning period 12-18Z was choosen for two reasons. At local noon (18Z) the cloud brightness on the visible image could be used. This period also avoided the cellular cumulonimbus clouds (Cb) that develop in the afternoon due to surface heating. As mentioned previously, it was obvious that the service-A network could not adequately sample isolated Cb rainfall.

Once suitable precipitation areas were found, the second step was to look for the clouds that made the precipitation on a sequence of satellite images. The coldest cloud top temperature and the maximum visible brightness (local noon brightness) for the clouds were measured.

The radiosonde station nearest the rain gauge report also was selected for extracting the lifted index, precipitable water (PW), cloud top height and temperature, the vertical wind shear (500 mb - sfc), and for running the bubble model. The lifted index was calculated in a similar manner to the National Weather Service. The average potential temperature and mixing ratio over the lowest 100 mb were used to define the Lifting Condensation Level (LCL). The parcel then was allowed to ascent adiabatically from the LCL to 500 mb where the temperature difference between the parcel and the sounding defined the index. A negative value indicates unstable conditions. The afternoon surface temperature was predicted from the potential temperature 100 mb above the surface assuming surface heating throughout the day and a well mixed boudary layer. This is very similar to the method used by the National Weather Service.

The bubble model used on McIDAS was similar to the Simpson and Wiggert (1969) model. It simulated a buoyant bubble that started from the LCL and rose to a level where it lost its vertical momentum. The vertical velocity was calculated at 10 mb intervals from the buoyancy of the bubble due to

its temperature difference from the sounding. No effects of liquid water weight were included in the velocity calculation. The rain parameter for the model was the condensation calculated from a budget of the moisture entering the bubble and the temperature change of the bubble as it ascended. No special calculations were made for nucleation processes or liquid water storage by the bubble. Ambient air was entrained into the bubble at the rate of 100% of mass increase per 400 mb ascent in the buoyancy and condensation calculations. This is the same procedure used by Park and Sikdar (1980) and Mack and Wylie (1982, also Appendix).

The condensation calculation was expressed in terms of grams of condensed water per Kg of air at the cloud base density. This unit was choosen because all calculations made were referenced to the starting unit mass of the bubble at cloud base as in the Simpson-Wiggert model. A conversion to grams of water per unit area could have been obtained by multiplying by the air density. But this step was unnecessary because the condensation has been used to compare model runs made on different soundings (Griffith et al., 1981, and Wylie, 1979) for changes in rain rates. It does not simulate the cloud dynamics with enough sophistication to predict the magnitude of the rainfall. This is because real clouds are made of many bubbles or updrafts of different sizes. We used this model to predict trends in rain rates from the changes in the temperature and humidity vertical structures.

In many cases the bubble would not freely ascend in the model because of the stable temperature structure. When the only stable part of the sounding was a surface inversion, the bubble was manually started at the top of the inversion. This manual interaction allowed the model to run but at the price of not including the air inside the inversion in the

condensation calculation. On many soundings stable conditions existed in the lower atmosphere with several inversions. Thus, we felt the bubble did not adequately simulate the clouds because the boundary layer moisture was ignored. The clouds, on the other hand, may have drawn some of this moisture into their updrafts.

A second problem was middle atmosphere stable layers. For the runs where the bubble stopped short of the tropopause, no corrections or adjustments were made. We considered changing the entrainment rate of mid-level air so that the bubble would stop at the same level as the cloud top temperature, but there are other variables such as starting level and initial velocity which also could be varied. In addition, many of the cloud top temperatures were warmer than the tropopause on soundings where no upper level stable layers existed. Given all these variables and possible situations, we decided not to complicate the model runs and used the most natural conditions. Since most of the moisture is in the lower atmosphere, little additional condensation would have been gained by extending the altitude of the bubble once it passed 500 mb.

Wind field convergence, moisture convergence and temperature advection were calculated from objective analyses of the radiosonde and service-A data. Analyses of the wind, mixing ratio, and temperature fields were made on uniform grids of 3° of latitude and longitude resolution over the United States. For the 700 and 850 mb temperature advection, the 12Z soundings were used while the 18Z service-A observations were used for the surface calculations.

A weighted sum of all observations at the same level was used to form each grid point value. The weighting function was gaussian in shape with a 50% or less relative weight given to observations over one grid point in

distance. This, in effect, was similar to the Low Pass Filter method of Barnes (1964).

d. Seasonal trends

The six-hour rain measurements exhibited some annual variation (Figure 2) as expected. Two extremely heavy events, where more than 2" fell, were found in the fall on 13 October. This occurred because of a stationary front in the Mississippi Valley which had a strong convergence of moisture for over 24 hours. We did not take data from the strong storm systems in July unless the rain was of a wide spread nature. Since Cb rainfall commonly occurred during the summer very few days were found that we could use. Thus, we chose to ignore the heavy rain events during the summer and the seasonal change in rain rates shown in Figure 1 is not indicative of all the rain that occurred in the central United States. The anvil expansion method listed in the appendix is more applicable to Cb rains because it includes a measurement of the cloud vertical motion intensity along with the environmental conditions.

Like rain, precipitable water measurements exhibited a large seasonal cycle (Figure 3). Values as low as 0.01" were found in December and January while in the summer 1.9" were recorded. The scatter in this parameter reflects the larger differences between air masses that occurred over the United States. These air mass differences have to be accounted for in order for any rain estimation scheme to work in this area or any other mid-latitude location.

Also showing a seasonal cycle were the lifted index (Figure 4), the cloud top temperature (Figure 5), and the cloud top height (Figure 6). The unstable lifted indicies (-) were primarily found in the summer while the

strongly stable indicies (+) were found in the fall and winter months. Seasonal trends in the cloud top temperatures, though present, were not as pronounced as the other variables. The coldest temperatures ranged from 220 K during December to 201 K in September. Cloud top heights, derived from temperatures, more clearly show the seasonal changes.

The large seasonal variation in cloud top brightness (Figure 7) were caused by two factors. One was higher clouds during the summer and fall, presumably associated with higher liquid water concentrations. The second was the seasonal change in the zenith angle of the sun. No correction for sun angle changes were made in Figure 7 because most brightness normalization schemes use radiative scattering theory for flat homogenous clouds. The brightest spot on convective clouds often is the side of a tower protruding above the cirrus cloud mass. Most brightness normalization schemes are marginally applicable to this situation. The effects of the higher liquid water concentrations on the cloud brightness, however, appear to be stronger than the sun angle changes. For example, the highest brightness values were found in September and October when the sun was near the equinox position.

The condensation estimated by the bubble model also showed a small seasonal change (Figure 8). In the spring the model estimated very small condensation quantity because the soundings were either stable or the bubble had to be started above a deep inversion. Both conditions inhibited a free ascent of the bubble as previously discussed. The highest model estimates were made on the unstable soundings. In the late fall and winter months no model runs were made because of the predominance of stable soundings.

No seasonal changes were obvious for the other parameters measured; temperature advection (Figure 9), moisture convergence (Figure 10), or the vertical wind shear (Figure 11).

e. Relationship to rain rates

Nine of the parameters tested had significant correlations with the six-hour rainfall reports (Table 1) according to the F-test in Panofsky and Brier (1968, p. 92.). The highest correlations were the precipitable water vapor, the cloud top temperature and height, the cloud top brightness, and the moisture convergence. The F ratios also are shown in Table 1. The first five parameters easily passed the F-test with coefficients from 0.35 to 0.48. Smaller correlations were found for the bubble model, vorticity advection, lifted index, and the 700 mb temperature advection. The advection at other levels, the wind convergence, and the vertical shear did not correlate with the precipitation reports.

Scatter plots of these variables (Figs. 12-22), in the order listed in Table 1) show some relationship with rain reports mainly for the heavy reports. The heaviest rain reports (>1.5") occurred with unstable soundings that had high PW values. High values of moisture convergence and temperature advection also were present. The satellite images indicated cold, high and bright cloud tops as expected. But for the same values of each parameter, many light rain reports also were found. Thus, the parameters can indicate probable heavy rain events but can not guarantee its magnitude.

A search for the best combination of parameters for estimating rain rates was made using the Biomedical Computer Program (1977) package developed by the University of California at Los Angeles. The best

predictors found were the PW, cloud top temperature (CT), and the moisture convergence (QC). The others that correlated with rain reports were rejected as predictors because they also correlated some of the other predictors. For example, the cloud top brightness, which was second best on the list (Table 1), also correlated with PW (0.67), cloud top height (-0.53), lifted index (-0.43) and cloud top temperature (-0.38). The cloud top height, which was third on the list, correlated very well with the temperture (0.93) since it was used in deriving the height and also with PW (-0.52). Thus, only one of the satellite measurements were needed and the addition of the other two did not add any additional information. The best regression for estimating rain rates was

$$\text{6 Hour Rain (inches)} = 1.0242 + 0.380\ \text{PW} - 0.0304\ \text{QC} - 0.0047\ \text{CT}. \quad (1)$$

Estimates of rain were made using the regression and compared to the rain reports (Figure 23). A reasonable correlation of 0.60 was found. The regression predicted the general trend in the rain reports for most of the cases but it under predicted the heaviest rain reports. This was expected since these extremely heavy rains did not occur with any comparable anomalies in the measured parameters.

For two parameters a regression of

$$\text{Rain} = -0.1047 + 0.429\ \text{PW} - 0.0330\ \text{QC} \quad (2)$$

was found which fit the rain reports with a correlation of 0.58.

For single parameters the following regressions were derived:

$$\text{Rain} = -0.05 + 0.44\ \text{PW} \tag{3}$$

$$\text{Rain} = 0.2 - 0.04\ \text{QC} \tag{4}$$

$$\text{Rain} = 2.10 - 0.008\ \text{CT} \tag{5}$$

with correlations of 0.48 (PW), 0.38 (QC), and -0.35 (CT). These regressions are shown in Figures 12, 15 and 16.

3. Satellite measurements of precipitable water

From previous studies, we knew that the vertically integrated precipitable water vapor was one of the best indicators of rain rates. Analyses of this parameter made from satellites were compared to the conventional radiosonde analyses over the United States on two days (Figs. 23-26) by Dr. Dayo Balogun. The days selected were the SESAME day of 10 April 1979 and a second day picked at random which also contained heavy precipitation, 15 May 1980.

The satellite values were taken from the system on McIDAS described by Hayden et al., (1981) which used the infrared and microwave temperature soundings from the NOAA-6 and TIROS-N satellites. This system used primarily three infrared channels sensitive to water vapor in the atmosphere. A first guess of the vertical profiles of temperature and moisture was taken from the Limited Fine Mesh Model forecast of the National Weather Service. The upwelling radiation from the surface was calculated from temperatures given by the Service-A observations. More details are given in Hayden et al., (1982).

In a qualitative sense, the satellite estimates of PW produce similar patterns to the radiosonde analyses. The higher moisture values were found in the cloudy areas and in Louisiana while drier conditions were found to the west and northeast.

However, the satellite estimates appeared to be less than the radiosondes in the moist and cloudy areas. For example, on 10 April (Figure 24) 2.5 cm were found in Oklahoma while the satellite estimated only 1.75 cm and in Louisiana 3.5 cm were present while the satellite estimated 2.5 cm. On 15 May (Figure 25) the satellite estimates also were only 75% of the radiosonde values. Similar underestimates were found in Nebraska and Iowa where the air was drier.

The sharp gradient of moisture to the west of Oklahoma into New Mexico is important for severe storm prediciton since severe storms tend to form on the boundary between wet and dry air masses. This gradient of moisture was correctly estimated on 10 April by the satellite but not on 15 May. The satellite underestimated the moisture in southwestern Texas along the Rio Grande River. Few satellite soundings were taken in this area which could possibly explain the error in the pattern.

In the extremely dry air masses, the satellite overestimated the PW. This is most evident in New Mexico and Colorado where the satellite estimates were approximately 0.5 cm high.

We conclude that the satellite soundings have some potential but they need more comparisons to radiosonde data before they can be used for estimating rain rates. Their bias has to be determined. The algorithms used to estimate moisture are being constantly improved by the NESS Techniques Development Laboratory which may be able to reduce the bias in the future. The method used here relies on having a surface temperature

analysis from in situ data. If the system were operated where surface data is not available its bias and characteristics may differ.

4. Cloud-echo areas

Griffith, et al. (1978) evaluated the echo area-cloud area relationship for cumulus clouds over south Florida. This relationship, though hard to define precisely because of scatter, is critical to any satellite based rain estimation scheme. This is because the cirrus anvils seen on satellite images are much larger than the rain areas. Since the Griffith et al. Florida study, few new rain area/cloud area data have been measured which leads to the question "Are the south Florida data valid for clouds in different geographical regions?"

To answer this question radar and satellite images for four severe storm cases in Oklahoma were inspected. The radar echo areas and cirrus anvil areas were measured for the times when the total storm system were contained within the viewing area of the radar. This limited the length of time that each storm could be followed because these storm systems grew rapidly and moved away from the radar. The maximum anvil areas were not measured because the storm systems could not be followed over their full lifetimes.

To make an echo area/cloud area comparison, the echo area measured at 20 dbz reflectivity were expressed as fractions of the cloud area measured by the 250K contour on the infrared satellite images (the solid line on Fig. 26). In one interesting case the echo area was as large as the anvil in the early stages of the storms when the anvil was small. As the anvils grew larger than 8000 km^2, the echoes dropped to 10% to 25% of the anvil. The 48 Dbz echoes dropped to 1% to 5% of the anvil areas.

Measurements were made of the 228K anvil contour for comparison to the 250K level. This resulted in a smaller anvil area measurement but, as shown in Figure 26, it mostly moved the points along the curve while raising the curves only slightly.

The most striking feature is that the echoes remained a near constant fraction of the anvil areas as they grew to very large areas of 30,000 km^2 or more. This implies that these convective systems reach a quasi-steady state. The Griffith et al., (1978) data were taken for smaller clouds than the convective complexes studied in Oklahoma. The Florida clouds exhibited a life cycle in which the echo areas peaked before the anvil areas. In the Oklahoma data we found a steady growth and were not able to follow the storms to their maximum areas.

A rough comparison between Fig. 26 and Griffith et al.'s (1978) echo/cloud area nomogram (Fig.5,p.1157), indicates that the Florida echoes were a smaller fraction of the cirrus anvils. For example, the maximum echo for a 10,000 km^2 or greater cloud in Florida was typically found to be 10% of the maximum anvil area. This occurred when the anvil was 80% of its maximum area. Thus echo/cloud area fraction was typically 12.5% (0.1/0.8) which is lower than 3 of the Oklahoma storms. Thus, the nomogram of Griffith et al., (1978) may underestimate the large storm systems which dump large amounts of rain in higher latitudes.

5. Conclusions and comments

From the statistics gathered on parameters measured by the Radiosonde and Service-A network it is apparent that some information is available on rain rates. Precipitable water and the moisture convergence parameters are the most useful from the *in situ* data. The cloud top temperature, height,

and brightness measurements from the satellite image also contain rain rate information. However, the cloud top height is so closely related to the cloud top temperature that it can not be considered as an independent measurement. On the basis of the correlations shown in Section 2, we found that a combination of PW, cloud top temperature, and moisture convergence can provide some reasonable estimation of rain rates.

Originally, we felt the one-dimensional model could be used to explain rain rate variances. This model has not been emphasized because it works only on unstable soundings. This handicap implies that it is useful only to summer precipitation in tropical air-masses and cannot be used in the other seasons on most days. The original use of the model was for predicting the seedability of clouds and it was appropriately applied to the predominantly unstable tropical soundings. Its use for mid-latitude soundings is an extension far beyond it original intent. Precipitable water, moisture convergence and cloud top temperature are universally applicable parameters. They can be used in situations where apparently stable convective conditions exist in the operational soundings such as frontal systems and around mid-latitude storms.

The two PW analyses made with satellite data indicate some information in the satellite moisture soundings. They have a bias from radiosondes which have to be defined with a larger number of comparisons before they can be used. The bias also may be different in different parts of the world which also needs to be explored.

The severe storm data indicate the bounds on the fraction of the anvil covered by rain are between 10 and 25% for large storm systems. The heavy rain covering only 1/10 of the rain area. The fractional rain area of the

cloud has some variance but some bounds on it can be statistically developed which will be useful to satellite based rain estimation schemes.

A technique using anvil expansion measurements on the satellite images is described in the Appendix which may help rain estimation schemes for situations where expanding anvils are present. For the AGRISTAR program, we did not make these measurements. We concentrated on precipitating clouds that seldom had expanding anvils. The Appendix indicates that expanding anvil measurements can be usefully combined with water vapor measurements from radiosondes. This technique uses data on the actual cloud motions rather than predicting them from external data as the bubble model does. It can be combined with other satellite rain estimation techniques for covering the heavy Cb convection.

References

Barnes, S.L., 1964: A technique for maximizing details in numerical weather map analysis. J. Appl. Meteor. 3,396-409.

Biomedical Center Computing Programs, 1977, Health Sciences Facility of the University of California at Los Angeles. University of California Press, Berkley, CA. 880 pp., Libraryl of Congress #77-83772.

Griffith, C.G., W.L. Woodley, P.G. Grube, D.W. Martin, J. Stout, and D. N. Sikdar, 1978: Rain estimation from geosynchronous satellite imagery-visible and infrared studies. Mon. Wea. Rev., 106, 1153-1171.

Griffith, C. G., J.A. Augustine, and W.L. Woodley, 1981: Satellite rain estimation in the U.S. High Plains. J. Appl. Met., 20, 53-66.

Hayden, C. M., W. L. Smith, H. M. Woolf, 1981: Determination of moisture from NOAA polar orbiting satellite sounding radiances. J. Appl. Meteor., 20, 450-466.

Kilonsky, B. J., and C. S. Ramage, 1976: A technique for estimating tropical open-ocean rainfall from satellite observations. J. Appl. Meteor., 15, 972-975.

Mack, R. A., and D. P. Wylie, 1982: An estimation of the condensation rates in three severe storms from satellite measurements of the convective mass flux. Mon Wea. Rev., in press.

Panofsy, H.A. and G. W. Brier, 1968: Some applications of statistics to meteorology. Penn. State Univ. Press, University Park, Pa. 224 pp.

Park, S., and D. N. Sikdar, 1980: An application of a simple diagnostic cloud model to the May 20, 1977 storms over the Oklahoma meso-network. Tellus, 32, 326-339.

Sikdar, D. N., V. E. Suomi, and C. E. Anderson, 1970: Convective transport of mass and energy in severe storms over the United States--An estimate from geostationary altitude. Tellus, 5, 521-532.

Simpson, J. and V. Wiggert, 1969: Models of precipitating cumulus towers. Mon. Wea. Rev., 97, 471-489.

Stout, J. D., W. Martin, and D. N. Sikdar, 1979: Estimating GATE rainfall from geostationary satellite images. Mon. Wea. Rev., 107, 585-598.

Woodley, W., C.G. Griffith, J.S. Griffin, and S. Stromatt, 1980: The infreference of GATE convective rainfall from SMS-1 imagery. J. Appl. Met., 19, 388-408.

Wylie, D.P., 1979: An Application of a geostationary satellite rain estimation technique to an extratropical area. J. Appl. Met., 18, 1640-1648.

TABLE 1

MEASURED PARAMETER	CORRELATION WITH 6 HOUR PRECIP. REPORT	NUMBER OF CASES	F
1. Vertically integrated precipitable water vapor	0.48	196	58 *
2. Cloud top brightness	-0.44	184	44 *
3. Cloud top height	-0.40	190	36 *
4. Moisture convergence	0.38	184	31 *
5. Cloud top temperature	-0.35	199	27 *
6. Bubble model predicted cond.	0.27	115	9
7. 500 mb vorticity advection	-0.21	173	8 *
8. Parcel lifted index	-0.20	200	8 *
9. 700 mb temperature advection	0.20	173	7 *
10. sfc temperature advection	0.19	156	6
11. 850 mb temperature advection	0.17	189	6
12. Wind convergence (sfc)	0.09	167	1
13. Vertical wind shear	0.03	156	0

* Significant correlation at the 99% level.

List of Figures

Figure 13: The 6 hour precipitation as a function of the brightest cloud top at local noon (1800 GMT) measured on the GOES-E images. The scale is in digital counts form 0 (black) to 255 (saturated white).

Figure 14: The 6 hour precipitation measurements as a function the highest cloud top height.

Figure 15: The 6 hour precipitation measurements as a function of the surface mixing ratio (Q) divergence at 1800 GMT (local noon). Negative values indiate moisture convergence. The line is a least squares fit to the data.

Figure 16: The 6 hour precipitation measurements as a function of the coldest cloud top temperatues measured on satellite images.

Figure 17: The 6 hour precipitation measurements as a function of the bubble model predicted condensation. The units are in grams of condensed water per kg of air at cloud base.

Figure 18: The 6 hour precipitation measurements as a function of the vorticity advection of the 500 mb winds. This parameter was calculated from a uniform grid analyses (3.0° spacing) made from the 1200 GMT radiosonde observations.

Figure 19: The 6 hour precipitation measurements as a function of the parcel lifted index calculated from the 1200 GMT sounding nearest the precipitation. Unstable cases are where the index is <Ø and stable >0.

Figure 20: The 6 hour precipitation measurements as a function of the temperature advection of the 700 mb wind field. Calculations were made from uniform grid analyses (3.0° spacing) of the 1200 GMT soundings.

Figure 21: The 6 hour precipitation measurements as a function of the surface wind field divergence measured at 1800 GMT (local noon).

Figure 22: The 6 hour precipitation measurements as a function of the vertical wind shear vector magnitude between 500 mb-sfc measured on 1200 GMT soundings nearest the precipitation.

Figure 23: The measured 6 hour precipitation vs. a statistical estimate made from the precipitable water, cloud top temperature, and mixing ratio convergence measurements made in the vicinity of the rain. The 1:1 relation is indicated by the straight line.

Figure 24: The vertically integrated precipitable water vapor measurements (shown as contours) from the TIROS-N satellite soundings (a) made at 2043 GMT 10 April 1979, and the radiosonde measurements taken at 00 GMT 11 April 1979 (b). Shading indicates areas of partial cloud cover and the dots are the locations of the satellite soundings.

Figure 25: The vertically integrated precipitable water vapor measurementds from the 1435 GMT 6 May 1980 orbit of the NOAA-6 satellite (a) and the radiosonde measurements taken at 1200 GMT 6 May 1980 radiosonde measurements (b). Shading indicates partial cloud cover and the dots are the locations of the satellite soundings.

Figure 26: The radar measured precipitation echo area divided by the satellite measured cloud area. The 20 dbz echo/250K satellite area is depicted by the solid line. The 48 dbz echo/228K satellite area is shown by the dashed line.

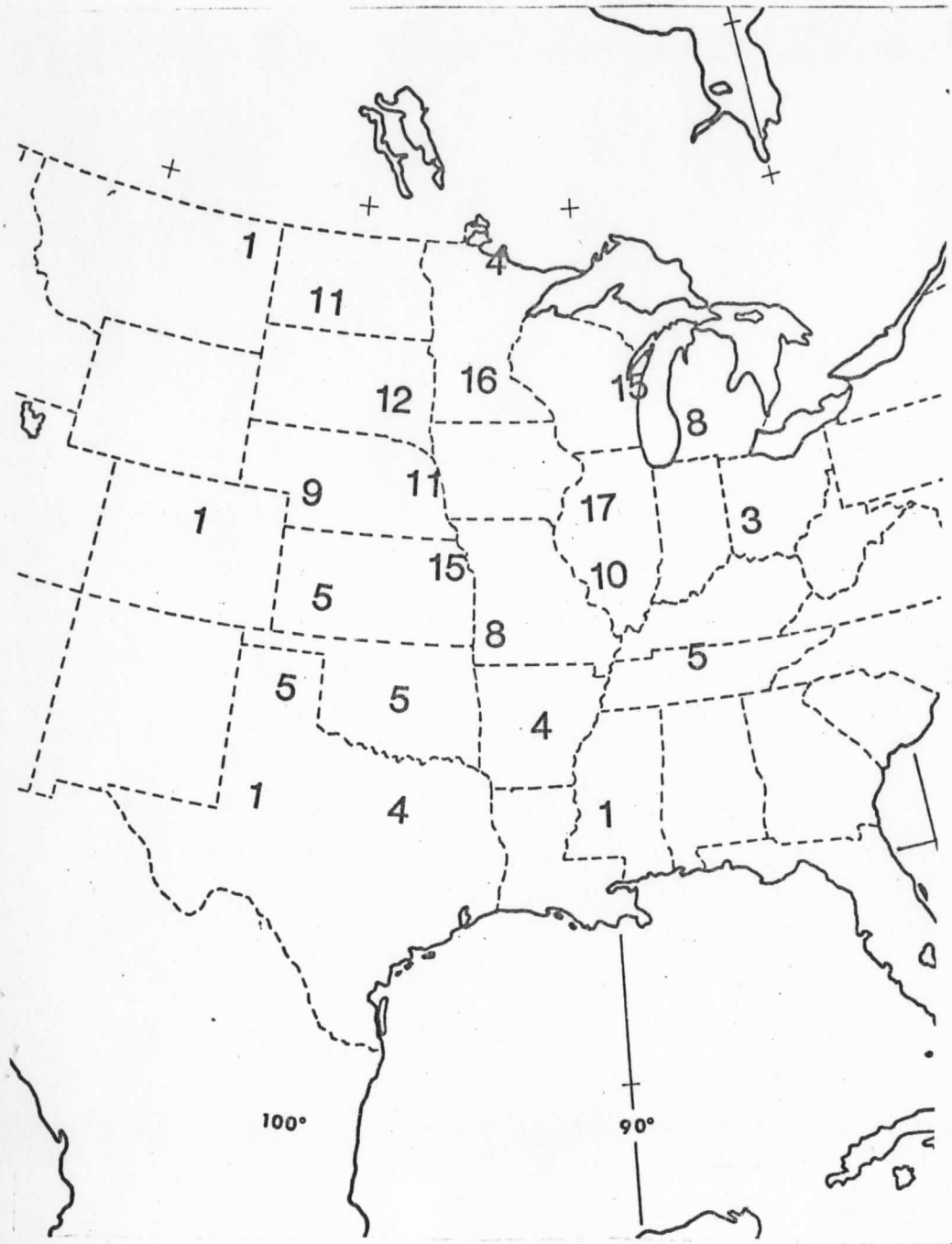

Figure 1: The number of days of precipitation studied for each readiosonde cite.

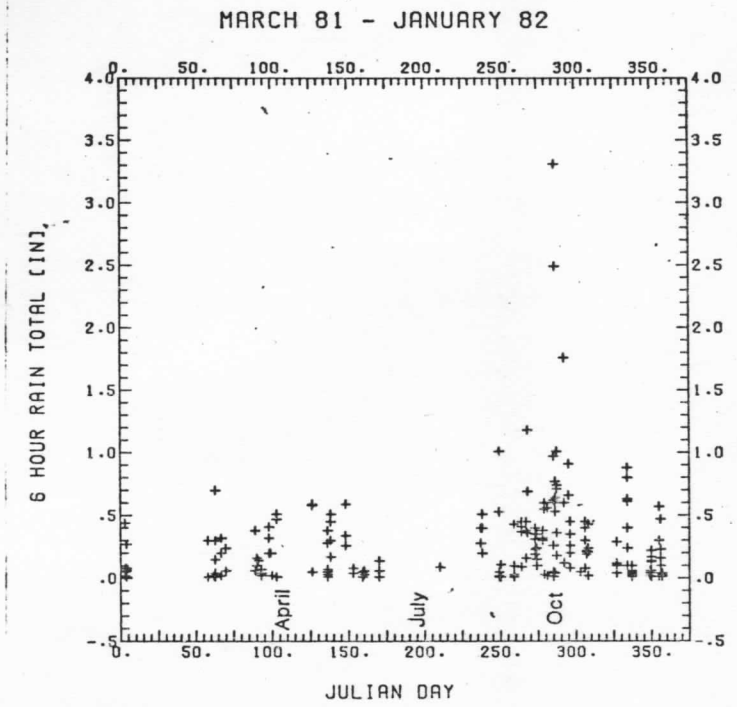

Figure 2: The six hour Service-A rainfall reports taken as a function of the Julian Day in the Mid-western and Great Plains states.

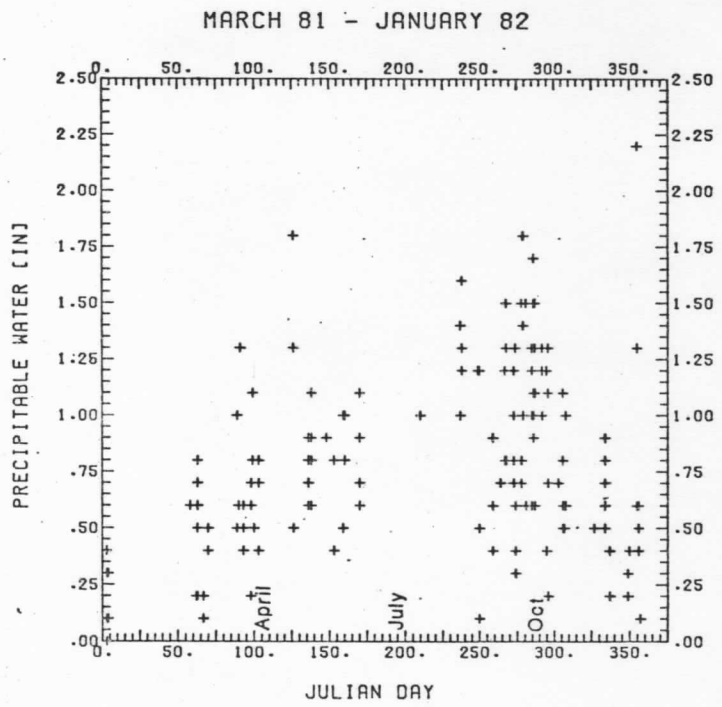

Figure 3: The vertically integrated precipitable water vapor measurements in the vicinity of rain at 1200 GMT (600 LST) for each day studied.

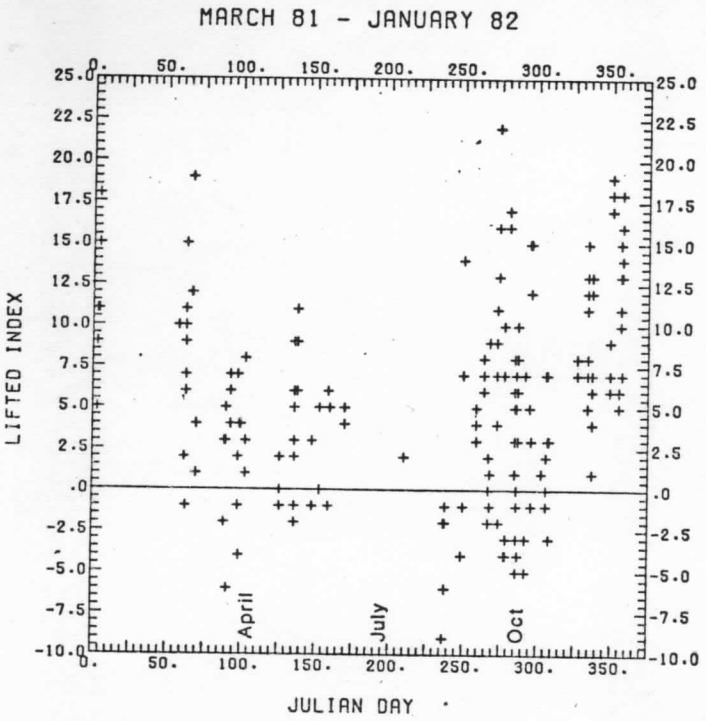

Figure 4: The parcel lifted index of the soundings studied (1200 GMT).

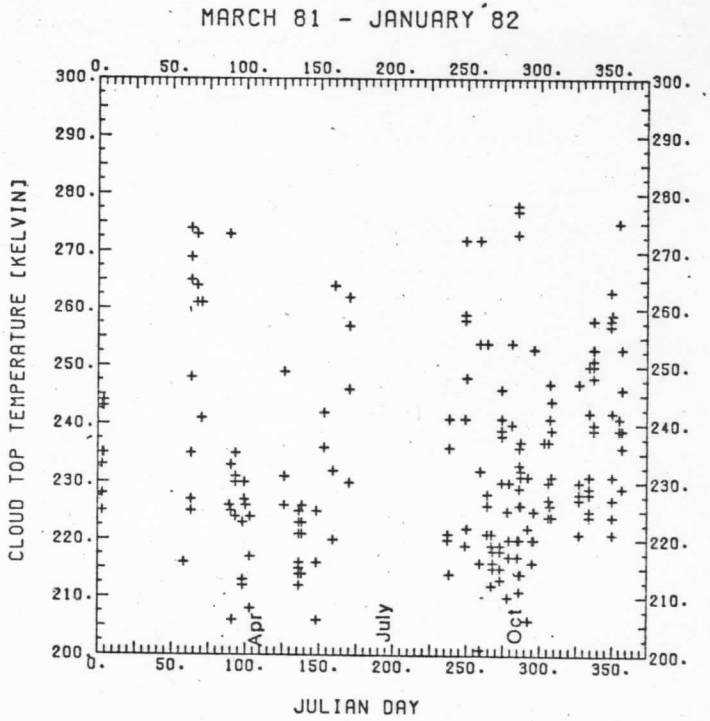

Figure 5: The temperatues of the coldest cloud tops where rain occurred in the Great Plains and Mid-western states as measured on satellite infrared images from 1200-1800 GMT (600-1200 LST).

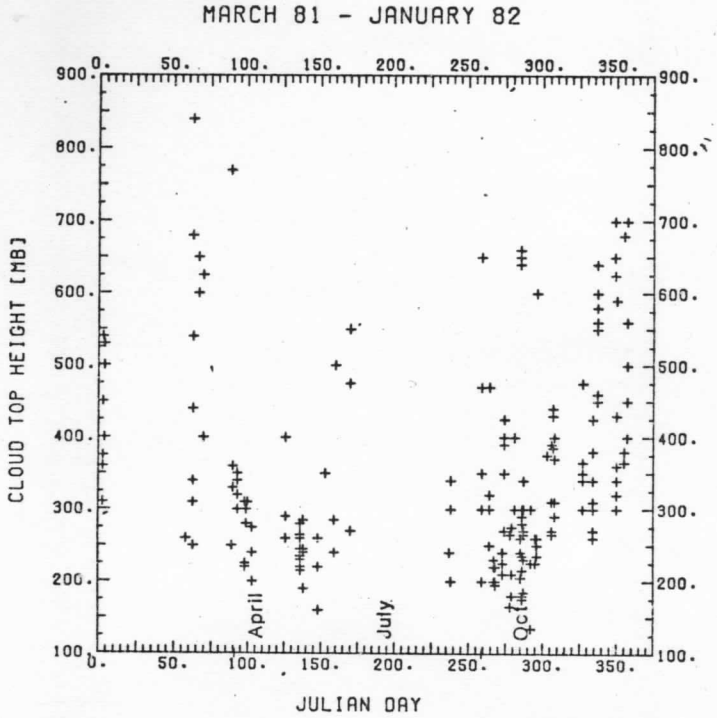

Figure 6: The heights of the coldest cloud tops in the vicinity of rain in the great Plains and Mid-western states. The heights were determined from the cloud top temperatures shown in Figure 3 and the temperature profiles of the nearest soundings.

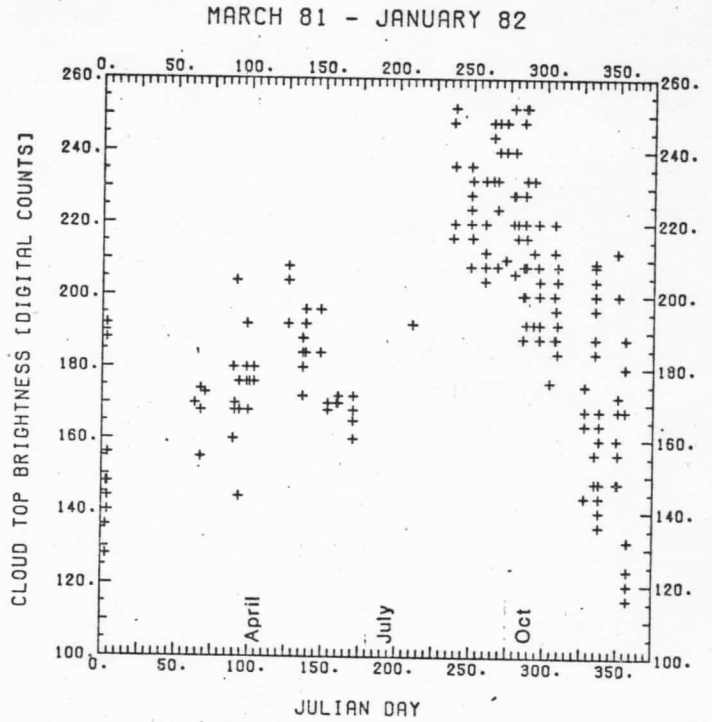

Figure 7: The satellite measured brightness of the cloud tops where rain occurred in the Great Plains and Mid-western states. The units are digital counts reported by the GOES system multiplied by 4. The range is from 0 (black) to 255 (saturated white).

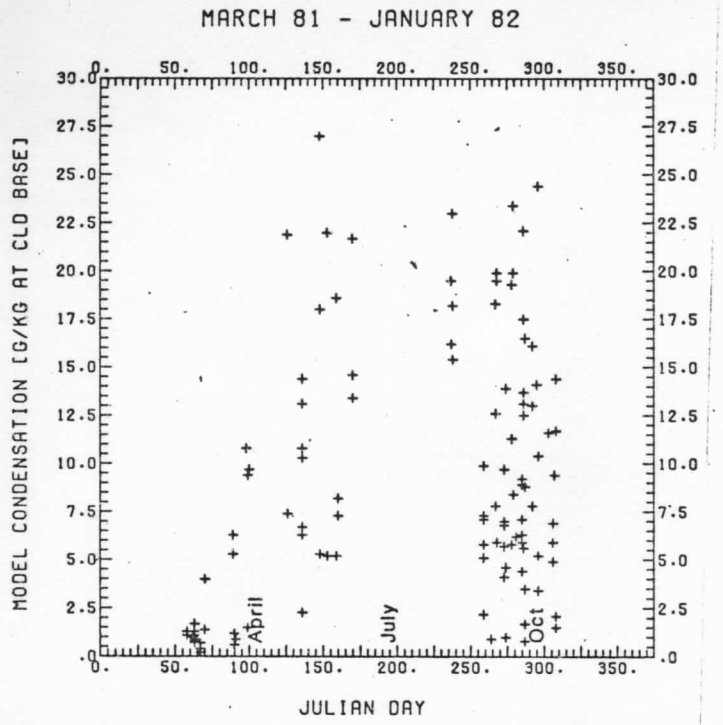

Figure 8: One dimensional model estimated condensation for an idealized bubble ascend on soundings near precipitations. The units are grams of water condensed per Kg of air at cloud base.

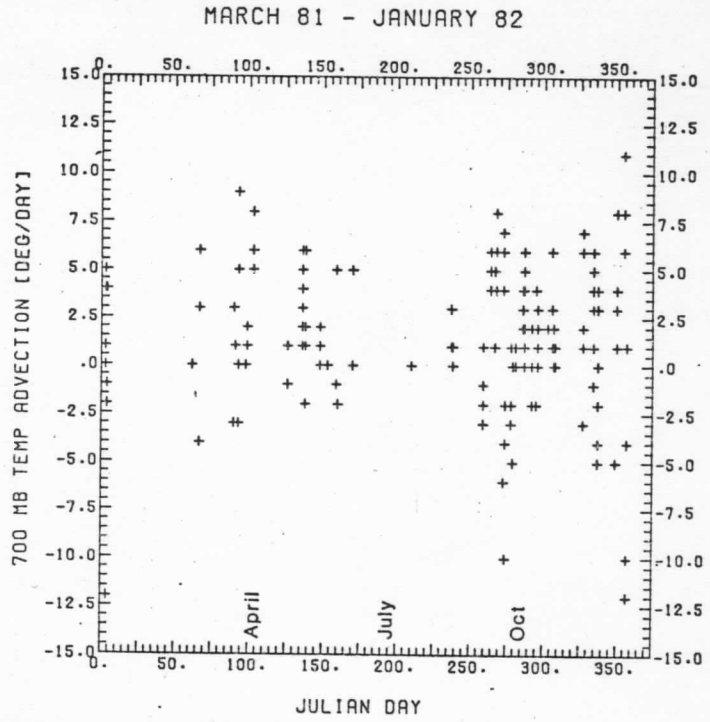

Figure 9: The temperature advection of the 700 mb wind in the vicinity of rain in the Great Plains and Mid-western states taken from the 1200 GMT (600 LST) soundings. The soundings were analyzed to a uniform grid of 3.0° latitude and longitude for the advection calculations.

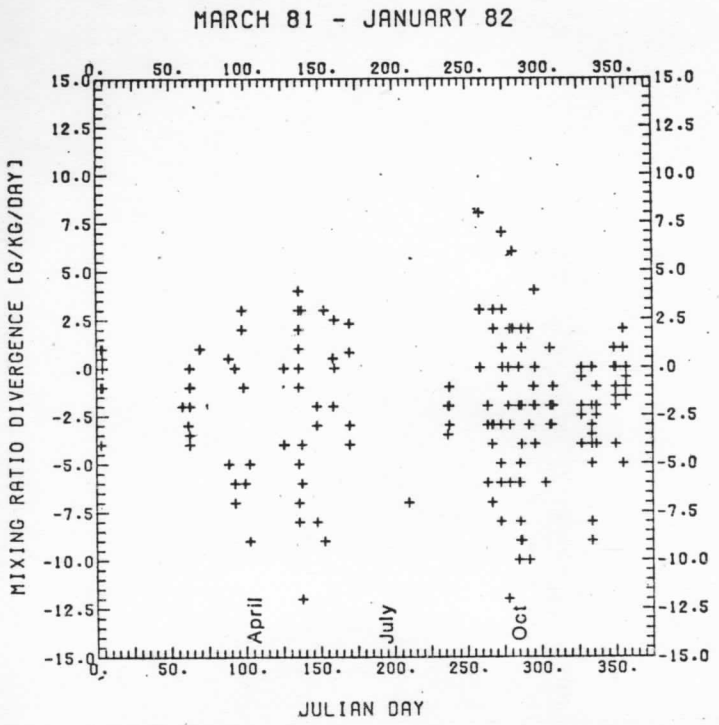

Figure 10: The mixing ratio (Q) divergence in the vicinity of rain in the Great Plains and Mid-western states. The Q divergence was calculated from a grid of 3.0° spacing made from the 1800 GMT Service-A data.

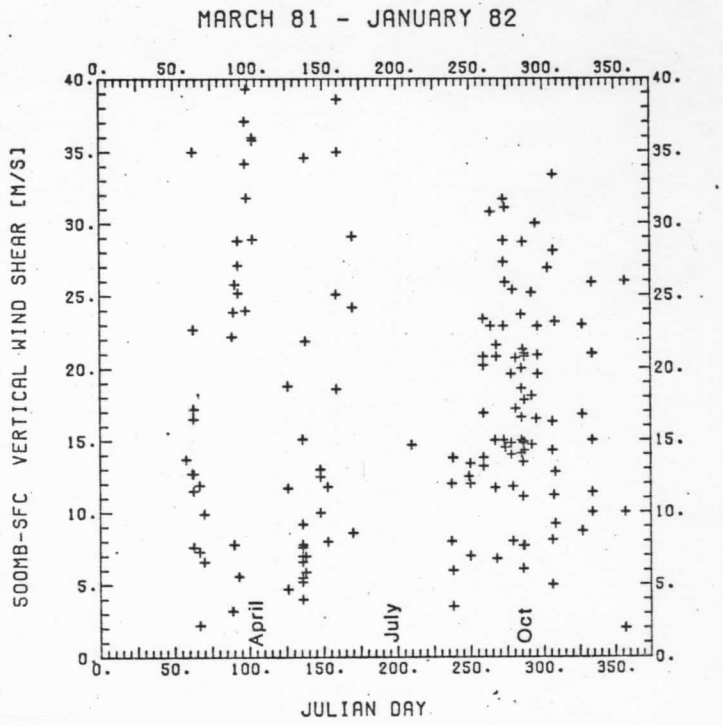

Figure 11: The vertical wind shear vector magnitude (500 mb-sfc) calculated from the 1200 GMT soundings near precipitation in the Great Plains and Mid-western states.

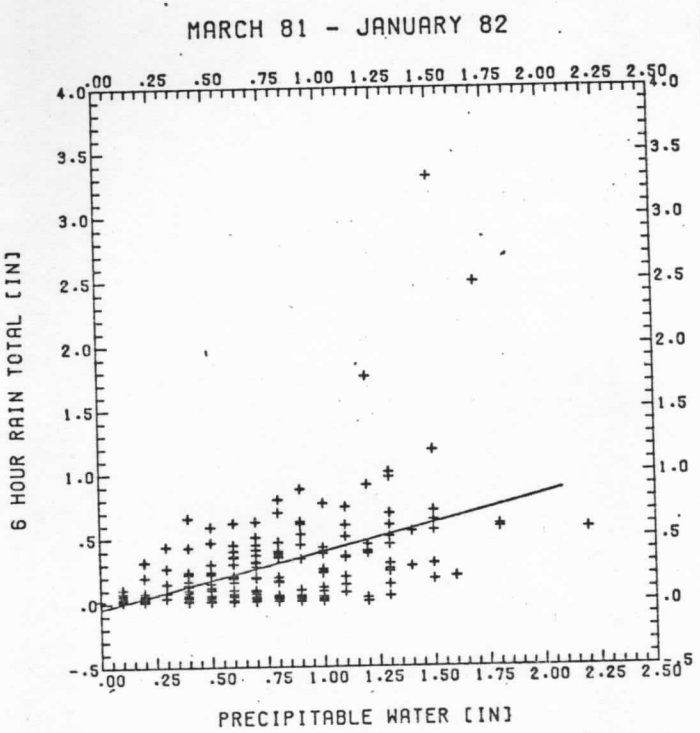

Figure 12: The 6 hour precipitation as a function of the vertically integrated precipitable water vapor quantities calculated from the 1200 GMT soundings nearest the raining areas. The line is a least squares fit to the data.

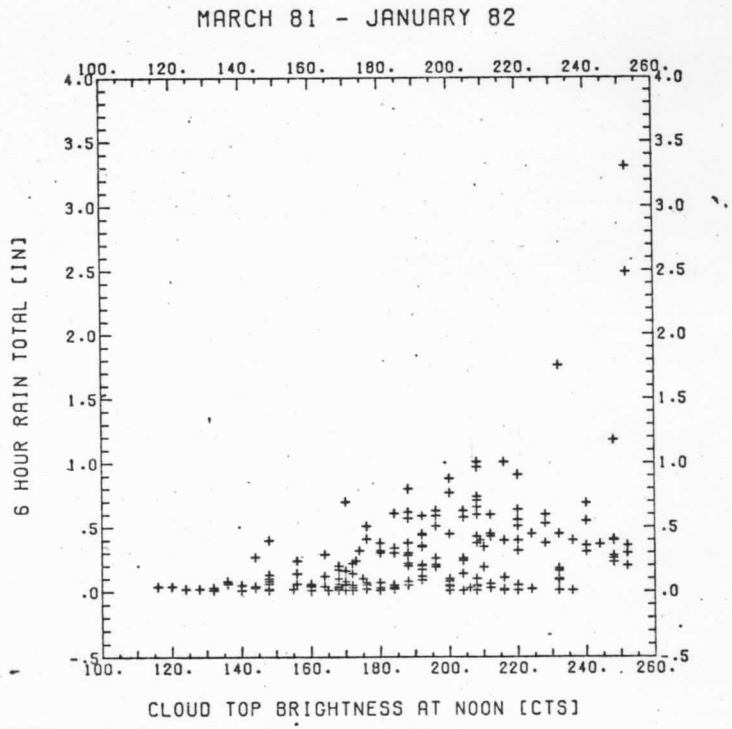

Figure 13: The 6 hour precipitation as a function of the brightest cloud top at local noon (1800 GMT) measured on the GOES-E images. The scale is in digital counts form 0 (black) to 255 (saturated white).

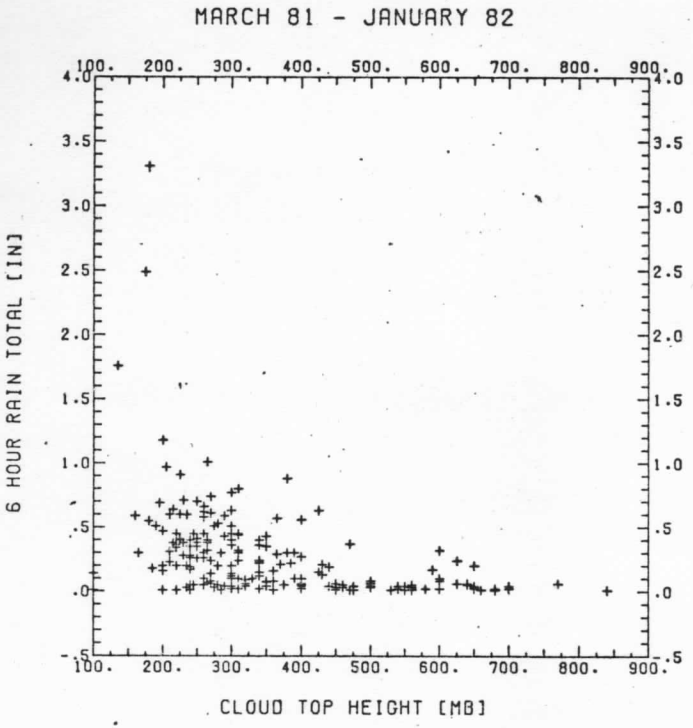

Figure 14: The 6 hour precipitation measurements as a function the highest cloud top height.

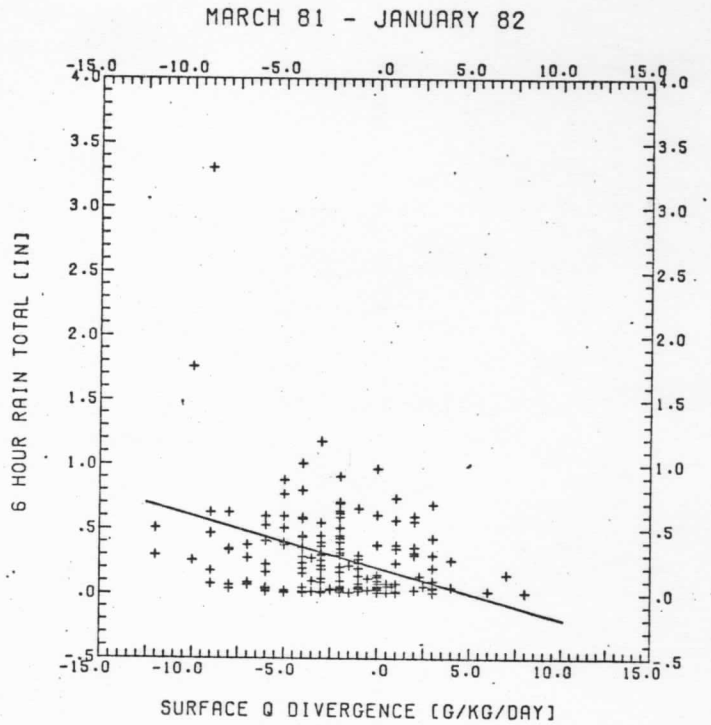

Figure 15: The 6 hour precipitation measurements as a function of the surface mixing ratio (Q) divergence at 1800 GMT (local noon). Negative values indiate moisture convergence. The line is a least squares fit to the data.

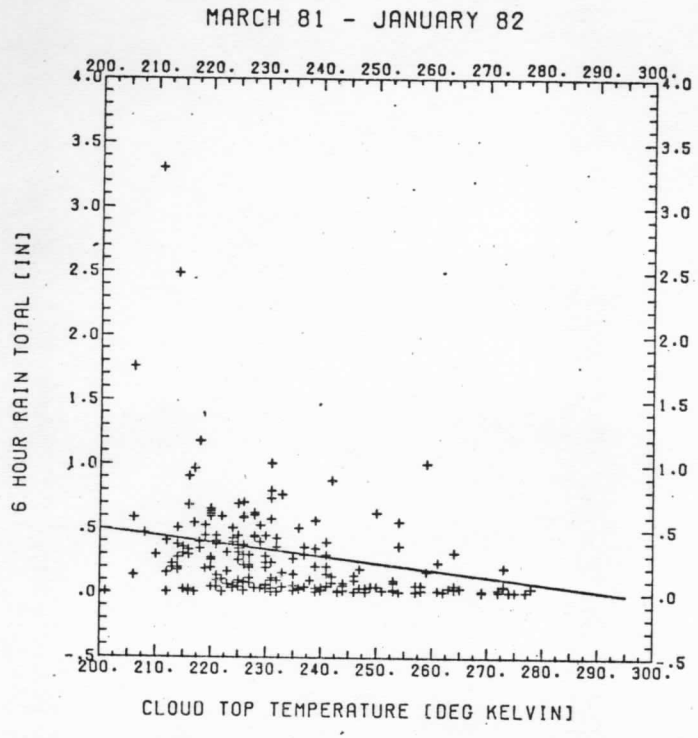

Figure 16: The 6 hour precipitation measurements as a function of the coldest cloud top temperatues measured on satellite images.

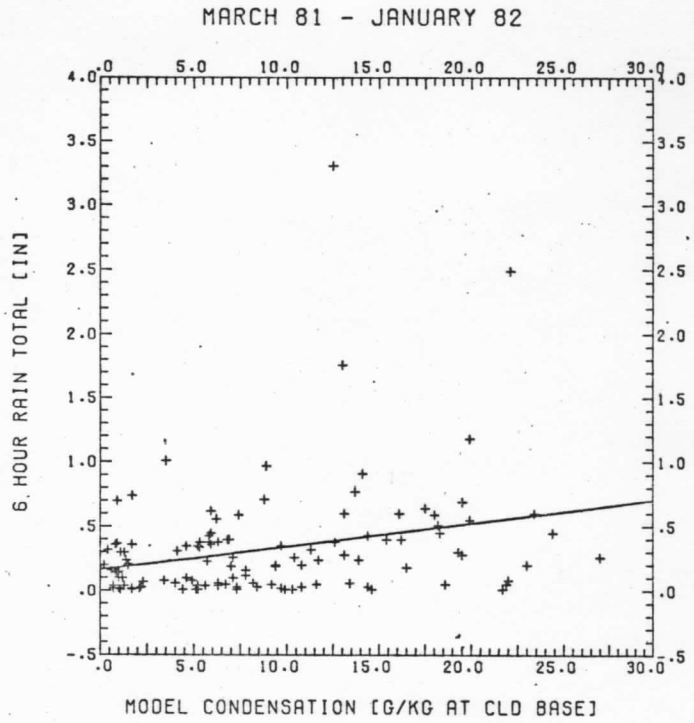

Figure 17: The 6 hour precipitation measurements as a function of the bubble model predicted condensation. The units are in grams of condensed water per kg of air at cloud base.

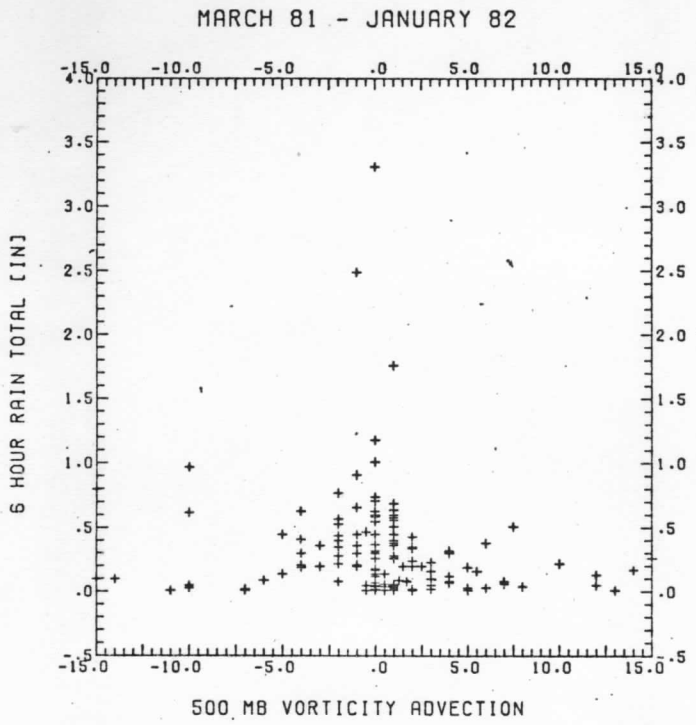

Figure 18: The 6 hour precipitation measurements as a function of the vorticity advection of the 500 mb winds. This parameter was calculated from a uniform grid analyses (3.0° spacing) made from the 1200 GMT radiosonde observations.

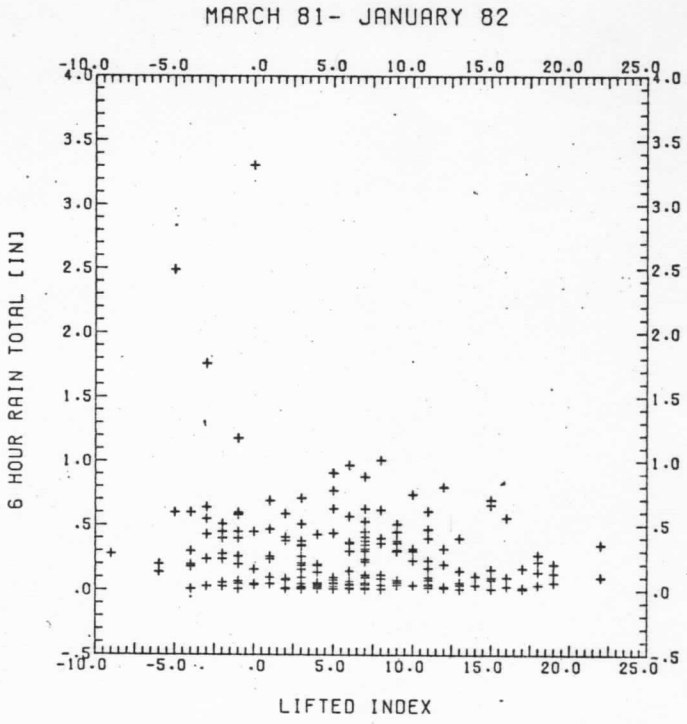

Figure 19: The 6 hour precipitation measurements as a function of the parcel lifted index calculated from the 1200 GMT sounding nearest the precipitation. Unstable cases are where the index is <Ø and stable >0.

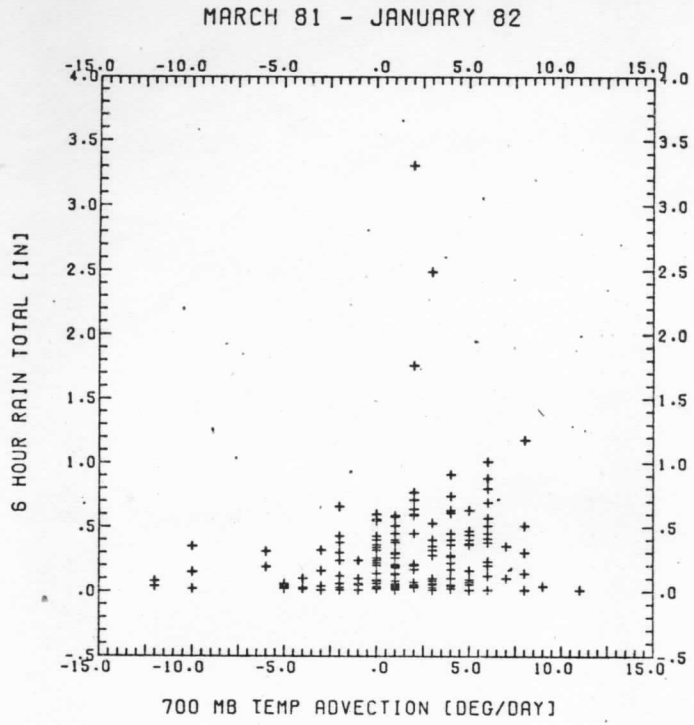

Figure 20: The 6 hour precipitation measurements as a function of the temperature advection of the 700 mb wind field. Calculations were made from uniform grid analyses (3.0° spacing) of the 1200 GMT soundings.

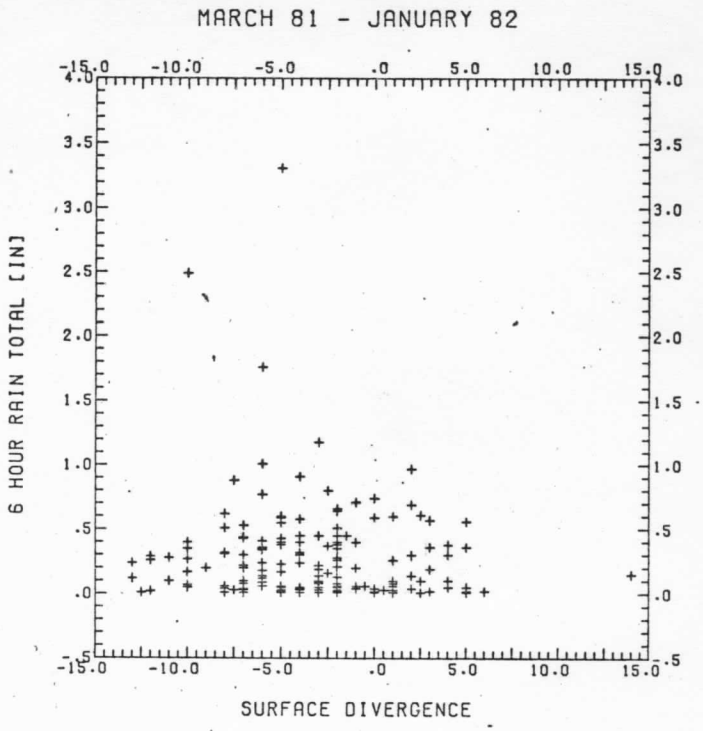

Figure 21: The 6 hour precipitation measurements as a function of the surface wind field divergence measured at 1800 GMT (local noon).

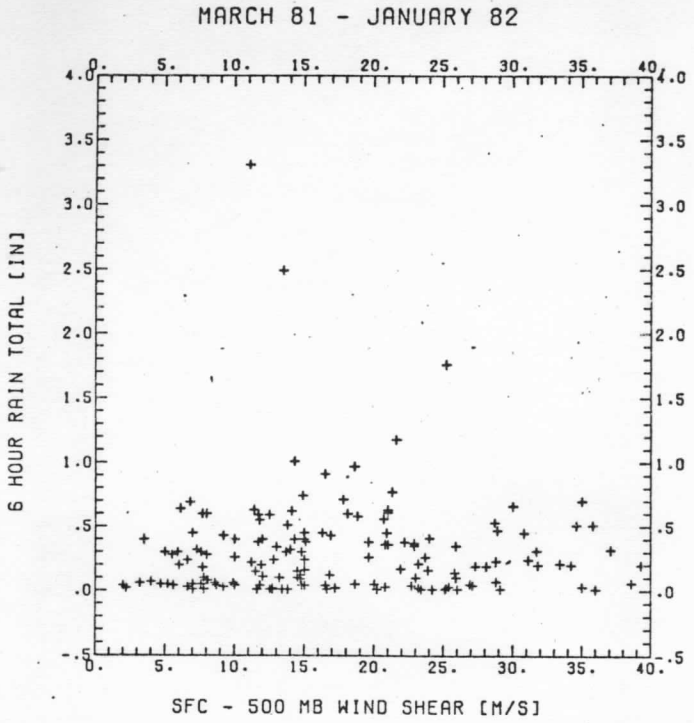

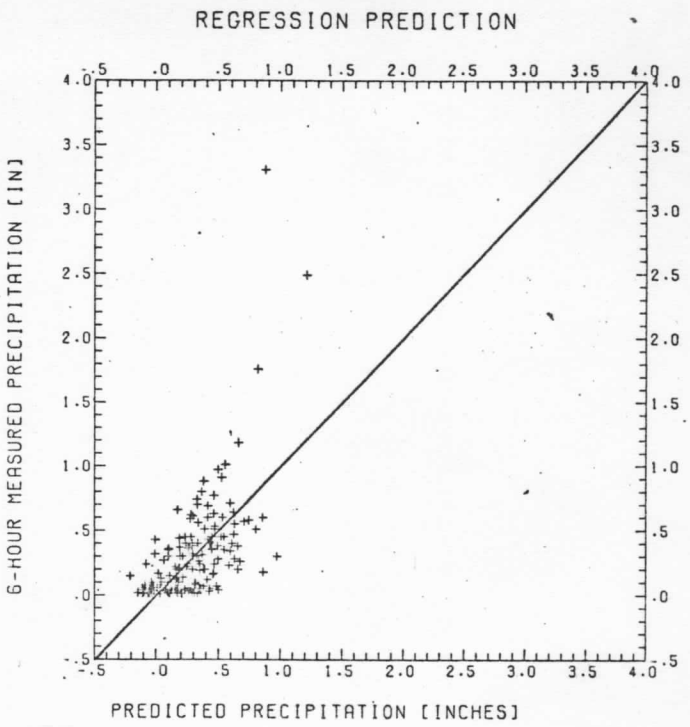

Figure 22: The 6 hour precipitation measurements as a function of the vertical wind shear vector magnitude between 500 mb-sfc measured on 1200 GMT soundings nearest the precipitation.

Figure 23: The measured 6 hour precipitation vs. a statistical estimate made from the precipitable water, cloud top temperature, and mixing ratio convergence measurements made in the vicinity of the rain. The 1:1 relation is indicated by the straight line.

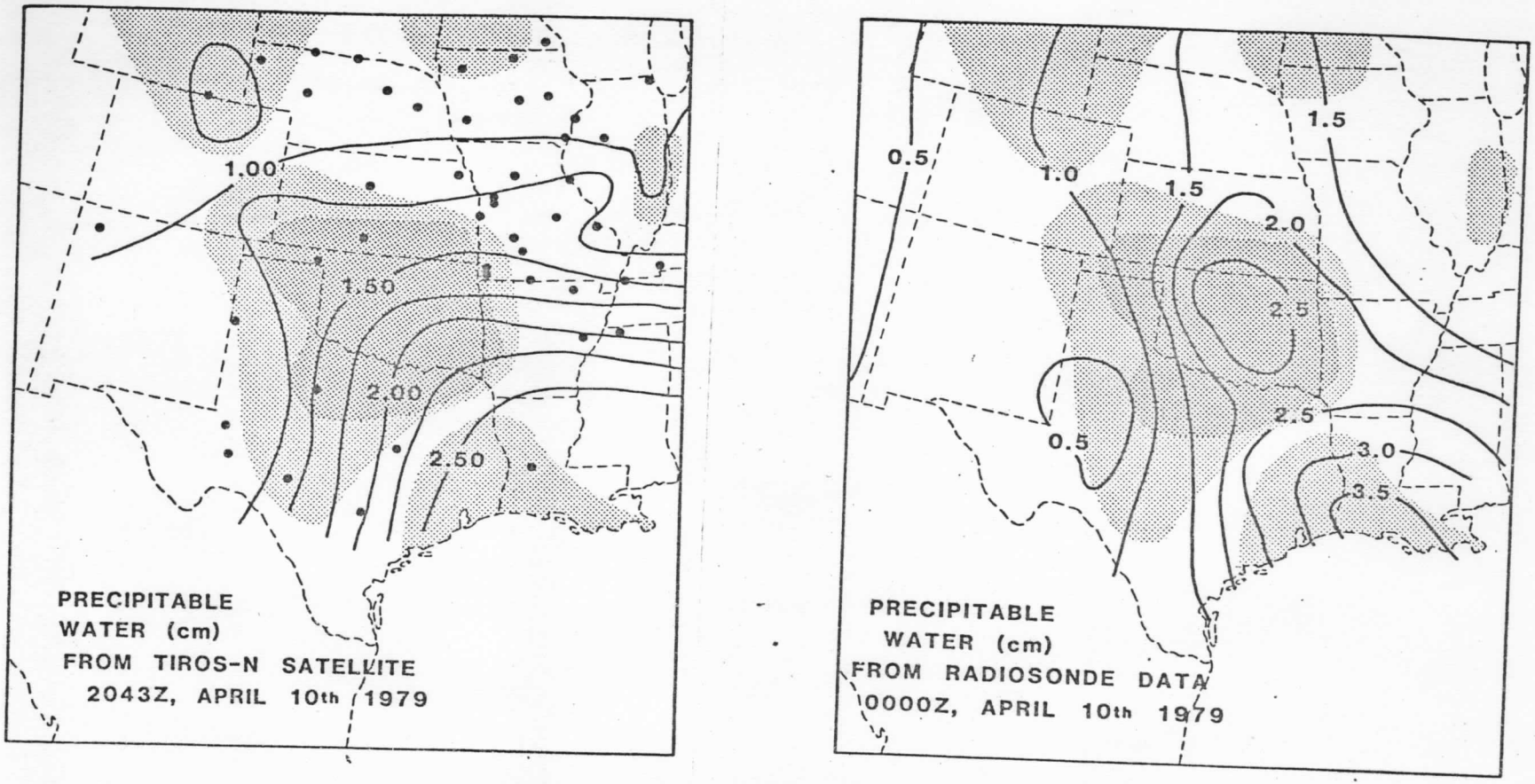

Figure 24: The vertically integrated precipitable water vapor measurements (shown as contours) from the TIROS-N satellite soundings (a) made at 2043 GMT 10 April 1979, and the radiosonde measurements taken at 00 GMT 11 April 1979 (b). Shading indicates areas of partial cloud cover and the dots are the locations of the satellite soundings.

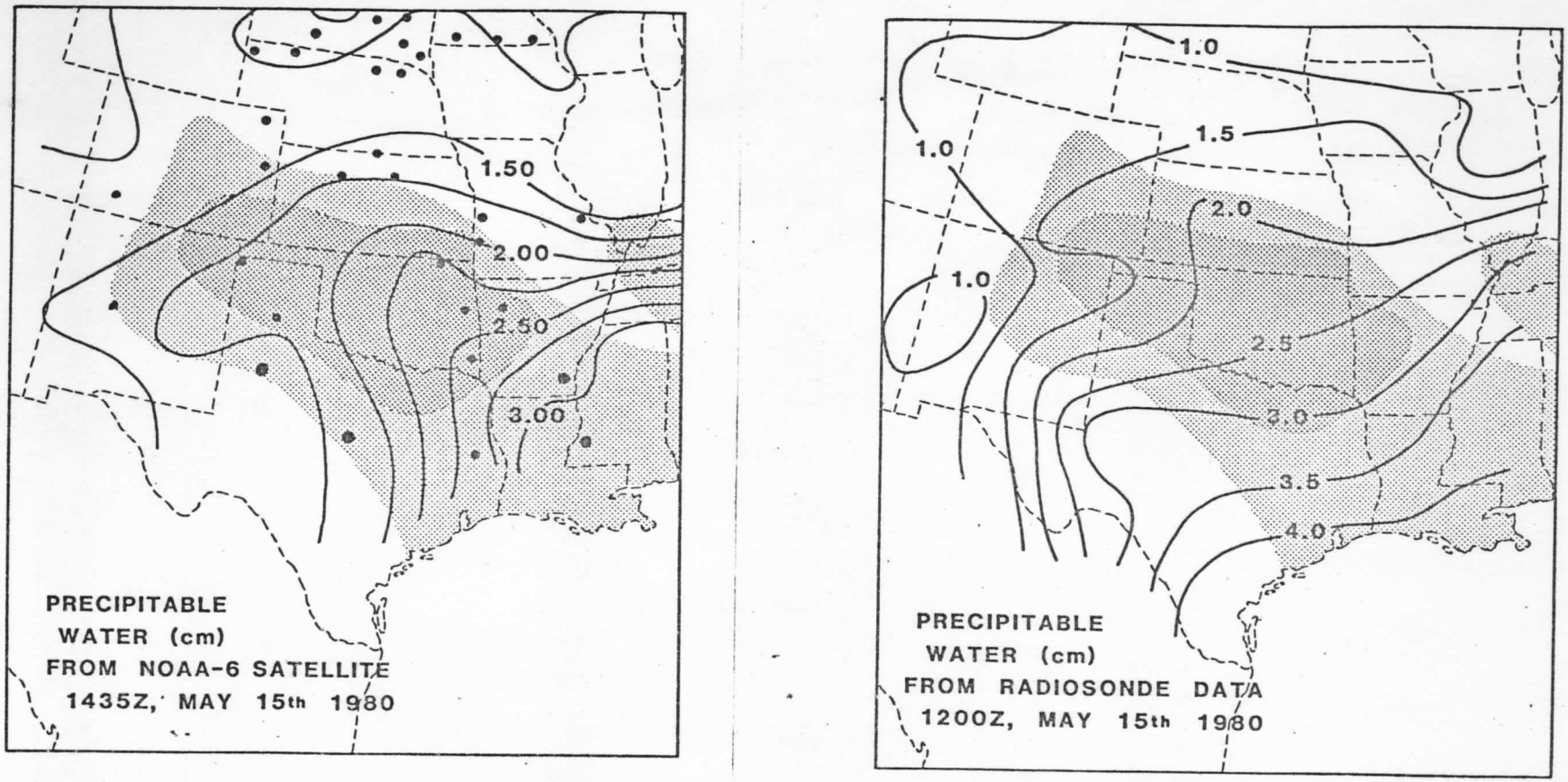

Figure 25: The vertically integrated precipitable water vapor measurementds from the 1435 GMT 6 May 1980 orbit of the NOAA-6 satellite (a) and the radiosonde measurements taken at 1200 GMT 6 May 1980 radiosonde measurements (b). Shading indicates partial cloud cover and the dots are the locations of the satellite soundings.

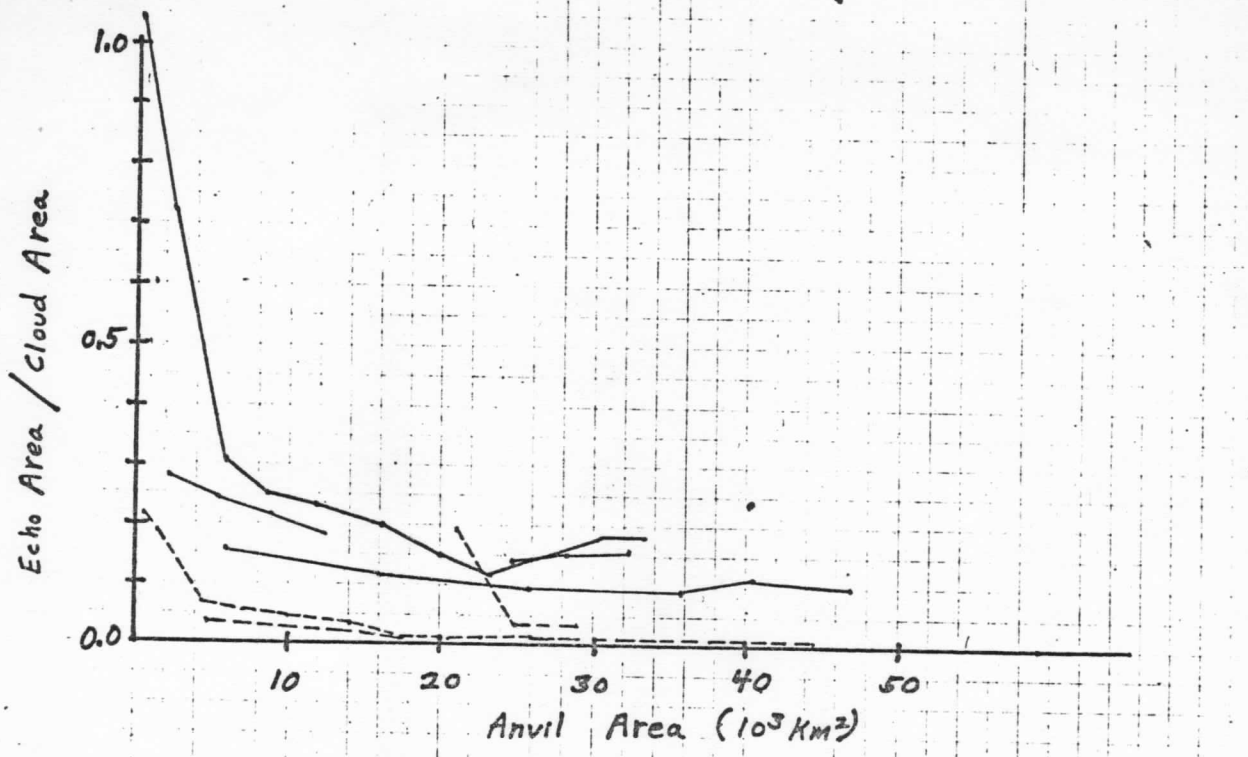

Figure 26: The radar measured precipitation echo area divided by the satellite measured cloud area. The 20 dbz echo/250K satellite area is depicted by the solid line. The 48 dbz echo/228K satellite area is shown by the dashed line.

APPENDIX

An Estimation of the Condensation Rates in Three Severe Storm Systems from Satellite Observations of the Convective Mass Flux

by

Robert A. Mack[1]

and

Donald P. Wylie[2]

University of Wisconsin-Milwaukee
Milwaukee, Wisconsin

[1]Present Address: Goddard Laboratory for Atmospheric Sciences
NASA/Goddard Space Flight Center
Greenbelt, Maryland 20771
Affiliated with: GE/MATSCO, Beltsville, Maryland 20705

[2]Present Address: Space Science and Engineering Center
University of Wisconsin-Madison
Madison, Wisconsin 53706

Revised
February 1982
To be published in
Monthly Weather Review

Abstract

A technique was developed for estimating the condensation rates of convective storms using satellite measurements of cirrus anvil expansion rates and radiosonde measurements of environmental water vapor. Three cases of severe convection in Oklahoma were studied and a diagnostic model was developed for integrating radiosonde data with satellite data.

Two methods were used to measure the anvil expansion rates; the expansion of isotherm contours on infrared images, and the divergent motions of small brightness anomalies tracked on the visible images. The differences between the two methods were large as the storms developed, but these differences became small in the latter stage of all three storms.

A comparison between the three storms indicated that the available moisture in the lowest levels greatly affected the rain rates of the storms. This was evident from both the measured rain rates of the storms and the condensation rates estimated by the model. The possibility of using this diagnostic model for estimating the intensities of convective storms also is discussed.

1. Introduction

The intensities of convective storms are usually expressed by the rainfall rates they produce or by the magnitudes of their vertical motions if such data are available. Using satellites Sikdar et al. (1970) have shown that storm intensities could be monitored by measuring the expansion rates of the cirrus anvils seen on sequences of geostationary images. Based on the premise that the anvil expansion rates are indicative of the flux of air drawn into the clouds, several algorithms for empirically estimating rainfall have been developed (Sikdar, 1972, Scofield and Oliver, 1977, Griffith et al., 1978, Stout et al., 1979, and Woodley et al., 1980). While these studies have had success in providing rain information, mainly in the tropics, they have had problems in estimating rain rates in non-tropical areas. These problems have been attributed to the variable moisture and wind shear environments of non-tropical areas which are believed to have affected the dynamics of the clouds and their condensation rates (Wylie, 1979, Scofield and Oliver, 1977, and Griffith et al., 1981). To gain more information on how environmental conditions affect precipitating clouds, we developed a diagnostic model for use with the anvil expansion measurements that accounts for the moisture entrained into the clouds. This model was applied to three intense convective storms in Oklahoma. It was developed on the first case, 20 May 1977, and then applied to two other cases on 30 May 1976 and 27 May 1979 to evaluate the efficiencies of condensation inside the clouds.

Anvil expansion measurements from satellite data were combined with environmental data from radiosondes and rainfall data from the WSR-57 radar and rain gauges provided by NOAA's Environmental Data Service at the National Climate Center in Asheville, North Carolina. Our objective is to bridge the gap between satellite methods of monitoring storms and the uses of

more conventional data sources. We will show how satellite data can be combined with cloud environmental data to improve estimates of convective rainfall and how these data can be used for evaluating the intensities of severe storms for either research or forecasting purposes.

2. The Diagnostic Model

According to Sikdar et al. (1970) the rate of areal expansion of the cirrus anvil can be related to the cloud divergence at the level of outflow by:

$$\nabla_h \cdot \tilde{V}_c = \frac{1}{A_c} \frac{dA_c}{dt} \qquad (1)$$

where ∇_h is the horizontal gradient operator, $\tilde{V}_c$ the velocity of the perimeter of the anvil, and Ac the anvil area. Sikdar was able to show that divergence rates greater than $6.0\ (10)^{-4} s^{-1}$ indicated strong vertical motions and possibly severe storms. A simple three layer model was used by Sikdar to compute the volume flux of air diverging from the anvil and the flux into the cloud base. The Sikdar model consisted of a Level of Inflow (LIF), which extended from the ground to the Lifting Condensation Level (LCL), a Level of Vertical Motion (LVM) from the LCL to the bottom of the outflow layer, and the Level of Outflow (LOF) in the anvil. It was assumed that entrainment into the updraft in a severe storm was small in the LVM and could be neglected and also that the outflow layer was 1 km thick.

Sikdar, et al (1970) made these assumptions because of the lack of information on LOF thickness and entrainment rates into the LVM. In the present study we used values for these quantities that were calculated from budgets around one cell in one of the convective systems (Park and Sikdar, 1980).

To determine expansion rates of the cirrus anvil, Sikdar et al. (1970) measured the change of area enclosed by a particular brightness contour

corrected for solar zenith angle on the visible satellite images. A similar technique was also applied to infrared images by Stout et al. (1979) and Weickman et al. (1977) which did not require any sun angle corrections.

Lo (1976) refined Sikdar's technique by dividing the anvil into slabs of different thickness based on the satellite measured brightness. The expansion rates of several brightness contours were measured to calculate the total anvil divergence from the sum of the slabs. The vertical mass flux inside the cloud also was modelled to consider horizontal entrainment into the updraft above the cloud base. Lo (1976) estimated the condensation rate inside the cloud using the mixing ratio measured outside of the cloud and an assumption of this parameter inside the cloud. This in effect was the Austin and Houze (1973) model worked backwards.

We modified Lo's method by calculating the rate of anvil divergence from the motions of small brightness features (bright spots or variations in brightness) near the perimeter of the anvil that were seen on visible satellite images. An example of one image is shown in Figure 1. The brightness features that were tracked have been lost by the photographic reproduction process. The motion analyses were made on the McIDAS of the University of Wisconsin (Smith, 1975) where the images were enhanced to show the details of the anvil. Quantitative calculations of the velocities were made using the cloud tracking software on the Man-computer Interactive Data Access System (McIDAS, Smith and Phillips, 1972).

Divergence rates were calculated using Stoke's theorem:

$$\nabla_h \cdot \vec{V}_c = \frac{1}{A_c} \oint \vec{V}_n \, dl \qquad (2)$$

applied to the line integral of the normal motion components, $\vec{V}_n$, on the boundary of the polygon, l, described by the vectors divided by the area

of the polygon. The average mass flux, $\overline{M_c}$, diverging in the polygon was defined as:

$$\overline{M_c} = \frac{-A_c}{g} \int_{P_1}^{P_2} \overline{\nabla_h \cdot \vec{V}_c} \, dP \qquad (3)$$

Where A_c is the average area, g the gravitational constant, $\overline{\nabla_h \cdot \vec{V}}$ the average divergence for the layer, dp, and P_1, and P_2 are the pressure at the bottom and top of the layer of outflow.

The satellite measured motion vectors specified the divergence for only one level. To compute the mass flux diverging in the anvil the vertical structure of the wind divergence in the outflow layer had to be estimated. Soundings from the NSSL rawinsonde network were used to model the vertical structure of the outflow layer. We assumed that the thickness and the shape of the upper level environmental divergence profile derived from the soundings were similar to the shape and thickness of the anvil measured divergence profile in the LOF even though the NSSL network was smaller than the total anvil. In reality, all large storm systems contain many individual cells with outflow layers of different thicknesses and structures. Because detailed information on small cells inside a large storm complex was not available, we used the results from the NSSL network as a guide to the vertical structure of the outflow layer. The smoothed environmental divergence profile in the outflow layer is roughly parabolic in shape (Fig. 2 for example) with a maximum divergence that decreased to zero at the top and bottom of the layer. It was assumed that the divergence measured from the satellite image was at the level where the maximum was found using the sounding data. Using the satellite measured divergence and a model of its vertical structure, based on the soundings, the total LOF mass flux was calculated using slabs 20 mb thick.

To determine the mass flux through different layers in the region of vertical motion (LVM), the entrainment rate into the LVM had to be assumed. The entrainment rate, λ, is normally defined as:

$$\lambda = \frac{1}{M_c} \frac{dM_c}{dP} \tag{4}$$

where M_c is cumulus mass flux, and p is the pressure. From equation (4) we can integrate from the base of the outflow layer, P_{LOF}, downward to the base of any layer, P (assuming λ is constant) to derive the mass flux in the updrafts of the cloud system at all layers.

$$M_c(P) = M_c(P_{LOF}) \, Exp\left[(P - P_{LOF})\lambda\right] \tag{5}$$

From Austin and Houze (1973) a relation between the condensation rate, C, and the mass transport at any level, M_c (P), is given by:

$$C = \int_{P_{LIF}}^{P_{LOF}} M_c \left[\lambda(q_e - q_c) - \frac{dq_c}{dP}\right] dP \tag{6}$$

which represents the condensation due to cooling of the saturated air as it ascends, dq_c/dP, and the drying caused by air being entrained into the updraft, $\lambda(q_e - q_c)$. The mixing ratio for the environment, q_e, was determined from the soundings and the mixing ratio for the cloud, q_c, was assumed to be the saturation mixing ratio at the environmental temperature. The condensation in the outflow layer was small due to the low temperature and low mixing ratio at that level and was neglected.

The choice of entrainment rate obviously affected the calculated vertical mass flux and consequently the model's estimate of condensation inside the clouds. Sloss (1967) has shown for cumulus clouds that develop into thunderstorms, the entrainment rates range from -0.001 to

$-0.004\ mb^{-1}$. This study deals with thunderstorm systems that were made up of many individual storms of different sizes and at different stages in their life cycle. An average for the total system had to be used. To determine the possible range of results, the entrainment rate was varied from 0.0 to $-0.003\ mb^{-1}$ and the calculated condensation rates compared to the observed precipitation from rain gauges or radar.

3. Data Sources and Analysis

a. Satellite Data and Analysis

Satellite data for 20 May 1977 and 27 May 1979 were available from the Geostationary Operational Environmental Satellite (GOES-EAST) archived at the Space Science and Engineering Center at the University of Wisconsin-Madison. Rapid scan (3 min) full resolution (.8 km) visible and 8 km infrared data were available from 1700 GMT to 0600 GMT on 20 May 1977. On 27 May 1979 satellite data were available every 15 min from 2100 GMT to 0100 GMT. Satellite data for 30 May 1976 were obtained at 15 min intervals from 2130 GMT to 2345 GMT from the Goddard Space Flight Center, Greenbelt, Maryland at the same resolution. The area of interest covered by these data was centered on 35 degrees north latitude and 95 degrees west longitude, which allowed observations of the severe storms as they grew and moved across Oklahoma.

Satellite cloud winds have been shown in the past to be a reliable method for determining bulk properties of cloud clusters and divergence fields (Ninomiya, 1971; Hasler, 1972; Suchman et al., 1977; Wilson and Houghton, 1979). The anvil expansions were determined by tracking brightness anomalies as previously mentioned. These vectors were chosen to define the divergence rates of the wind field near the perimeter of the anvil. Motion vectors were derived using three consecutive satellite images

at 15 minute intervals. Each wind set overlapped with one image from the previous set to give consistency between sets.

The single pixel method (Smith and Phillips, 1972) was used to track the brightness features because of the human interaction needed in defining specific features in the anvil. Suchman and Martin (1976) have shown that the single pixel tracking method yields a small error (2 m s^{-1}) for derived upper level winds in the tropics and compares well with winds derived from conventional means.

Divergence rates were calculated from the changes in area of the isotherm contours on the infrared images. The differences between the two methods of measuring divergence and mass flux into the anvil, the kinematic method using visible images and the isotherm expansion on the infrared images, will be shown in the next section and discussed in section 6.

The height of the cirrus anvil was determined from the infrared temperature of the bulk of the anvil. Since cirrus anvils become thin at their edges, the heights of the motion vectors (visible image method) were assumed to be the same as the thicker, inward part of the anvil. A temperature averaged from several locations in the anvil outside of the vertically protruding towers was used. This temperature was compared to the soundings of the NSSL network to convert the satellite measured temperature to a height in mb.

b. Rawinsonde Data and Analysis

For the severe storms on 20 May 1977 and 30 May 1976, rawinsonde data were obtained from NSSL. Data from the rawinsonde stations in the network were available from 1930 GMT to 0300 GMT on 20 May 1977 and from 1500 GMT to 2330 GMT on 30 May 1976, both at 90 minute intervals. The stations were spaced at ~100 km intervals which encompassed most of the area of the

Texas. In southeastern New Mexico, a low pressure system (Fig. 3) developed ahead of a stationary front which extended from a cyclone in central Canada. The low pressure center intensified and slowly moved into the Texas panhandle. Southeasterly low level flow continued to bring warm moist air into southern Oklahoma and northern Texas. The 500 mb chart at 1200 GMT showed a large amplitude trough in the westerlies moving out of the southwest into Oklahoma.

Activity began about 1500 GMT near Lubbock, Texas and then slowly moved northeastward. The 1909 GMT satellite picture (Fig. 1) showed heavy activity in Texas and Oklahoma. At 2000 GMT the cells in Oklahoma begin to build in strength. At 2100 GMT numerous thunderstorms were observed ahead to the front. The NSSL network reported heavy rainfall associated with this activity. Numerous tornadoes were reported during the evening of 20 May and in the early morning of 21 May. Most storms caused moderate damage, but tornadoes at Altus and Tipton, Oklahoma produced heavy damage (Ray et al. 1977).

A total of 21 anvil expansion (divergence) analyses were made from 1715 GMT through 2215 GMT for Case I. The storm system was well developed at the beginning of the observation period and roughly conformed to a large-scale nephsystem (Ninomiya, 1971) with difluent flow over the entire region (Fig. 1).

The temperature determined from the infrared satellite image corresponded to a height of about 200 mb on the soundings available from the NSSL network. A comparison of anvil motion measurements (downwind edge) to rawinsonde wind reports from the NSSL network indicated the anvil motions corresponded to the 200 to 300 mb layer where the vertical shear also was small.

Divergence calculations were made from measurements of anvil motions by integrating around the polygon defined by the positions of the motion vectors. The area and divergence derived are plotted versus time in Figures 4 and 5 respectively. A linear increase in area over the entire period was apparent.

Past studies of anvil divergence rates by Adler and Fenn (1979) and Stout et al. (1979) used the growth rates of the 250K contour measured on the infrared images. For comparison to those studies,the anvil areas defined by the 273K, 250K, and 213K contours are shown in Figure 4. The areas within all three contours increased linearly with time. The 273K and 250K contours also grew at a faster rate than the 213K contour and the area defined by the motion vectors.

The mean divergence for the storm system decreased gradually with time (Fig. 5) mainly due to the increase in anvil area. An exponential curve was fit to the data using the least squares method. The scatter about the curve was small, 1.6 x $10^{-5}s^{-1}$, which was within the 95 percent confidence level. Values of divergence ranged from 2.8 x $10^{-4}s^{-1}$ (at a 4.0 x $10^{10}m^2$ area) to 7.2 x $10^{-5}s^{-1}$ (at a 24.0 x $10^{10}m^2$ area). This is similar to the divergence rates derived by Ninomiya (1971) from upper level winds over other severe storm systems.

It should be noted that these values of divergence are mean values defined over large areas (>$10^{10}M^2$). They should not be confused with values of divergence over individual cumulonimbi, which could be an order of magnitude larger.

To compare the past methods of measuring anvil divergence, equation (1) was applied to the area within the 250 K isotherm. The area at each 15 min

interval was derived from the linear equation used to fit the data to reduce scatter. The contour measured divergence also decreased with time but a greater rate than the motion vector measurements (Fig. 5) due to the larger total areas measured.

The divergences derived from the image measured motions applied to only one level in the outflow layer and thus the total divergence for the outflow layer had to be modeled as previously mentioned. In order to do this, the vertical structure of the environmental divergence calculated from the four available NSSL soundings for 2230 GMT by Park and Sikdar (1980) was used (Fig. 2). The profile shown in Figure 2 was taken at the end of the observation period, but it was representative of the storm period studied. According to Park and Sikdar (1980) the level of outflow was between the 350 mb and 150 mb surfaces, with a maximum at 205 mb. Convergence occured below this layer. From this profile we can infer that the vertical velocity increased in the lower layers reaching a maximum at 350 mb and then decreased to zero at 150 mb.

The mass flux diverging in the anvil was calculated by integrating from 350 mb to 150 mb in 20 mb increments using the motion vector measured divergence and the smooth vertical profile (Fig. 2) as described in section 2. The total mass flux (Fig. 6) increased exponentially with time from 1.65×10^{13} g s^{-1} at 1715 GMT to 3.06×10^{13} g s^{-1} at 2215 GMT.

These values were larger than found by all previous studies of storms. Braham (1952) for small air mass thunderstorms in Ohio and Florida found mass fluxes of 0.5×10^{11} g s^{-1}. For heavy Oklahoma thunderstorms Fankhauser (1966) calculated the fluxes to be around 2.8×10^{10} g s^{-1} while Auer and Marwitz (1968) found an average of 2.3×10^{11} g s^{-1} from 17 high

plains and one Oklahoma thunderstorm. Similarily, Newton (1966) calculated a flux of 7.0×10^{11} g s^{-1} for a single Oklahoma storm.

Satellite studies by Sikdar et al. (1970) estimated mass fluxes on the order of 10^{11} to 10^{12} g s^{-1} for an anvil area of $10^{10} m^2$. Auvine and Anderson (1972) calculated similar values and concluded that 10^{12} g s^{-1} was a typical value for a large intense thunderstorm in the mid-latitudes. For a tropical cloud cluster Lo (1976) calculated 10^{11} g s^{-1} using an anvil area on the order of 10^8 to 10^9 m^2.

Two reasons can be postulated for this storm being at least one order of magnitude larger than any of the past studies. The anvil area was on the order of 10^{10} -10^{11} m^2, which is a very large storm compared with past cases. Also the present model used an outflow layer thickness that was larger than the previous satellite studies by Sikdar et al. (1970) and Auvine and Anderson (1972). The parabolic profile used here was for a 200 mb thickness which roughly corresponded to 5 km compared to the 1 km used by the Sikdar studies.

Also shown in Figure 6 is the mass flux calculated from the expansion of infrared contours (250K). Since the contours expanded at a constant rate (Fig. 4) a constant mass flux was calculated (see eq. 1 and 3). The infrared method produced a mass flux estimate that was greater than the motion vector analysis at 1800 GMT but became very close to it at 2100 GMT (7% lower).

The total mass flux into the outflow layer (kinematic method) was used to draw the vertical profile of mass flux from the cloud base to the base of the outflow by equation (5). The entrainment rate for this storm system was varied from 0.0 mb^{-1} to -0.003 mb^{-1}. The total condensation rate for this storm system was calculated using (6) with the derived mass flux profiles

(Fig. 7). The actual and saturation mixing ratios were calculated from the NSSL soundings for 1924 GMT, 2100 GMT (Fig. 8) and 2230 GMT. The mixing ratio profiles were similar for the three time periods, but the earlier time period was somewhat drier in the lower layers below 700 mb (not shown). The mixing ratios were interpolated to 15 min. time intervals for the condensation calculations.

The volumetric condensation rate increased from 1715 GMT to 2000 GMT, leveled off, and then decreased slightly after 2145 GMT. These changes reflected the changes in mass flux estimates and mixing ratio profiles used over the time period. The model was sensitive to the vertical structure of the moisture profile in addition to the total amount of water vapor present. Increasing the entrainment rate caused the curves to retain their basic shape, but flatten out and decrease in value. More water vapor was needed to saturate the entrained air for the higher entrainment rates. If the infrared mass flux estimates had been used, more constant condensation estimates would have been produced that would have decreased slightly in time rather than increase as shown.

In order to compare the model's estimated volumetric condensation rates with what was actually observed as precipitation on the ground, hourly precipitation data were used. Obviously a one to one comparison can not be made using the precipitation data because of the time between observations and the spacing between the gauges. An average hourly trend was used for comparison. The hourly precipitation increased over the time period studied. The volumetric condensation rate calculated for a large entrainment of -0.003 mb^{-1} was less than the observed precipitation rates at 2100 GMT and 2200 GMT indicating that a lower entrainment rate was more realistic. Park and Sikdar (1980) derived an entrainment rate of -0.002 mb^{-1} for one storm inside this

system from their rawinsonde budget studies. Therefore we will use this value in the next section for comparisons with the other storms.

b. Case II: 30 May 1976

An extremely unstable air mass over Texas and Oklahoma, with lifted indices between -8 and -12 existed ahead of a major shortwave at 500 mb in western New Mexico. Strong divergent flow aloft over Oklahoma was accompanied by a jet maximum at 300 mb over central Texas. On the 2100 GMT surface map (Fig. 9), a low pressure system was centered over southwest Texas. A stationary front extended from Illinois through eastern Kansas, Oklahoma, and north through New Mexico. A southeasterly low level flow brought warm moist air into southern Oklahoma from the Gulf of Mexico. The low pressure system began to deepen at 2100 GMT and thunderstorm activity developed in northern Texas and southern Oklahoma. Two convective systems were evident on the satellite images (Fig. 10). As the activity built northward, severe thunderstorms were reported at Norman, Oklahoma by 2315 GMT. The low continued to deepen at 0000 GMT 31 May, and widespread thunderstorms developed in Oklahoma along the stationary front.

Most severe weather reports came from the convective area southwest of Norman Oklahoma (Alberty et al., 1976). Our analyses were confined to the first convective system that developed south of Norman at 2130 GMT and moved northeast. This is the cloud mass on the right in Figure 10. A total of five divergence analyses were made for Case II from 2200 GMT to

2300 GMT. Winds north of the storm were southwesterly at 15-20 ms^{-1} at the anvil level increasing to 25 ms^{-1} in the vicinity of the storm. A 20-25 ms^{-1} westerly flow also was present south of the storm. The southwestern or upwind side of the storm appeared to be stagnant on the satellite images and most of the anvil expansion took place downwind.

The upper level winds at 2200 GMT from a RAOB released in the southern part of the storm at station EMC of the NSSL network indicated that the measured cloud motions conincided with the winds from 300 mb to 150 mb. The wind shear in this layer was small. The satellite infrared temperature of the anvil cloud corresponded to a height of about 210 mb on the NSSL sounding.

The divergence measurements for Case II were not as strong as Case I. The almost circular shape of the anvil in the satellite pictures (Fig. 10) also indicated that the vertical wind shear was very small. At 2200 GMT the vertical wind shear was about 1.5×10^{-3} s^{-1} from the sounding data.

The areas measured by the 273 K, 250 K, and 213 K contours and the motion vectors increased linearly with time from 2200 GMT to 2300 GMT (Fig. 11). These areas were on order of magnitude smaller than Case I.

The kinematic divergence from the upper level winds decreased with time (Fig. 12) as was the case for Case I. An exponential curve was fit to the data by the least squares method. The divergence ranged from 8.6×10^{-4} s^{-1} (6.0×10^{9} m^2 area) to 4.1×10^{-4} s^{-1} (2.6×10^{10} m^2 area). Unlike Case I, where the storm developed into a large-scale nephsystem, Case II remained a mesoscale system during the time of observation. This

was apparent by the smaller area of the anvil and magnitude of the divergence. Divergences calculated from the contour expansion method again were smaller than the kinematic method.

The vertical profile of environmental divergence was calculated for 2200 GMT from selected soundings from the NSSL network (Fig. 13). The profile shows that an upper level divergence layer existed between the 8.0 km (370 mb) and 15.4 km (117 mb), with a maximun divergence of $1.9 \times 10^{-4} s^{-1}$ at 11.5 km (220 mb). Convergence existed from the surface to 750 mb with small divergence from 660 to 370 mb. The layer between 9.4 km (300 mb) and 14.7 km (135 mb) was chosen as the outflow layer. A smoothed profile was made from these data for use in the anvil divergence calculations (dashed line, Figure 13).

The total mass flux into the outflow layer was plotted versus time in Figure 14. The values of mass flux were an order of magnitude smaller than those for the Case I (Fig. 6). This is realistic because we were dealing with a storm system on a much smaller scale ($10^9 - 10^{10}$ m^2 compared to $10^{10} - 10^{11}$ m^2 for Case I.) The values ranged from 5.2×10^{12} g s^{-1} at 2200 GMT to 11.3×10^{12} g s^{-1} at 2300 GMT. These values are typical for a thunderstorm system in the midlatitudes (Auvine and Anderson, 1972).

Also shown in Figure 14 is the mass flux estimated from the infrared contour measurements of anvil expansion. This method produced a constant mass flux over the period studied because of the constant rate of areal expansion as also was found in Case I. In the initial stage of the anvil (2200 GMT) the contour mass flux estimate was twice as large as the motion vector analysis. However, after one hour (2300 GMT) the two were nearly identical.

The vertical structures of the actual and saturation mixing ratios were determined from the soundings at station EMC at 2200 GMT and 2300 GMT. An average profile for each mixing ratio was determined for the time of observation and plotted in Fig. 15. These profiles showed that the lower layer of the atmosphere (below 700 mb) was quite dry.

For the time period studied, the volumetric condensation rates (Fig. 16) continuely increased as in Case I. At the higher entrainment rates the curves flatten out and the values became small.

Because the storm did not cross most of the NSSL rain gauges we used the 10 cm WSR-57 radar at Norman, Oklahoma for data on the volumetric rainfall rate during the period studied (Fig 16). The volumetric rainfall rate slowly increased with time, but was considerably smaller than any of the derived condensation rate values. This was probably due to the very dry air in the lower levels as depicted by the mixing ratio profiles, Figure 15. The dry environment may have evaporated a lot of the rain as it fell.

Hourly precipitation data from the synoptic rain guage network were plotted and analyzed for Case II, however only one rain gauge reported precipitation under this storm from 2200 to 2300 GMT. A rate of 0.5 cm h^{-1} was reported during this time which compared well with radar derived intensity of 0.589 cm h^{-1} for the same time period. This shows, as is commonly seen, that a severe convective storm may go undetected by the normal synoptic rain gauge networks.

c. Case III: 27 May 1979

On 27 May 1979 an unstable air mass, combined with weak surface convergence with a minor upper air disturbance came into phase over west

and central Oklahoma and caused intense afternoon storm activity. The 1800 GMT surface map (Fig. 17) showed a stationary front extending from the east coast through southern Illinois, Missouri, and through central Oklahoma. A developing low pressure system was positioned southwest of Texas.

By 2000 GMT several thunderstorms had developed along an east-west line through central Oklahoma near the stationary front. These cells soon dissipated and a new line of intense thunderstorms developed southeast of Norman, Oklahoma at 2100 GMT (Fig. 18). Strong updrafts and large hail were reported by plane. Golf ball size hail was reported near ADA at 2220 GMT (Alberty et al., 1979). We studied the convective system southeast of Norman from 2115 GMT to 2300 GMT.

Eight upper level wind sets were derived for Case III. The winds aloft for this storm case were weak compared to the two previous cases. A southwest flow of 15 ms^{-1} southwest of the storm was measured from cirrus motions. A mesoscale difluent flow existed over the storm area during the entire period of observation. The downwind side of the anvil moved at speeds of 20 to 25 ms^{-1} northeastward while the upwind side exhibited little motion. This anvil appeared to diverge in the same manner as Case II.

The anvil motions and other cirrus near the storm coincided with the 200-300 mb winds measured by the NSSL rawinsonde at station ADA. Little wind shear was reported in this layer by the rawinsonde. The infrared satellite image gave a temperature of 213 K for the cirrus anvil which corresponded to a height of about 200 mb on the soundings.

The divergence and anvil area calculated using the kinematic method

yielded results similar to Case II. The area increased linearly with time (Fig. 19) using both the kinematic and contour methods The 273 K and 250 K contours were larger than the area of the motion measurements while the 213 K contour was nearly the same.

Divergence values in Figure 20 derived from kinematic vectors ranged in value from 11 x 10^{-4} s^{-1} (1.25 x 10^{9} m^{2} area) to 4.25 x 10^{-4} s^{-1} (15 x 10^{9} m^{2} area) which also was similar to Case II.

An attempt was made to use data from the SESAME field-processed rawinsonde data. Unfortunately the location and the timing of several of the soundings used in the computation were not compatible with the location and occurrence of the storm. The divergence profile calculated from the available soundings (EMC, ADA, SUD, TVY, OUN) indicated convergence in the upper levels, implying sinking motion. It was apparent that the majority of the soundings were in clear air well outside of the storm.

The divergence profile derived for Case II was used to model the upper level cloud divergence profile for Case III. Of the past two cases studied, Case II was similar to Case III, in terms of the life cycle during the time of observation and size of the storm.

The total mass flux derived for Case III is shown in Fig. 21. The motion vector mass flux increased over the entire period and ranged in value from 6.0 x 10^{11} g s^{-1} at 2115 GMT to 7.0 x 10^{12} g s^{-1} at 2300 GMT while the contour area derived value remained constant at 5.5 x $(10)^{12}$ g s^{-1}. These values are similar in magnitude to Case II and also typical for mid-latitude storms as previously mentioned in section 4.a.

The mean environmental and saturation mixing ratios were calculated for the period studied using four raob stations outside of the storm (Fig. 22). The condensation rates for different values of entrainment are

shown in Fig. 23. The volumetric condensation rate increased during the time of observation as in Case II.

Data from WSR-57 radar at Norman, Oklahoma were used to determine a volumetric rainfall rate for the storm. As in the other cases the measured rainfall increased in time but at a rate less than the model estimated condensation rates.

5. Comparisons of the Three Storm Cases

a. Anvil divergence rates

To compare the intensities of the three storm cases, the divergences derived from the upper level winds for each storm are plotted versus anvil area on Fig. 24. The magnitude of divergence was dependent on the given cloud area (anvil area). Cases II and III were both observed during the early stage of the mature thunderstorm while Case I was observed at a later stage when the cloud area was larger than the other two cases. Case I divergence decreases gradually with increasing area while Cases II and III decreased sharply illustrating the general relationship between cloud area and divergence. It was not possible to obtain data on Case I when it was the same size as the other two. From Fig. 24 it is evident that the magnitude of the divergence for Case II was greater than III for the same cloud area implying that Case II was a stronger storm.

b. Rainfall Intensities

Rainfall intensity is a measure of storm severity by which the storms can be compared (Fig. 25). Case II produced the largest rainfall rates. A quantitative comparison with Case I was difficult because radar data were not available for I and raingauge data were not available to calibrate the radar data used for Cases II and III. According to Wilson and Brandes (1979) the Z-R relationships used for radars can vary up to a factor of 2 which implies that the inter-storm differences in rain rates shown here are only tentative indicators of what existed.

For Case I the rainfall intensity increased during the long period that is was monitored. At 2100 GMT it was close to the level of Case II even though II was a young storm at this time while Case I had existed for over 5 hours. It appeared that Case I had a large moisture supply from which it was able to draw from, while II and III showed decreases in rainfall intensities after the first hour.

c. Estimated Condensation Rates

The volumetric condensation rates estimated by the model also can be used as an index of storm intensities. In order to compare the storms, the volumetric condensation rates had to be converted to areal rates by dividing by the area of the precipitation. For Cases II and III the area was defined using the 12 dbz reflectivity on the radar image of the lowest altitude scan. For Case I a "hand smoothed" analysis of the rain gauges was used for the areal measurements. A constant entrainment rate of $-0.002\ mb^{-1}$ was applied to all three storms for comparison purposes (Fig. 26).

The model estimated condensation rates indicate that Case II was stronger than the other two storms. The differences between Cases II and III are in general agreement with the measured rainfall intensities (Fig. 25).

The condensation intensity estimated for Case I also was smaller than expected from the measured rainfall intensities. This is believed to be a side effect of using the rain gauges to measure the area of rainfall rather than the radar echoes. Uniform coverage between gauges was assumed which may not have existed over the large area of the storm. If the areal extent of the rain were overestimated, then the condensation intensity in Figure 26 may have been underestimated.

d. Precipitation Efficiencies

An additional way of comparing storms is by estimating their efficiencies of rain production. The precipitation efficiency of storms has had several definitions in the literature. It can be defined using either the total amount of water vapor converging on the cloud system at all levels or only the moisture entering through the cloud base (Marwitz, 1972). Because most of the moisture resides at the lowest levels in the atmosphere these differences cause only small differences in the resulting calculations. In this study we defined the precipitation efficiency (PE) to be the measured volumetric rainfall rate divided by the estimated condensation rate. Our

definition includes the moisture at all levels in the atmosphere. Because this is a volumetric calculation it was less dependent of the measurements of rain area than the condensation intensity parameter previously discussed.

Braham (1952) calculated an efficiency of 19% for small air mass thunderstorms in Ohio and Florida. On the other hand, Newton (1966) calculated an efficiency of 48% for a large Oklahoma storm. Austin and Houze (1973) have noted that the condensation rate can range from 2 to 10 times larger than the cellular rainfall, the average being between 3 to 4. They chose to use an efficiency of 33% in their model as the best estimate with an uncertainty of ±33%. This value neglected the effects of the downdraft.

Using our model we found the PE to vary from 6 to 60% (Table 1). The choice of entrainment obviously affected the PE calculations. Higher entrainments produced higher estimates of PE because more dry air from above the boundary layer was assumed to be drawn into the clouds. For a constant entrainment of $-0.002\ mb^{-1}$ the PE was estimated to vary from 17 to 60% for the three storms. Case I being the most efficient while II was the least efficient. This ranking between cases partially corresponds to the environmental humidity profiles (Figures 8, 25, 22 and Table 1 summarized in Table 2). However, it reflects the relative humidity differences at 850 mb between cases more than the surface relative humidities or mixing ratios.

6. Discussion and Conclusions

This study of three storms was made to improve our understanding of how anvil expansion measurements made from satellite images are related to convective storm intensities and rainfall. Our findings are as follows:

a. The anvil divergence measurements and the mass flux estimates calculated from them were sensitive to the type of method used (the kinematic method or the contour method) in the initial stage of the storms. The anvil area measurements from the isotherm contour areas on the infrared pictures increased at a linear rate in time implying that the vertical mass flux into the anvil was constant during the time period studied. In contrast, the kinematic method of motion tracking on the visible pictures produced mass flux estimates that increase in time at a logarithmic rate. When the anvils reached large areas in the latter stage of their life, the kinematic mass flux estimates approached a constant and agreed with the infrared contour estimates (within 20%).

The anvil area measurements gave the impression that the 213K contour replicated the divergence measurements derived from the motion vectors. For Cases I and III (Figs. 4 and 19) this contour had an area that was nearly equal to the area described by the motion vectors. The 213K contour obviously represented a smaller part of the anvil than the 250K and 273K contours (Figs. 1 and 18). But for Case II the area of the 213K contour was closer to the warmer contours (Figs. 11). While it appears that some infrared contour could be found that would replicate the motion vector analysis, this temperature may vary between storms. Most studies using satellite images (Adler and Fenn, 1979, Wylie, 1979, Stout et al., 1979, Griffith et al., 1981 and 1978) selected a temperature near 250K so that they would measure the area of the entire anvil and not have variations from the height differences of the central portions of the anvils. They picked a temperature that was substantially warmer than the center of the anvil but was cold enough to eliminate lower clouds that were not associated with the anvil. For this reason we used the 250K contour for comparison to our motion vector analyses.

Our preference was the kinematic method because two of the three cases studied exhibited rain rates that increased with time. In contrast, the constant mass flux of the infrared method implied that the condensation rates and rain rates should have remained constant in time. Thus the kinematic method more realistically modelled the time changes of the storms.

Along the same lines, the choice of anvil thickness or the vertical profile of divergence in the outflow layer also are important parameters which affect mass flux calculations. We modified the past efforts in using satellite derived anvil divergence measurements by employing rawinsonde budget calculations for determining divergence profiles. If this model is to be used operationally, the budget studies may not always be available and thus information on how the vertical divergence profiles vary between convective systems will be needed.

b. Rainfall rates tend to be a function of the moisture environments of the clouds if averaged over the total areas of the convective systems. This relationship has been found by other studies of rainfall rates (Zawadaki and Ro, 1978, Wylie, 1979, and Griffith et al., 1981) and the same trend appeared in the data presented in this paper (see Table 2). This relationship is important and should be considered when satellites are used to estimate rainfall.

c. The choice of entrainment rate was important in modeling the cloud budgets. Our inter-storm comparisons indicated that this parameter was not a simple constant for all large storms. While entrainment rates have been related to cell sizes in the past literature, little information is available on large multi-cell systems and this information is needed in order to make quantitative calculations from properties measured on satellite images.

With the use of the present high speed computer systems, such as McIDAS, this technique has the potential for realtime analysis of severe convective storm systems. The intensity of the storm could be determined by the rate of expansion of the cirrus anvil and the intensity of the condensation produced by the model. The flash-flood potential of a storm system could be determined from the amount of condensation produced by the model, the motion of the storm system as seen in sequence of satellite images, and the regeneration of new convection in the storm area.

REFERENCES

Adler, R.A. and D.D. Fenn, 1979: Thunderstorm intensity as determined from satellite data. J. Appl. Meteor., 18, 502-517.

Alberty, R. L., J. Weaver, D. Sirmans, J. Dooley, B. Bumgarner, 1976: Spring Program '76: Section I. Meteorological summary. NOAA Tech Memo ERL-NSSL-83, 130 pp. Nat. Tech. Info. Ser. PB-280 745.

Alberty, R. L., D. W. Burgess, C. E. Hane, and J. F. Weaver, 1979: SESAME 1979 operations summary. NOAA ERL, Boulder, Co. Available from the U. S. Govn't. Printing Office No. 1979-677-072/1303 REG8. or Nat. Tech. Info. Ser. PB80-119902.

Auer, Jr. A.H. and J.D. Marwitz, 1968: Estimates of air and moisture flux into hailstorms on the High Plains. J. Appl. Meteor., 7, 196-198.

Austin, P.M. and Houze Jr. R.A., 1973: A technique for computing vertical transports by precipitating cumuli. J. Atmos. Sci., 30, 1100-1111.

Auvine, B. and C.E. Anderson, 1972: The use of cumulonimbus anvil growth data for inferences about the circulation in thunderstorms and severe local storms. Tellus, 4, 300-311.

Braham, R.R., 1952: The water and energy budgets of the thunderstorm and their relation to thunderstorm development. J. Meteor., 9, 227-242.

Frankhauser, J.C., 1966: Some physical and dynamical aspects of singular cumulonimbus observed by instrumented aircraft and radar. Proc. Twelfth Conf. Radar Meteor., Boston, Amer. Meteor. Soc., 405-413.

Griffith, C. G., W.L. Woodley, P.G. Grube, D.W. Martin, J. Stout, and D.N.Sikdar, 1978: Rain estimation from geosynchronous satellite imagery-visible and infrared studies. Mon. Wea. Rev., 106, 1153-1171.

Griffith, C. G., J. A. Augistine, and W. L. Woodley, 1981: Satellite rain estimation in the U. S. high plains. J. Appl. Met., 20, 53-66.

Hasler, A. F., 1972: Properties of tropical cloud clusters determined from geostationary satellite pictures. Ph. D. thesis, University of Wisconsin. Availavle from the University of Wisconsin Libraries, 728 State St., Madison, Wisc. 53706.

Lo., C. S., 1976: Using satellite imagery to determine the mass transport of individual cells in a GATE cloud cluster. M. S. thesis, University of Wisconsin-Madison. Available from the University of Wisconsin Libraries, 728 State St., Madison, Wisc. 53706.

Marshall, J.S. and W.M. Palmer, 1948: The distribution of raindrops with size. J. Meteor., 5, 165-166.

Marwitz, J. D., 1972 : The structure and motion of severe hailstorms. Part III: Severely sheared storms. J. Appl. Meteor., 11, 189-201/

Newton, C. W., 1966: Circulations in large sheared cumulonimbus. Tellus, 4, 699-712.

Ninomiya, K., 1971: Dynamical analysis of outflow from tornado-producing thunderstorms as revealed by ATS III Pictures. J. Appl. Meteor., 10, 275-295.

Park, S. and D. N. Sikdar, 1980: An application of a simple diagnostic cloud model to the May 20, 1977 storms over the Oklahoma meso-network. Tellus, vol. 32, 326-339.

Probert-Jones, J. R., 1962: The radar equation in meteorology. Quart. J. Roy. Meteor. Soc., 88, 485-495.

Ray, P. S., J. Weaver, and the NSSL Staff, 1977: Spring program summary (1977). NOAA Tech. Memo. ERL-NSSL-84, 173 pp. Nat. Tech. Info. Ser. PB-284 953.

Scofield, R. A., and V. S. Oliver, 1977: A scheme for estimating convective rainfall from satellite imagery. NOAA Tech. Memo. NESS 86, 47 pp. Nat. Tech. Info. Ser. PB-270 762.

Sikdar, D. N., V. E. Suomi, and C. E. Anderson, 1970: Convective transport of mass and energy in severe storms over the United States-An estimate from a geostationary altitude. Tellus, 5, 521-532.

Sikdar, D. N. 1972: ATS-3 observed cloud brightness field related to a meso-to-subsynoptic scale rainfall pattern. Tellus, 24, 400-413.

Sirmans, D. and R. J. Doviak, 1973: Meteorology radar signal intensity estimation. NOAA Tech. Memo. ERL-NSSL-64, Norman, Okla. 80 pp. (Available from NTIS, No. COM-73-1192312AS.)

Sloss, P. W., 1967: An empirical examination of cumulus entrainment. J. Appl. Meteor., 6. 878-881.

Smith, E. and D. Phillips, 1972: Automatic cloud tracking using precisely aligned digital ATS pictures. IEEE Trans. on Computers, C-21(17), 715-729.

Smith, E. A., 1975: The McIDAS system. IEEE Trans. on Geosci. and Electronics., GE-13, 123-236.

Stout, J., D. W. Martin, and D. N. Sikdar, 1979: Estimating GATE rainfall with geosynchronous satellite images. Mon. Wea. Rev., 107, 585-598.

Suchman, D., D. W. Martin and D. N. Sikdar, 1977: Deep convective mass transports: An estimation from a geostationary satellite. Mon. Wea. Rev., 105, 943-955.

Suchman, D. and D. W. Martin, 1976: Wind sets from SMS images: An assessment of quality for GATE. J. Appl. Meteor., 15, 1265-1278.

US Weather Bureau, Staff Members of National Severe Storms Project, 1963: Environmental and thunderstorms structures as shown by National Severe Storms Project observations in spring 1960 and 1961. Mon. Wea. Rev., 91, 271-292.

Weickman, H. K., A. B. Long, and L. R. Hoxit, 1977: Some examples of rapidly growing oceanic cumulonimbus clouds. Mon. Wea. Rev., 105, 469-476.

Wilson, J. W., and E. A. Brandes, 1979: Radar measurement of rainfall- a summary., Bull Amer Met Soc., 60,1048-1058.

Wilson, T. A. and D. D. Houghton, 1979: Mesoscale wind fields for a severe storm situation determined from severe storm satellite cloud observations. Mon. Wea. Rev., 107, 1198-1209.

Woodley, W., C. G. Griffith, J. S. Griffin, and G. C. Stromatt, 1980: The inference of GATE convective rainfall from SMS-I imagery. J. Appl. Met., 19, 388-408.

Wylie, D. P., 1979: An application of a geostationary satellite rain estimation technique to an extratropical area. J. Appl. Meteor., 18, 1640-1648.

Zawadzki, I. I., and C. U. Ro, 1978: Correlations between maximum rate of precipitation and mesoscale parameters., J. Atm. Sci., 17,1327-1334.

Table1

The Precipitation Efficiencies (measured rainfall/moisture converging on system) averaged over the time periods studied for each convective system.

CASE I

Entrainment Rate λ (mb^{-1})	Precipitation Efficiency $\overline{PE}$ x 100(%)
0.0	24
-0.001	38
-0.002	60

CASE II

λ (mb^{-1})	$\overline{PE}$ x 100(%)
0.0	6
-0.001	11
-0.002	17
-0.003	29

CASE III

λ (mb^{-1})	$\overline{PE}$ x 100(%)
0.0	14
-0.001	22
-0.002	36
-0.003	57

Table 2

Average Water Vapor Mixing Ratios, relative humidities for the 3 cases studied. For comparison, the average measured rainfall intensities also are given for the time periods studied.

	Surface		850 mb		
	Mixing Ratio	Relative Humidity	Mixing Ratio	Relative Humidity	Average Rainfall Intensities
Case I	15 g kg^{-1}	81%	11 g kg^{-1}	79%	6.5 cm h^{-1}
Case II	15	74	10	57	7.2
Case III	13	57	9.5	66	4.3

Acknowledgements

This research was done as partial fulfillment for the degree of Master of Science at the University of Wisconsin at Milwaukee under the supervision and guidance of Professor D. N. Sikdar and supported by NSF Research Grant Number ATM-7724842. The authors wish to thank Dr. Soon-Ung Park of the University of Wisconsin-Milwaukee and Dr. Robert Adler of the Goddard Space Flight Center (NASA) for their many helpful comments and suggestions during the course of this research. The satellite data used in this research was obtained from the Space Science and Engineering Center; Madison, Wisconsin and the Goddard Space Flight Center; Greenbelt, Maryland. The upper air data and radar data was furnished by Bill Bumgardner of the National Severe Storms Laboratory in Norman, Oklahoma.

List of Figures

Fig. 13. The vertical profile on environmental divergence derived from soundings from the NSSL network at 2200 GMT on 30 May 1977. Dashed line is smoothed profile.

Fig. 14. The total mass flux into the outflow layer as derived by the model for Case II plotted versus time. The curve is subjectively drawn (solid line). Dashed lined indicates the mass flux estimates from the isotherm contour measurements.

Fig. 15. The average actual mixing ratio, q_e, and saturation mixing ratio q_s, from station EMC at 2230 GMT for Case II.

Fig. 16. The volumetric condensation rates produced by the model (Kinematic method) for different entrainment rates and the radar derived volumetric rainfall (dashed line) plotted versus time (Case II).

Fig. 17. The 1800 GMT surface map for 27 May 1979 (Case III).

Fig. 18. The 2215 GMT full resolution visible satellite image for 27 May 1979 (Case III). Contours depict isotherms from the infrared image.

Fig. 19. Cirrus anvil area derived from isotherm expansion (dashed lines) and wind vector positions on the visible image (solid line) versus time (Case III). The rates of areal expansion are shown in ( ).

Fig. 20. Kinematic cloud divergence (solid line) derived from the motion measurements and divergence derived from the expansion of the 250 K isotherm (dashed line) plotted versus time (Case III).

Fig. 21. The total mass flux into the outflow layer as derived by the model (Case III) plotted versus time. The curve is subjectively drawn. Dashed line indicates the mass flux estimated from the isotherm contour measurements.

Fig. 22. The average actual mixing ratio, q_e, and saturation mixing ratio , q_s, at 2200 GMT (Case III).

Fig. 23. The volumetric condensation rates produced by the model (Kinematic method only) for different entrainment rates and the radar derived volumetric rainfall (dashed line) plotted versus time.

Fig. 24. The divergence derived from the motion vectors for each storm case plotted versus anvil area.

Fig. 25. The rainfall intensities for each storm case plotted versus time. Case I was derived from hourly synoptic rain gauges and Case II and III were derived from radar observations.

Fig. 26. The condensation rate derived from the model with an entrainment of -0.002 expressed as an intensity (cm hr^{-1}) plotted versus time for each case.

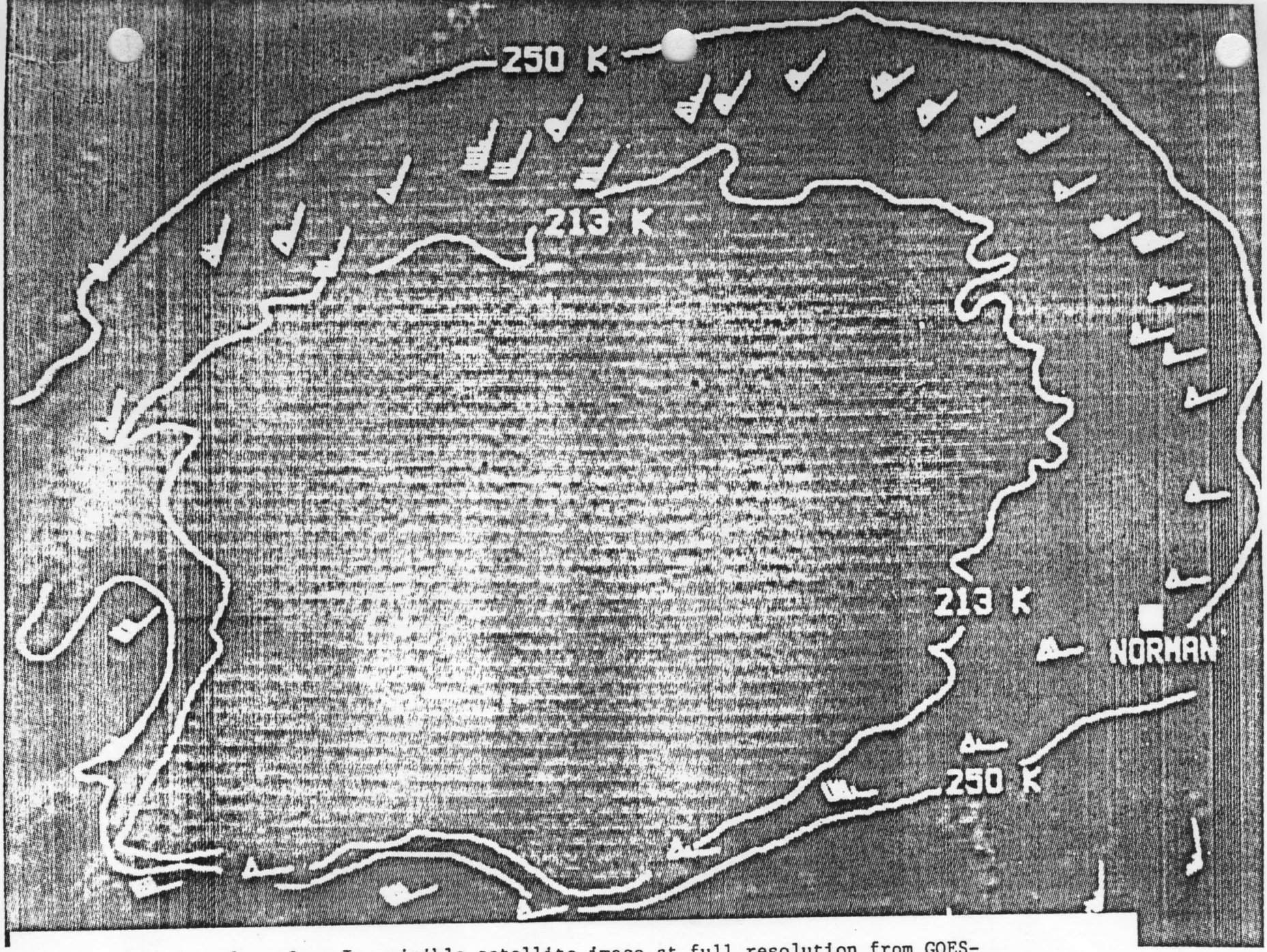

Fig. 1. Case I: visible satellite image at full resolution from GOES-EAST on 20 May 1977 at 1909 GMT. The contours indicate infrared measured temperatures. Meteorological flags indicate the motion vector analysis (knots) made from tracking brightness anomalies on visible pictures.

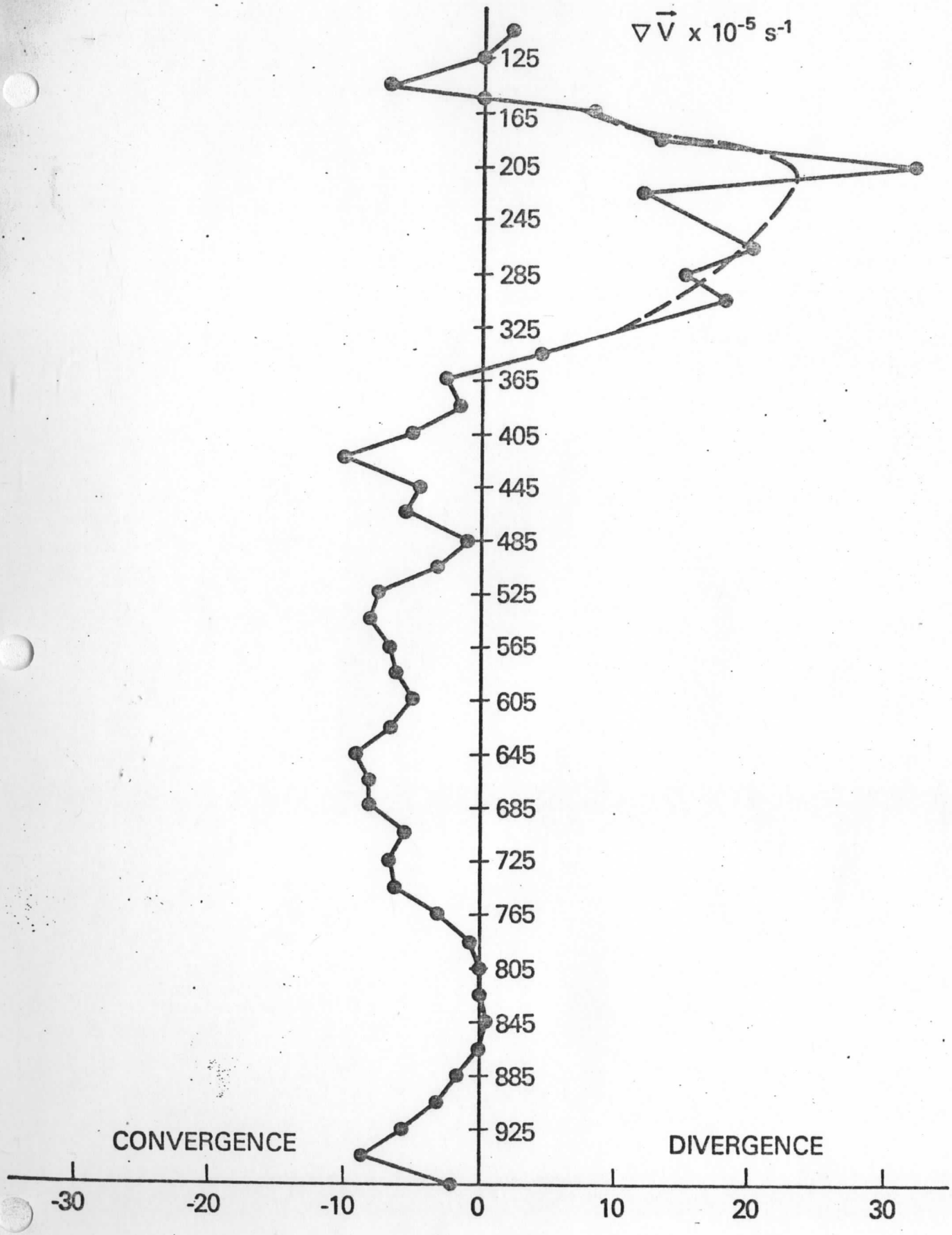

Fig. 2. The vertical profile of environmental divergence derived from soundings from the NSSL network at 2230 GMT on 20 May 1977 (from Park and Sikdar, 1980). Dashed line is the smoothed profile.

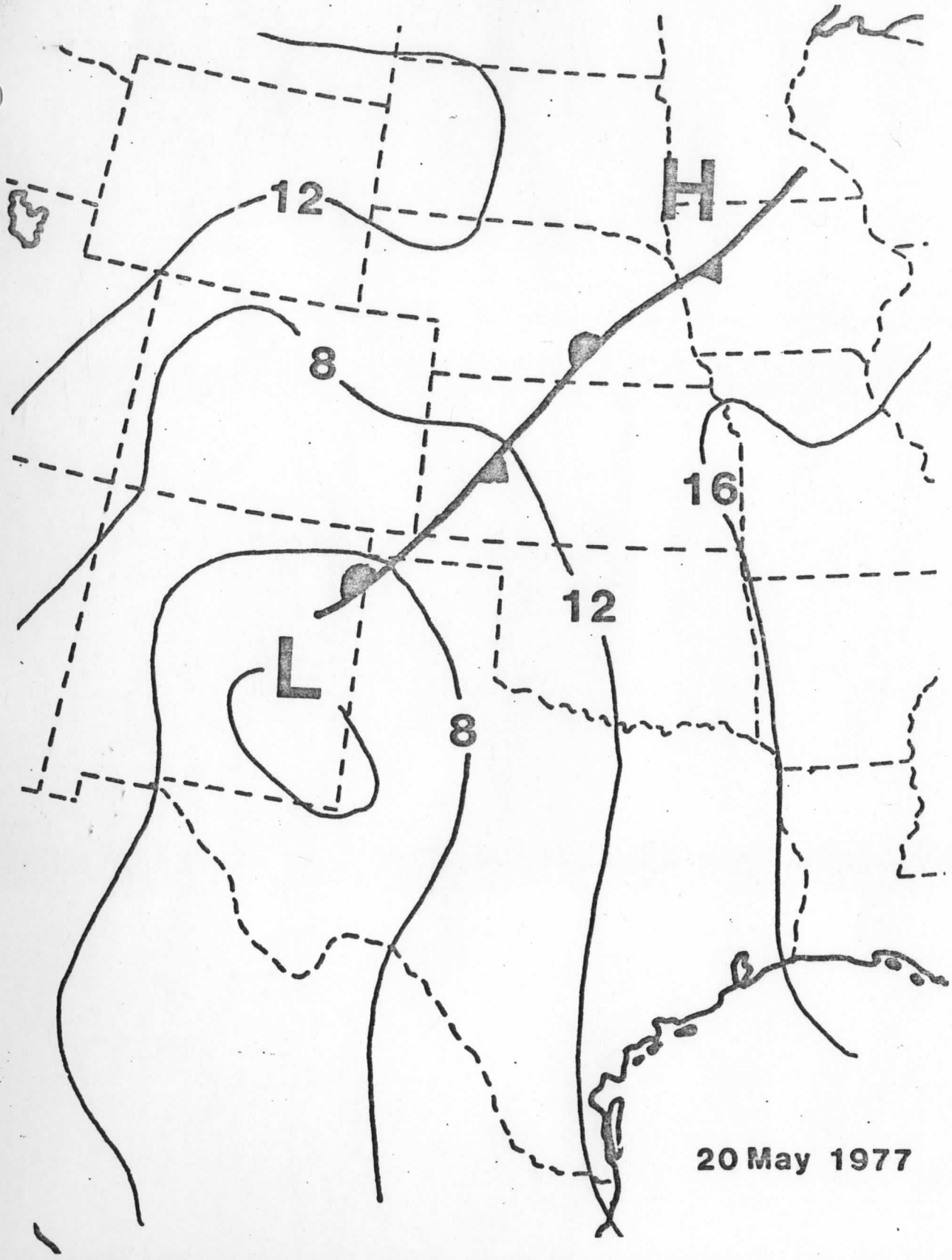

Fig. 3. The synoptic map for Case I (20 May 1977), at 1800 GMT.

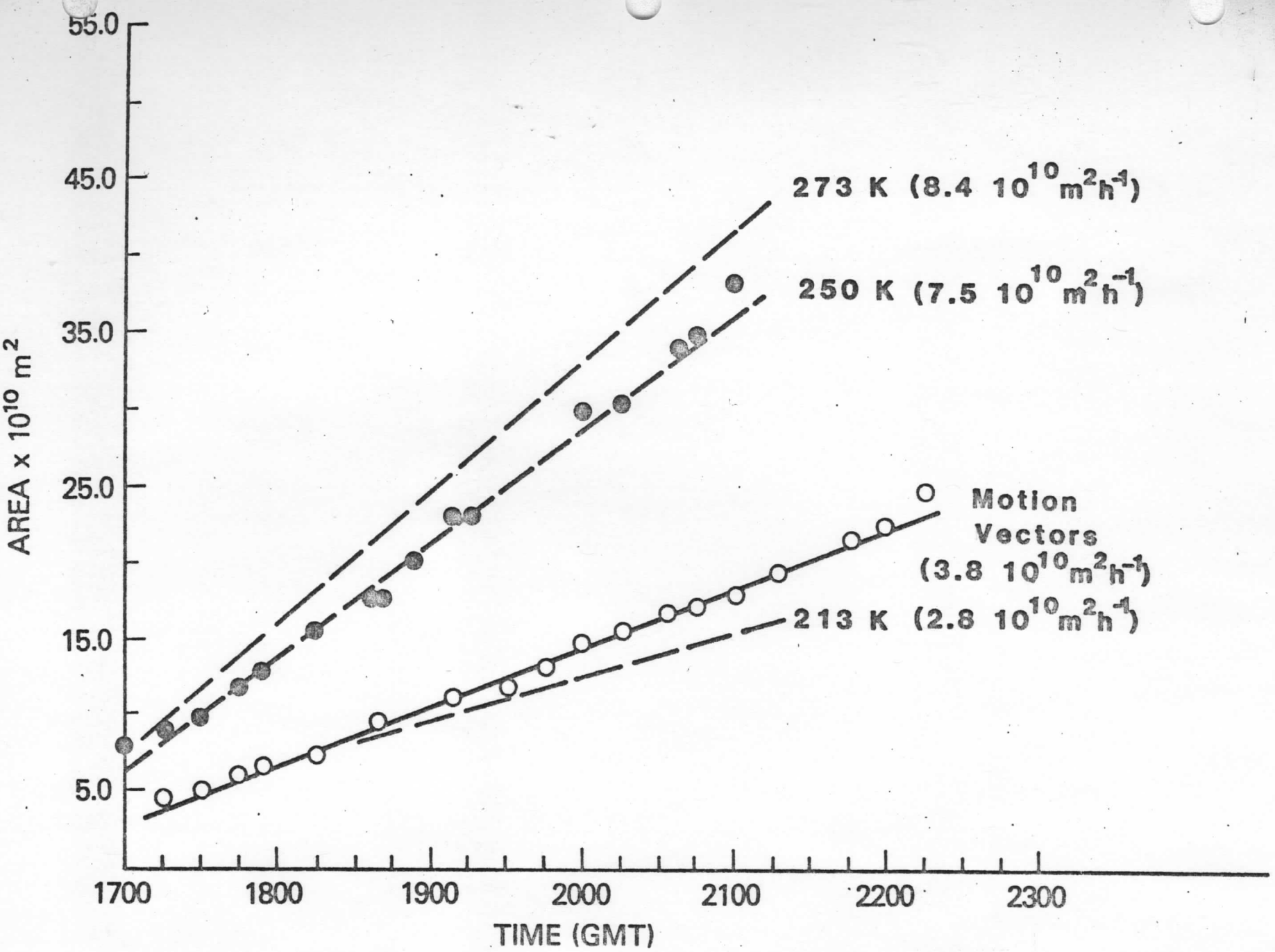

Fig. 4. Cirrus anvil area derived from isotherm (contour) expansion (dashed lines) and motion vector positions on the visible image (solid line) versus time (Case I). The rates of areal expansion are shown in ( ).

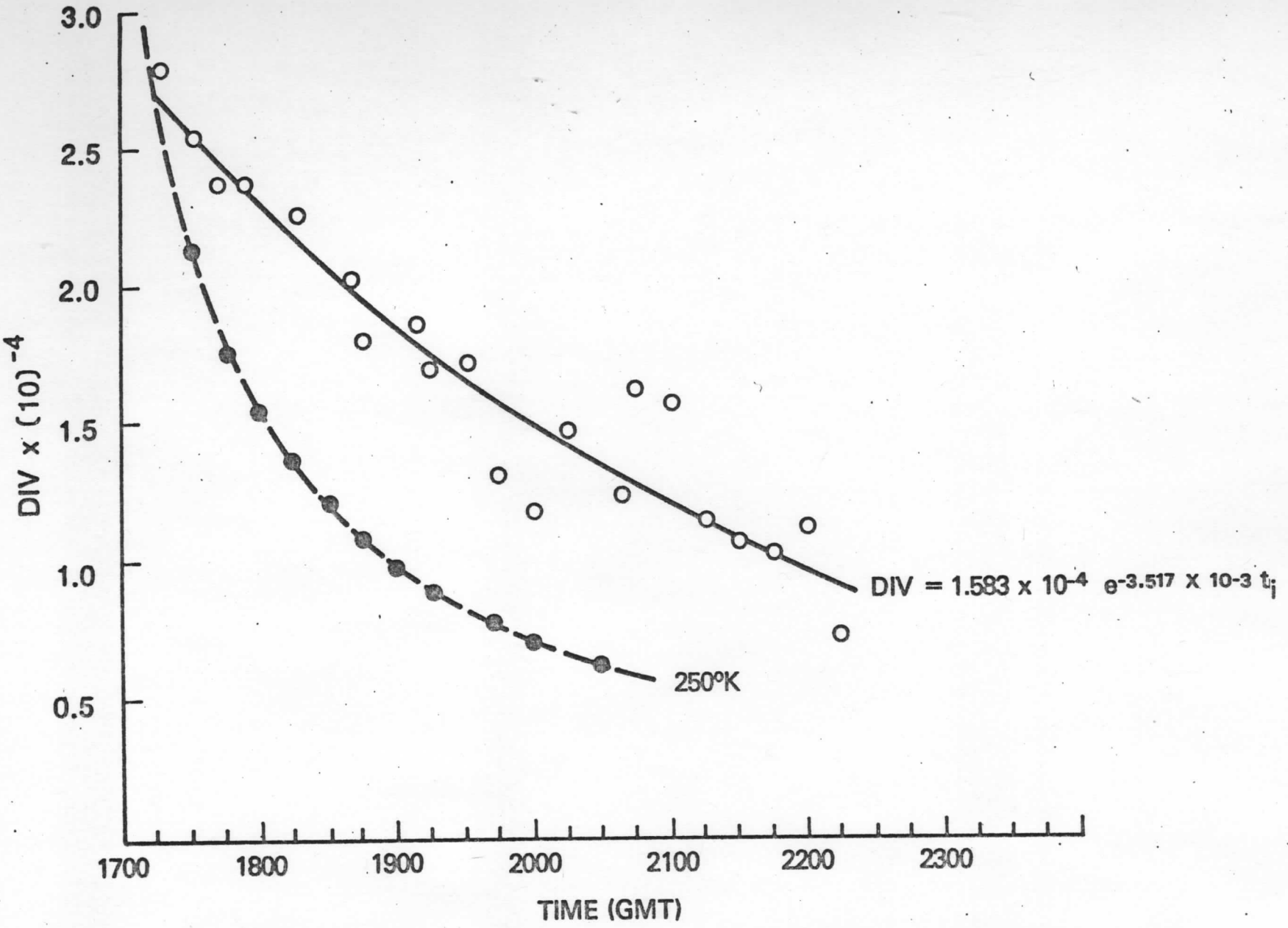

Fig. 5. Kinematic cloud divergence (solid line) derived from the motion analyses and divergence derived from the 250 K isotherm expansion (dashed line) plotted versus time (Case I).

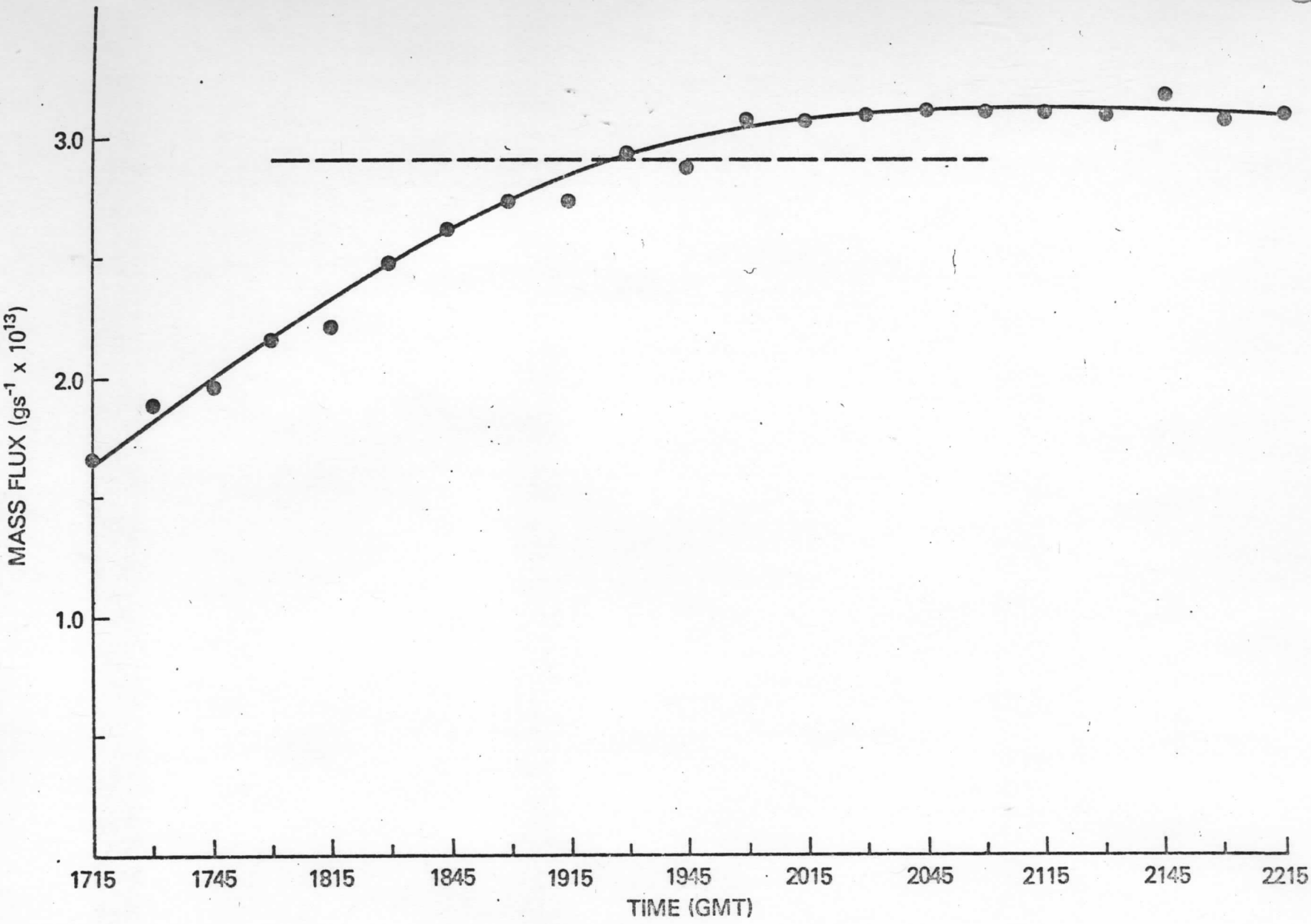

Fig. 6. The total mass flux into the outflow layer as derived by the model (Kinematic method) for Case I plotted versus time. The curve is subjectively drawn. Dash line indicates the mass flux estimate made using the isotherm contour measurements.

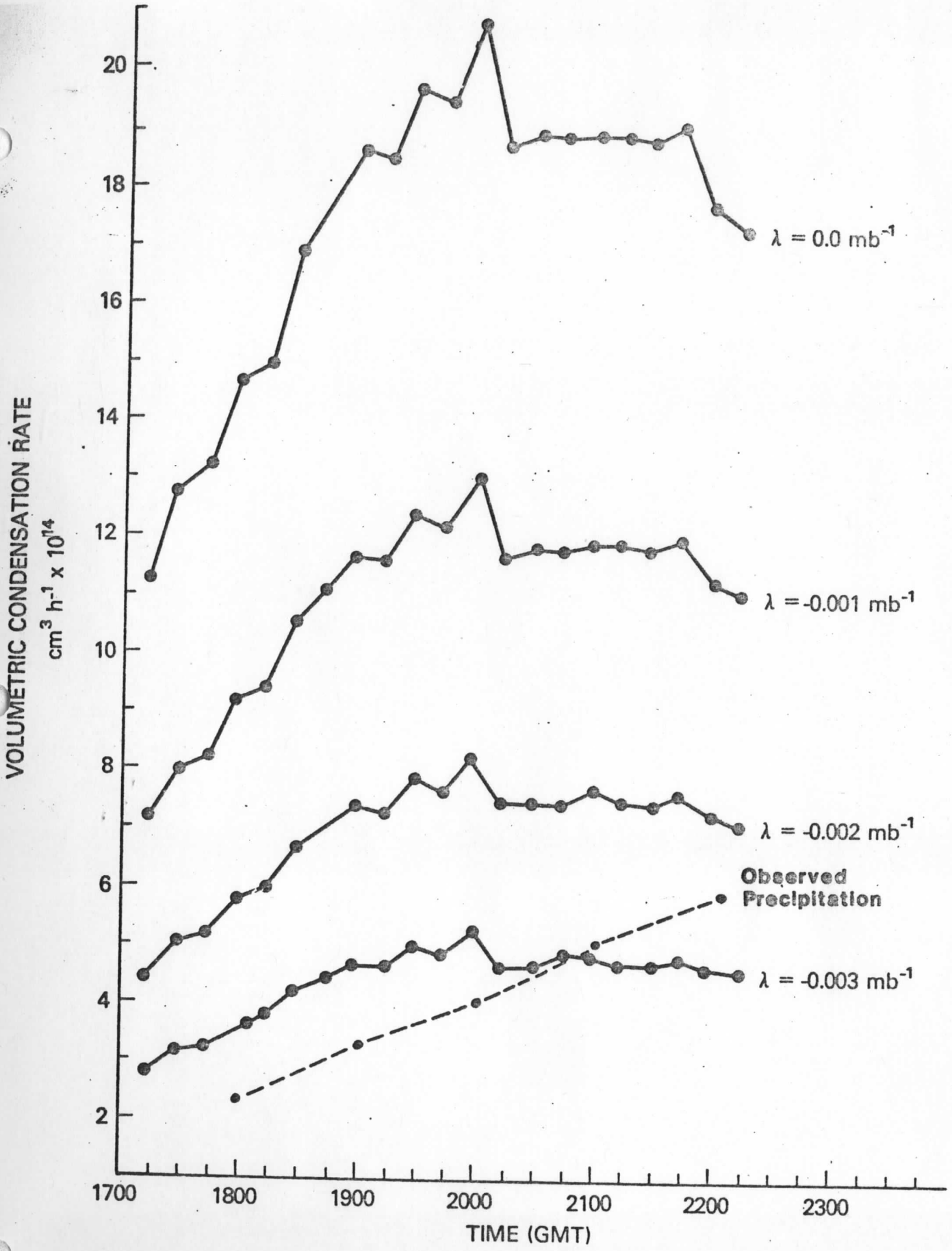

Fig. 7. The volumetric condensation rates produced by the model (Kinematic method only) for four different entrainment rates, λ , plotted versus time (Case I).

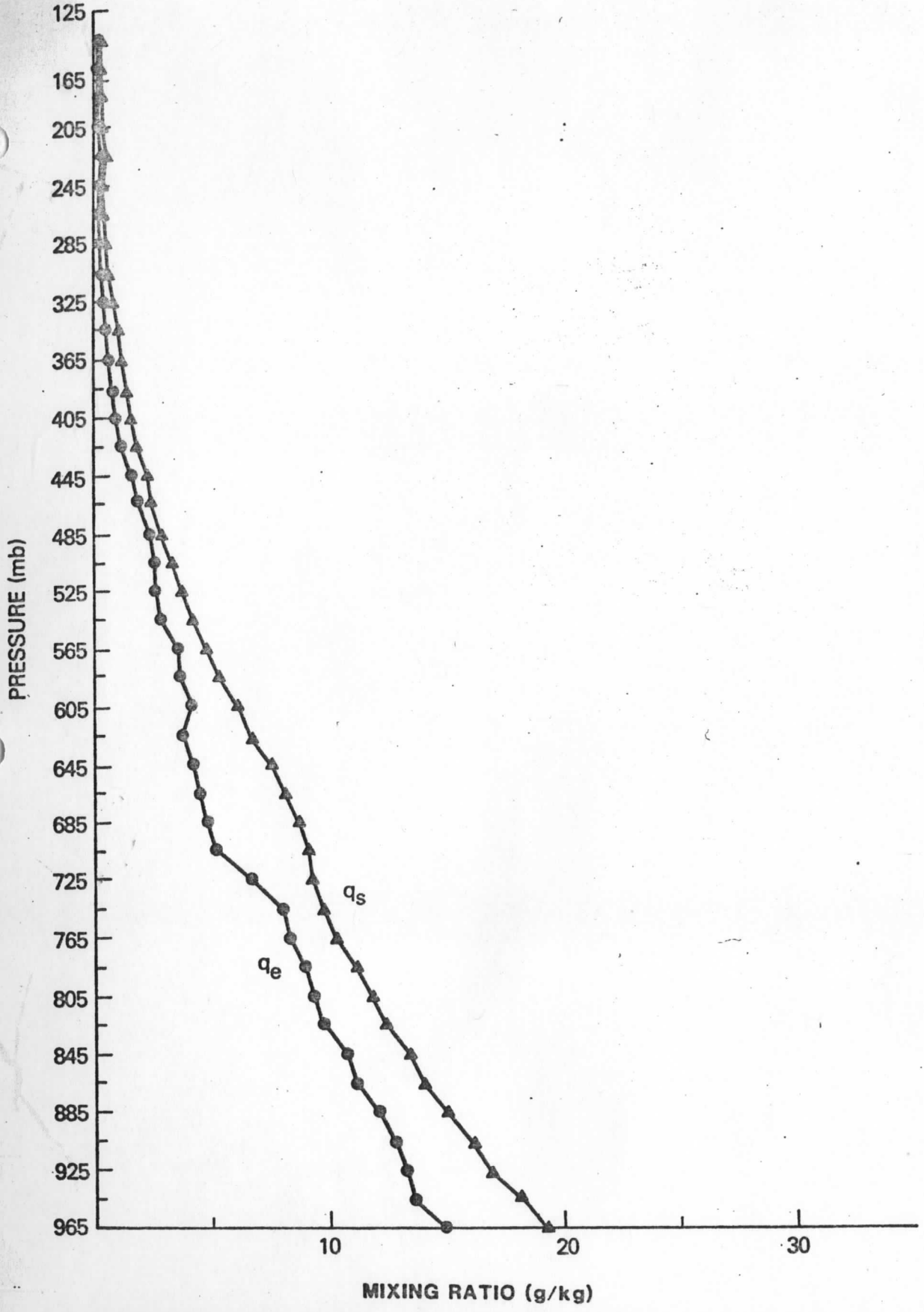

Fig. 8. The average actual mixing ration, q_e, and saturation mixing ration, q_s, for Case I at 2100 GMT.

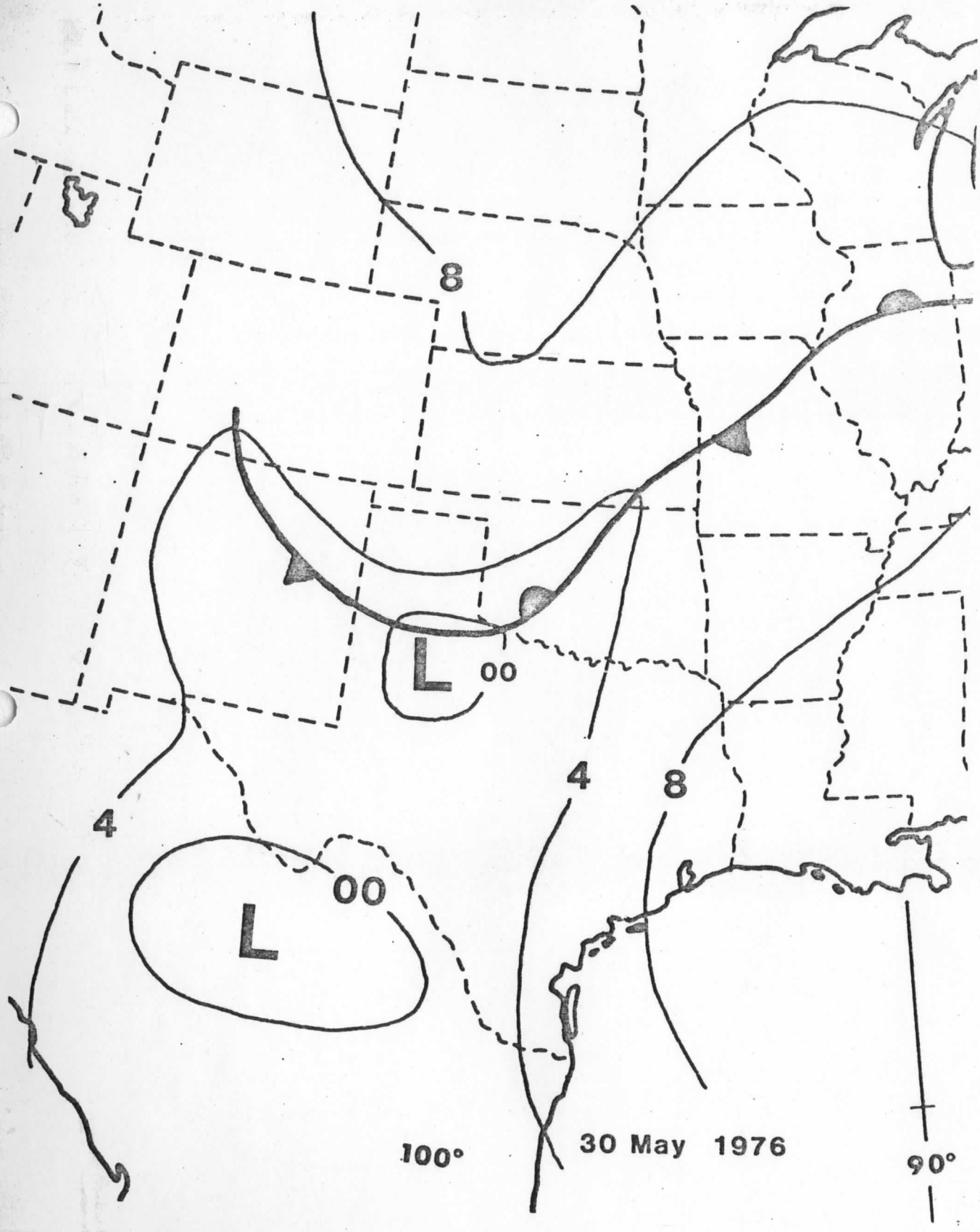

Fig. 9. The 2100 GMT surface map for 30 May 1976 (Case II).

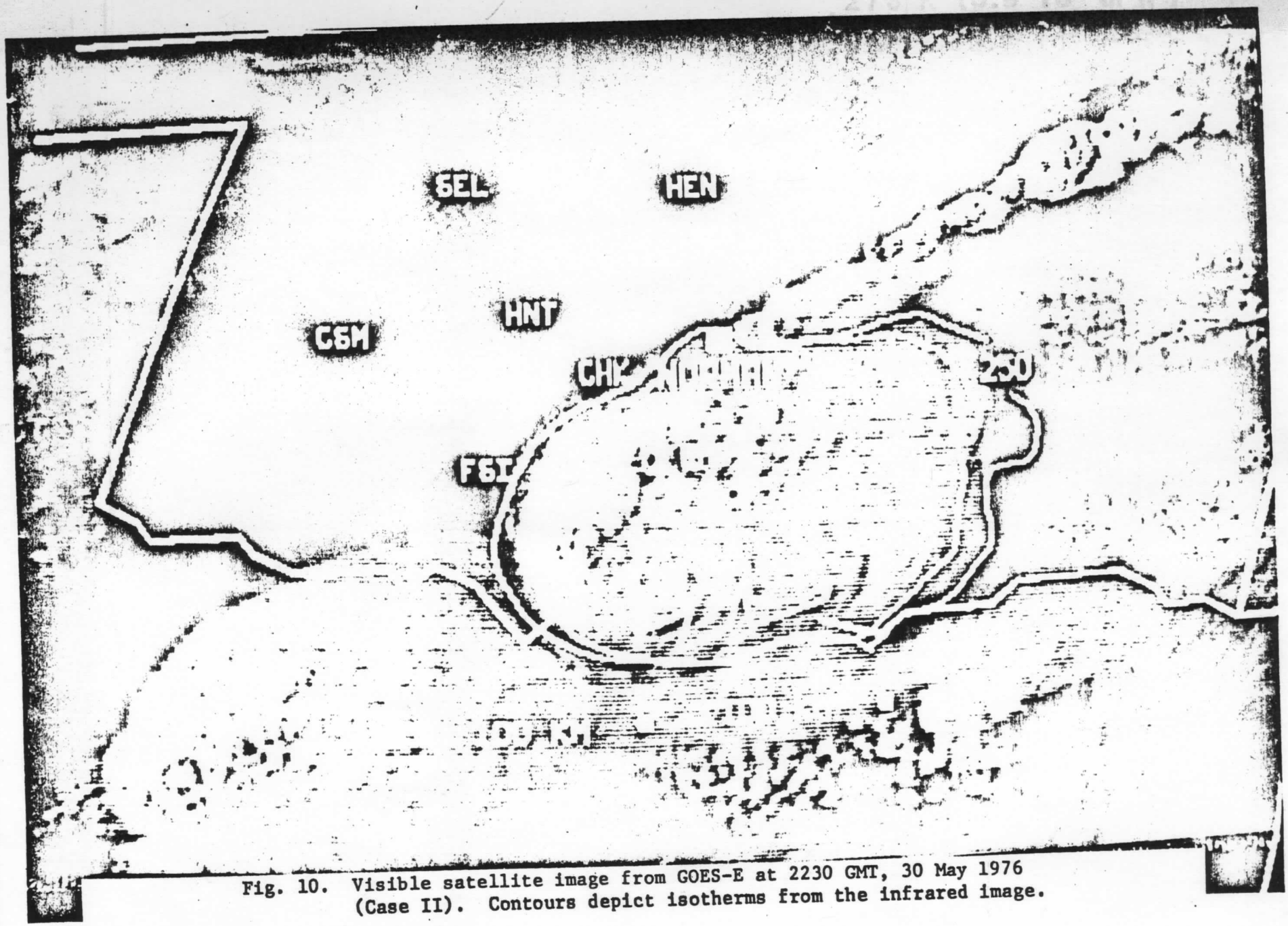

Fig. 10. Visible satellite image from GOES-E at 2230 GMT, 30 May 1976 (Case II). Contours depict isotherms from the infrared image.

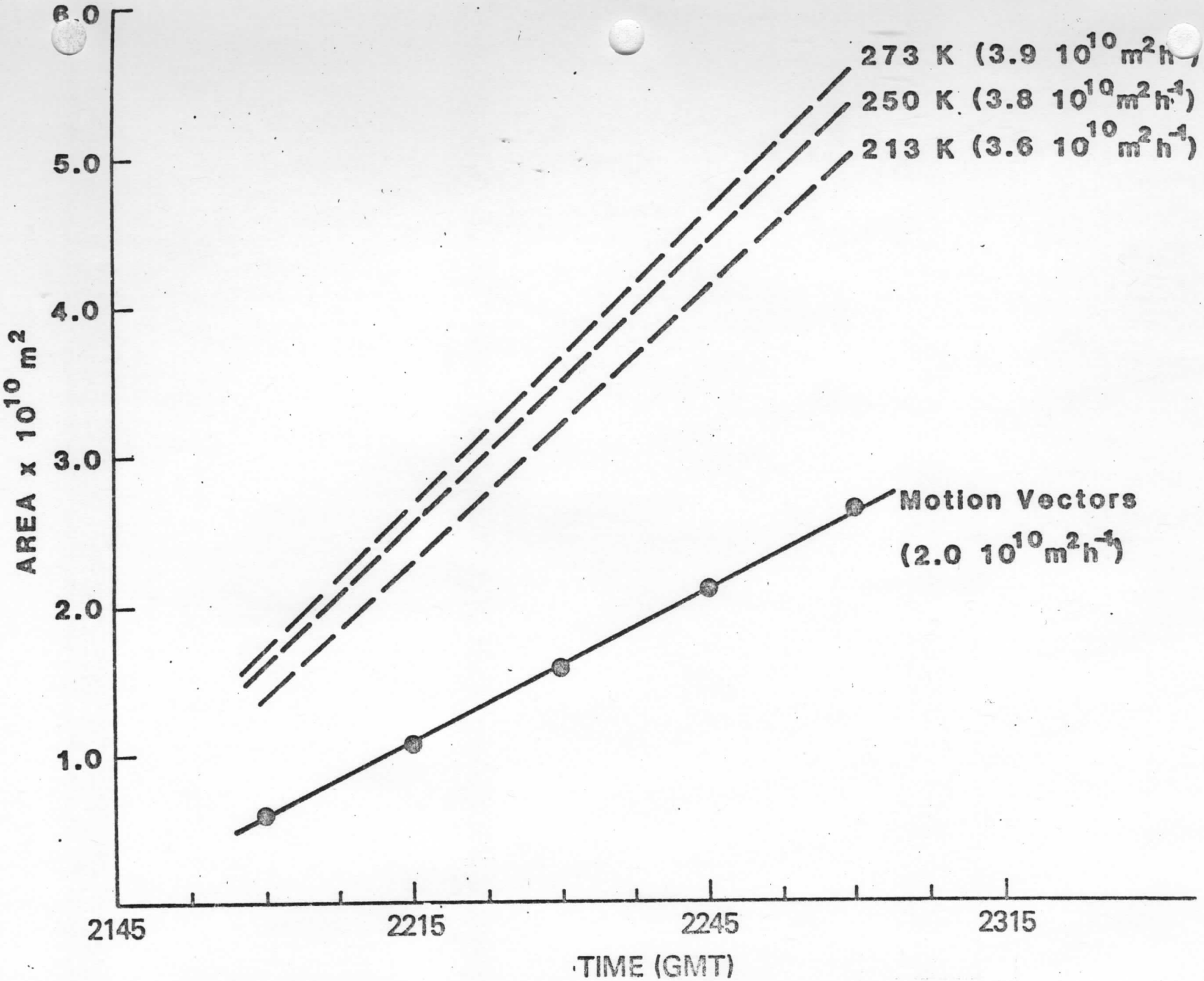

Fig. 11. Cirrus anvil area derived from isotherm expansion (dashed lines) and motion vector positions on the visible image (solid line) plotted versus time (Case II). Areal expansion rates are shown

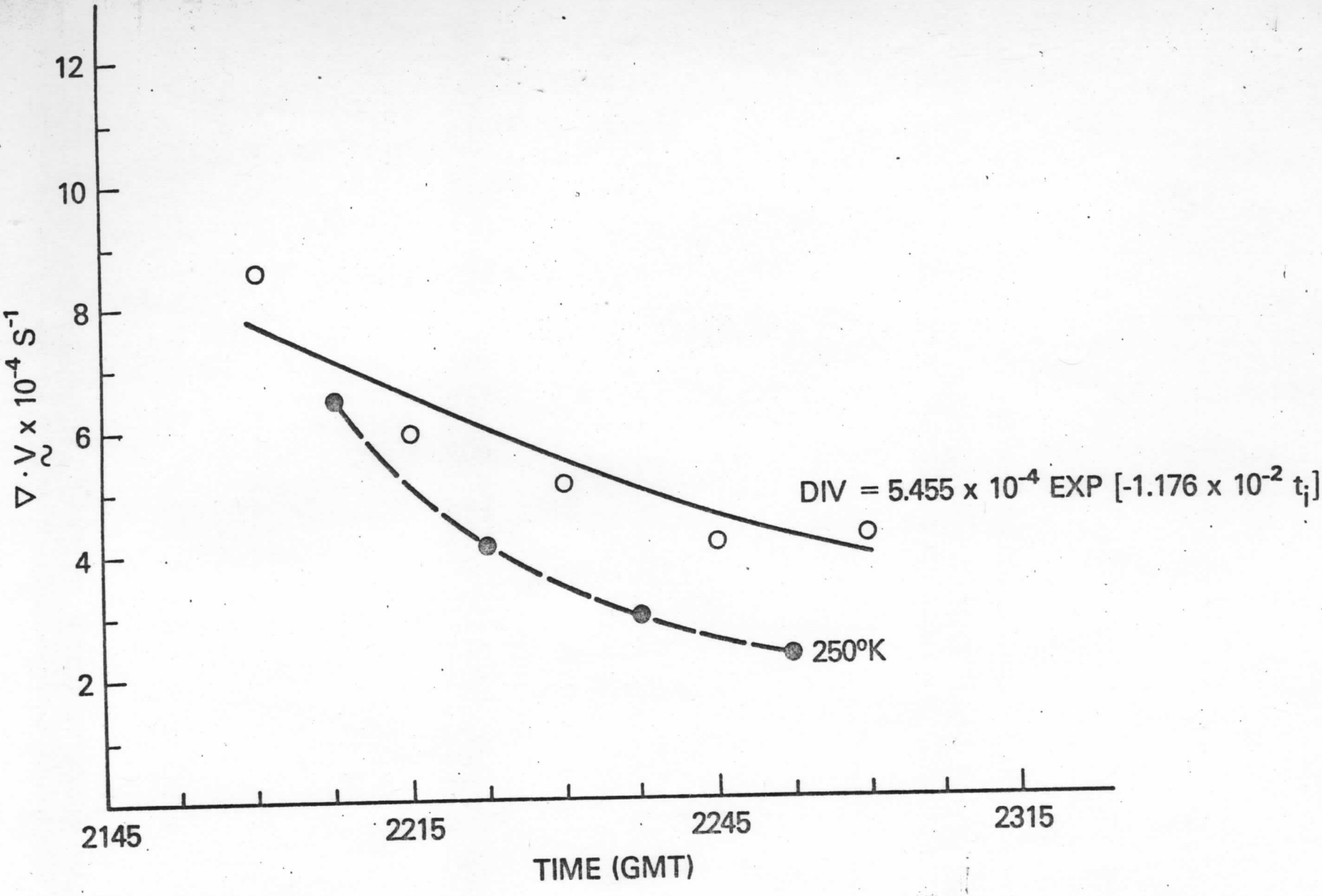

Fig. 12. Kinematic cloud divergence (solid line) derived from the motion vectors and divergence derived from the 250 K isotherm expansion (dashed line) plotted versus time (Case II).

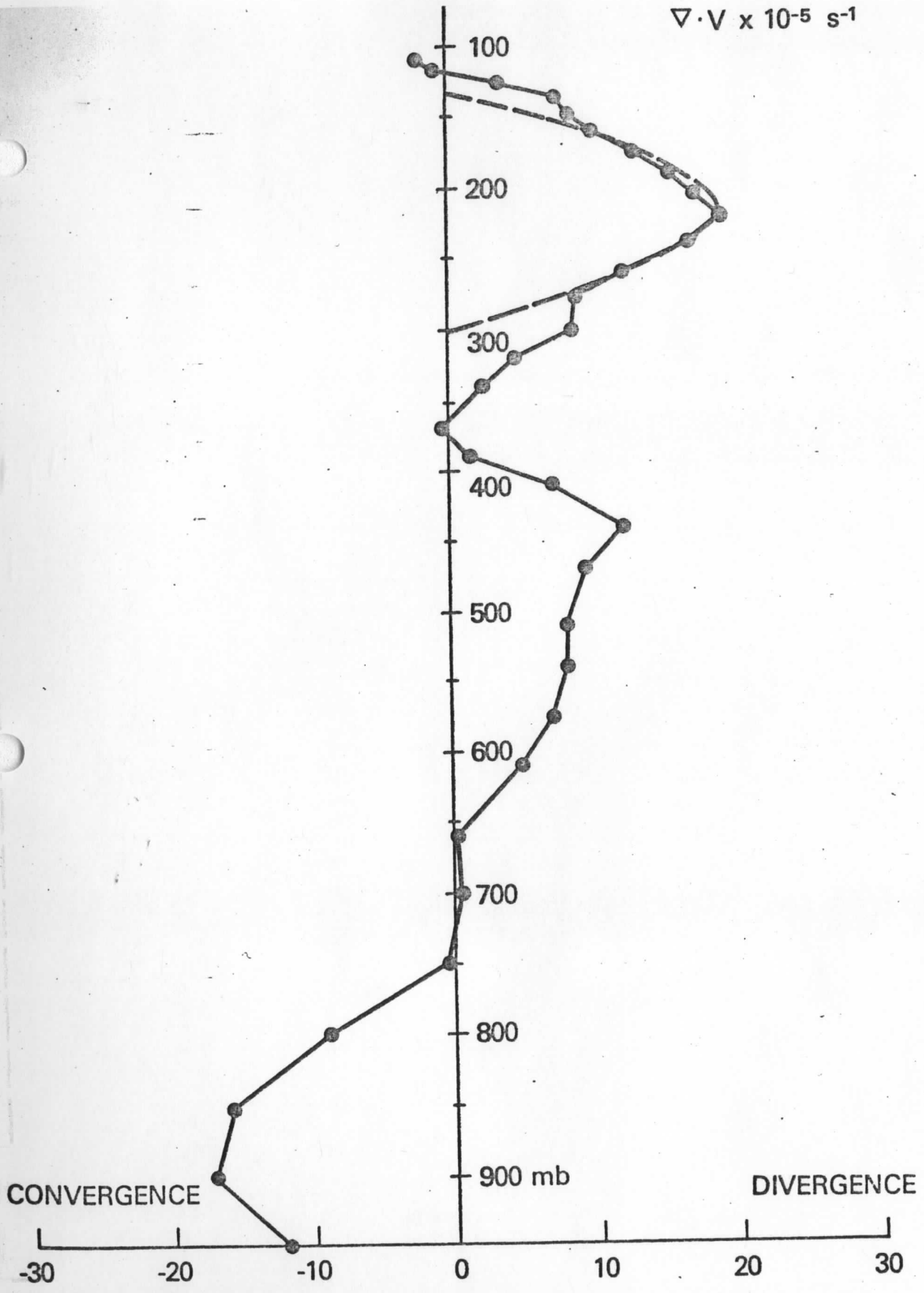

Fig. 13. The vertical profile on environmental divergence derived from soundings from the NSSL network at 2200 GMT on 30 May 1977. Dashed line is smoothed profile.

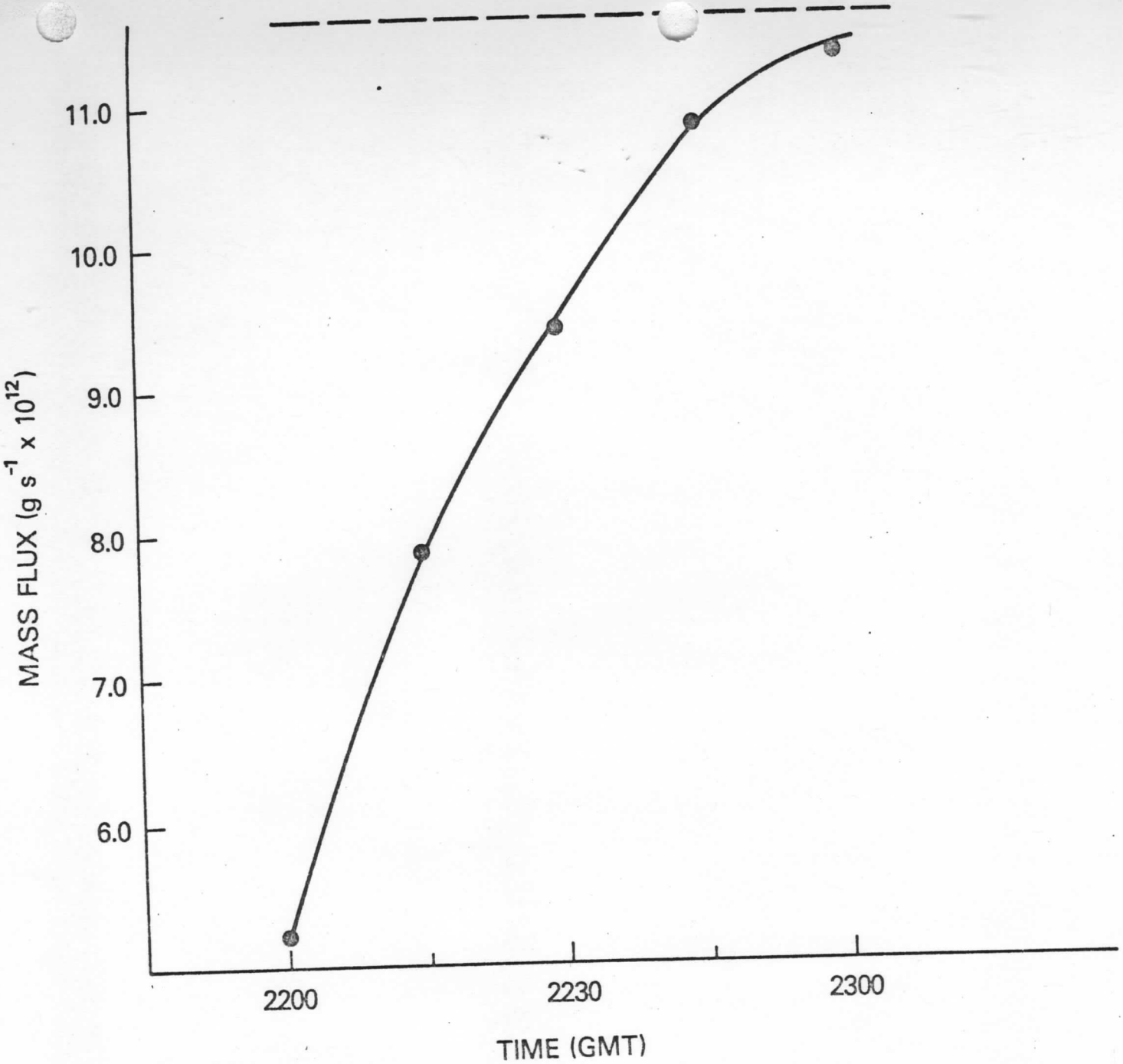

Fig. 14. The total mass flux into the outflow layer as derived by the model for Case II plotted versus time. The curve is subjectively drawn (solid line). Dashed lined indicates the mass flux estimates from the isotherm contour measurements.

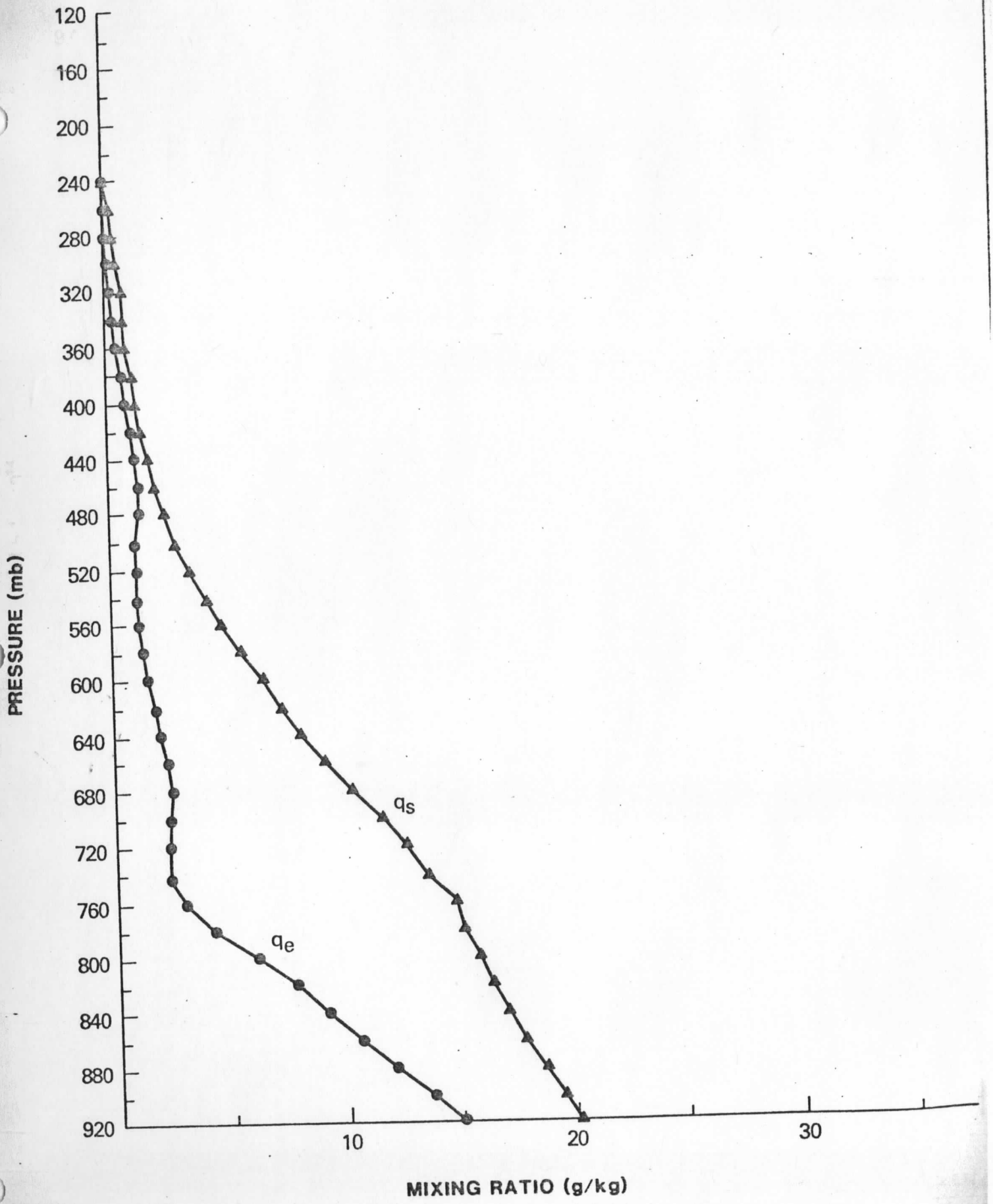

Fig. 15. The average actual mixing ratio, q_e, and saturation mixing ratio q_s, from station EMC at 2230 GMT for Case II.

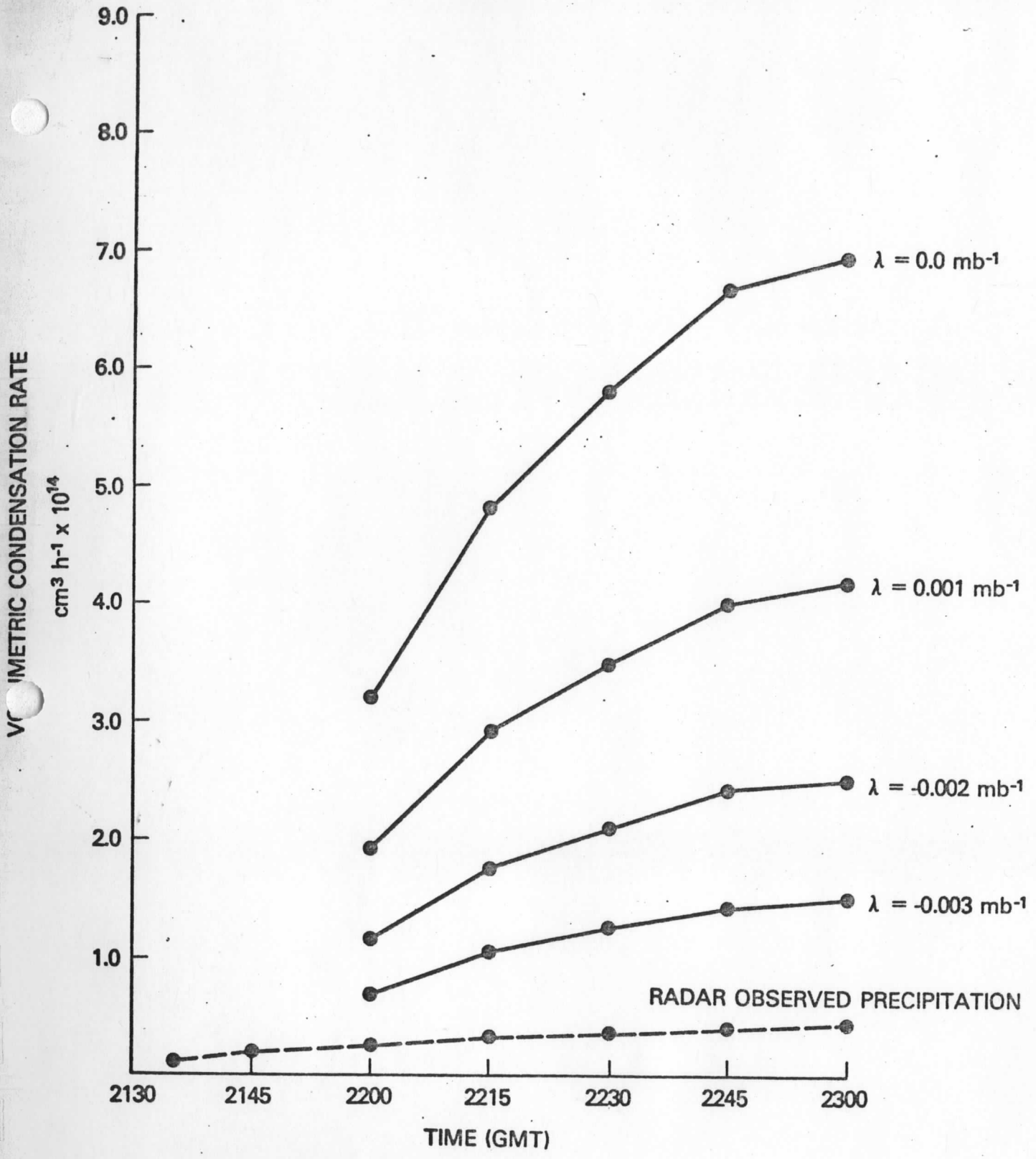

Fig. 16. The volumetric condensation rates produced by the model (Kinematic method) for different entrainment rates and the radar derived volumetric rainfall (dashed line) plotted versus time (Case II).

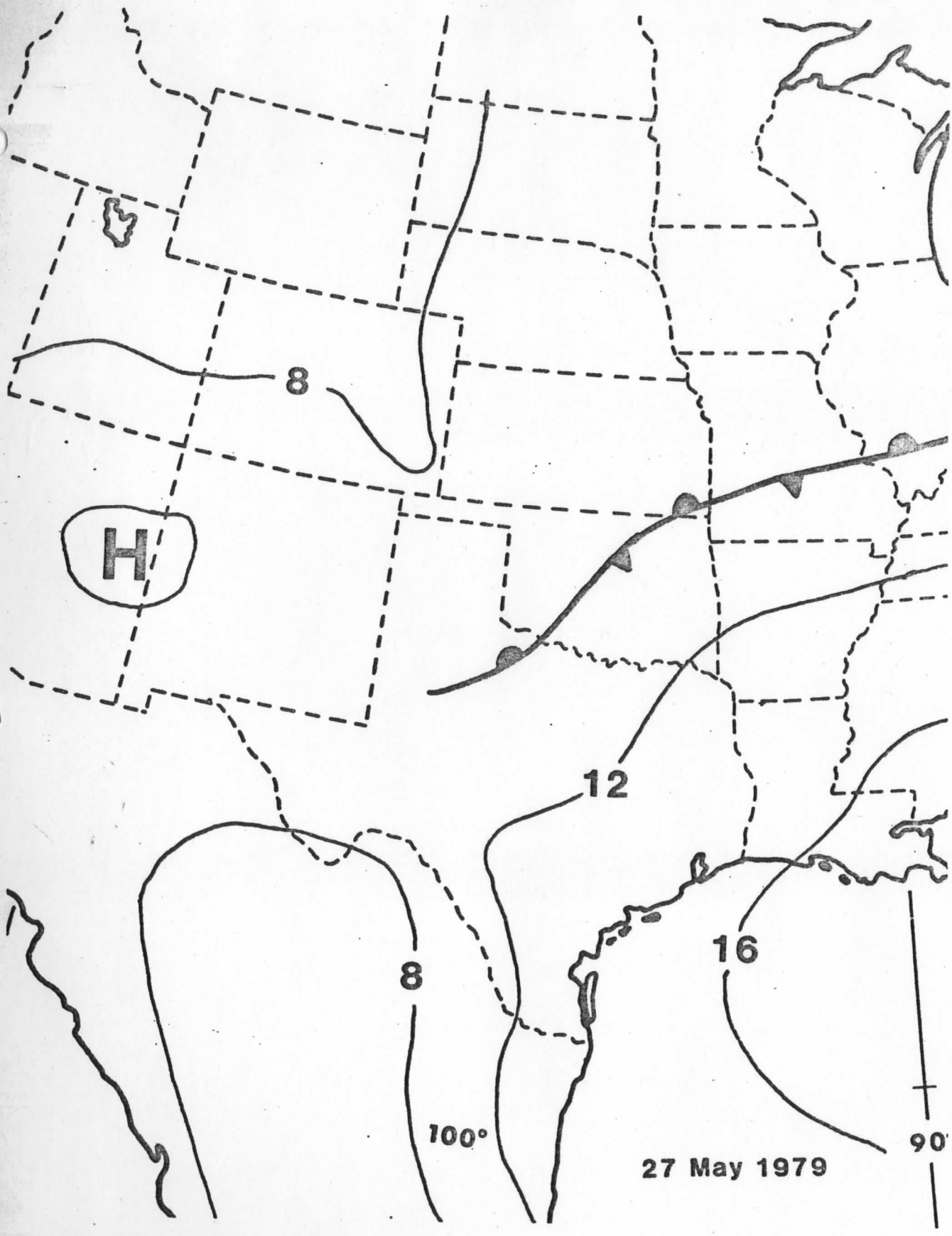

Fig. 17. The 1800 GMT surface map for 27 May 1979 (Case III).

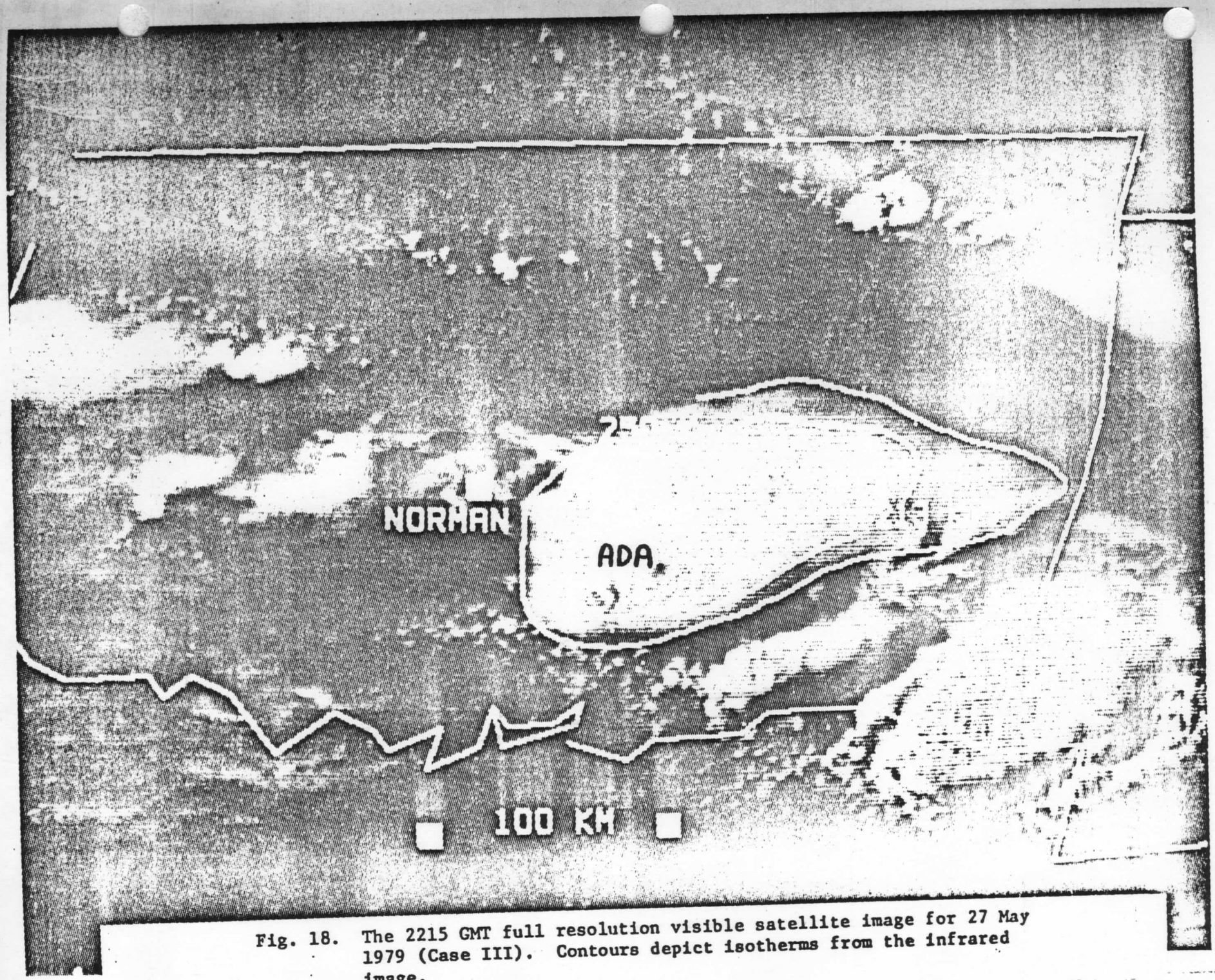

Fig. 18. The 2215 GMT full resolution visible satellite image for 27 May 1979 (Case III). Contours depict isotherms from the infrared image.

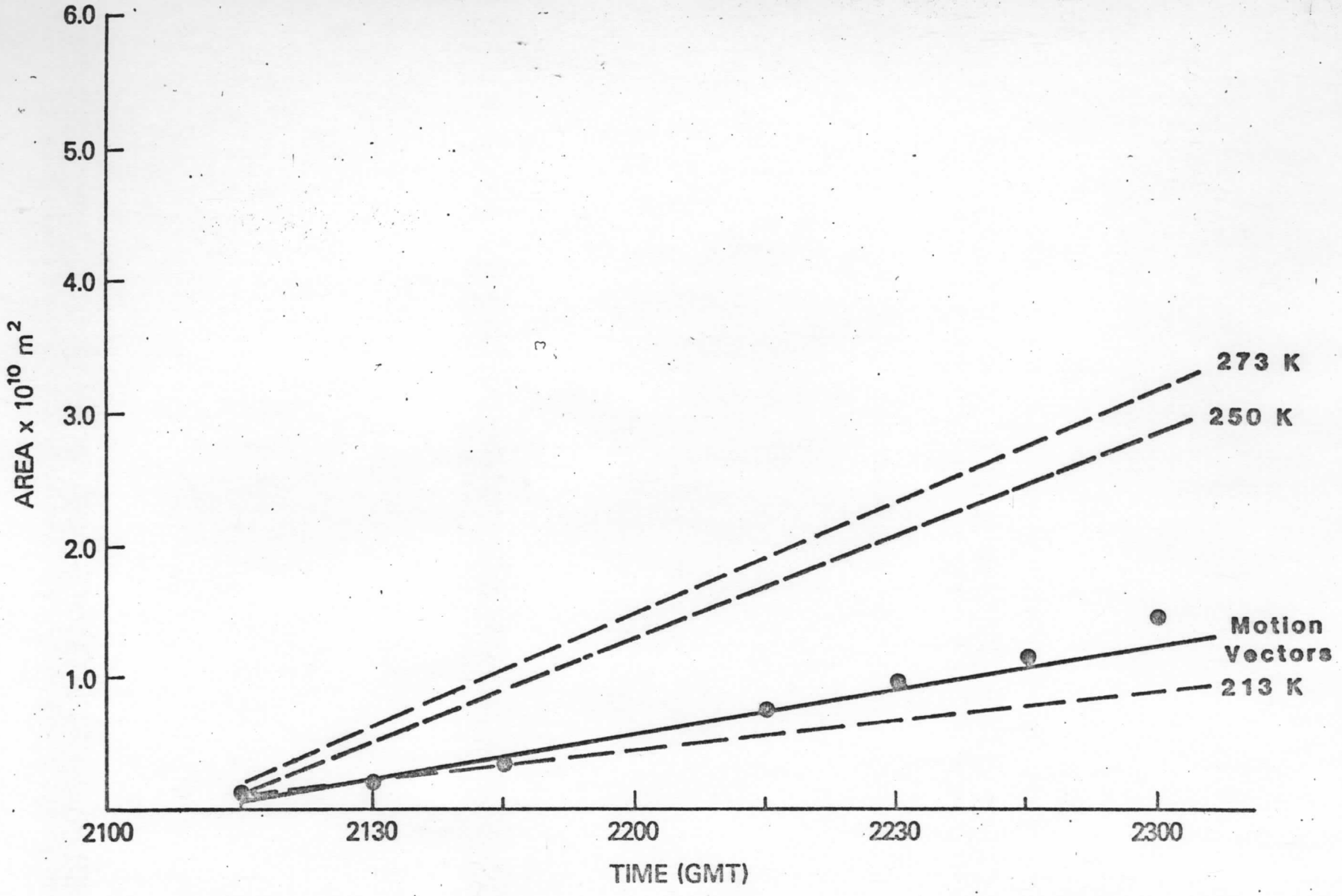

Fig. 19. Cirrus anvil area derived from isotherm expansion (dashed lines) and wind vector positions on the visible image (solid line) versus time (Case III). The rates of areal expansion are shown in ( ).

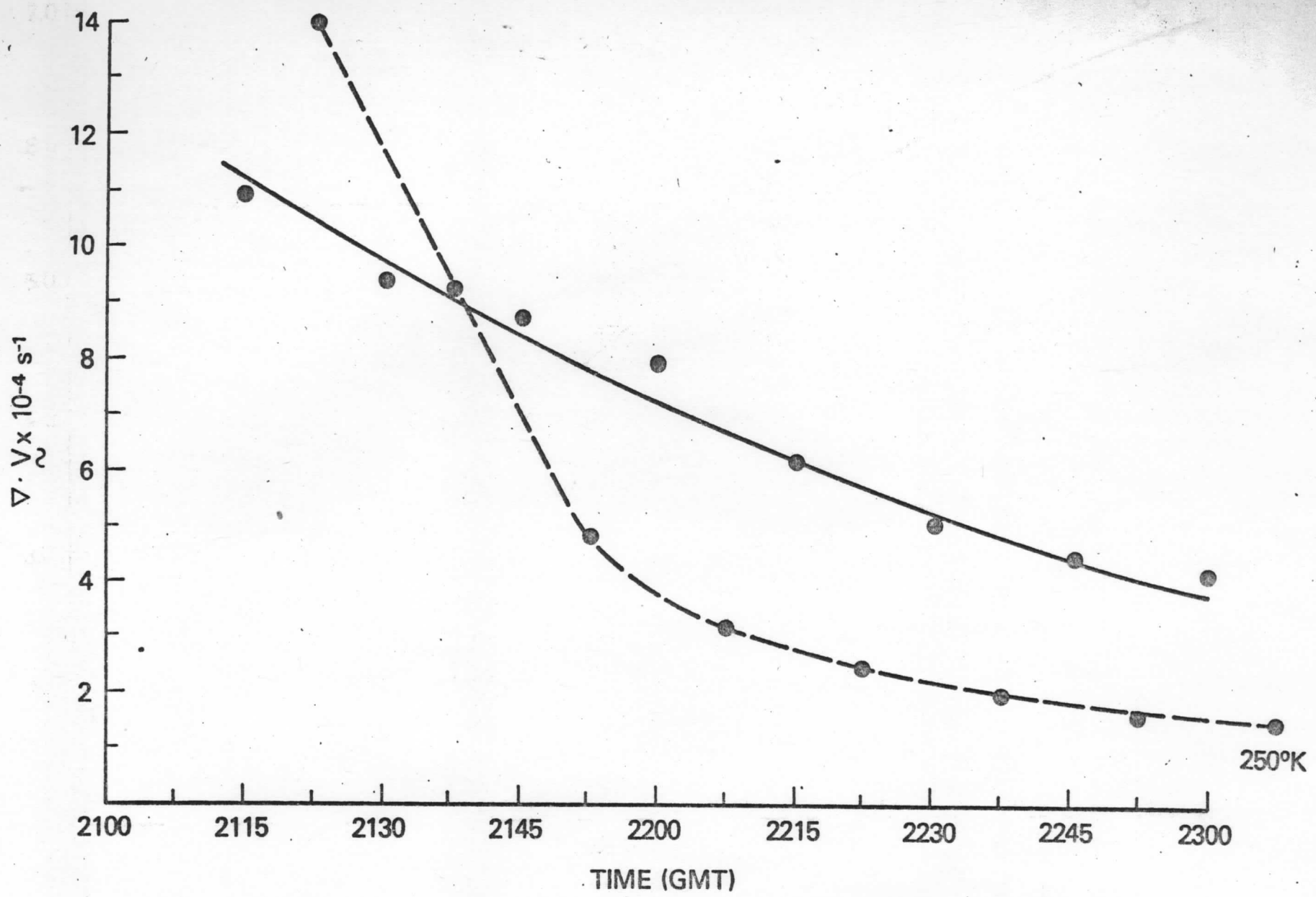

Fig. 20. Kinematic cloud divergence (solid line) derived from the motion measurements and divergence derived from the expansion of the 250 K isotherm (dashed line) plotted versus time (Case III).

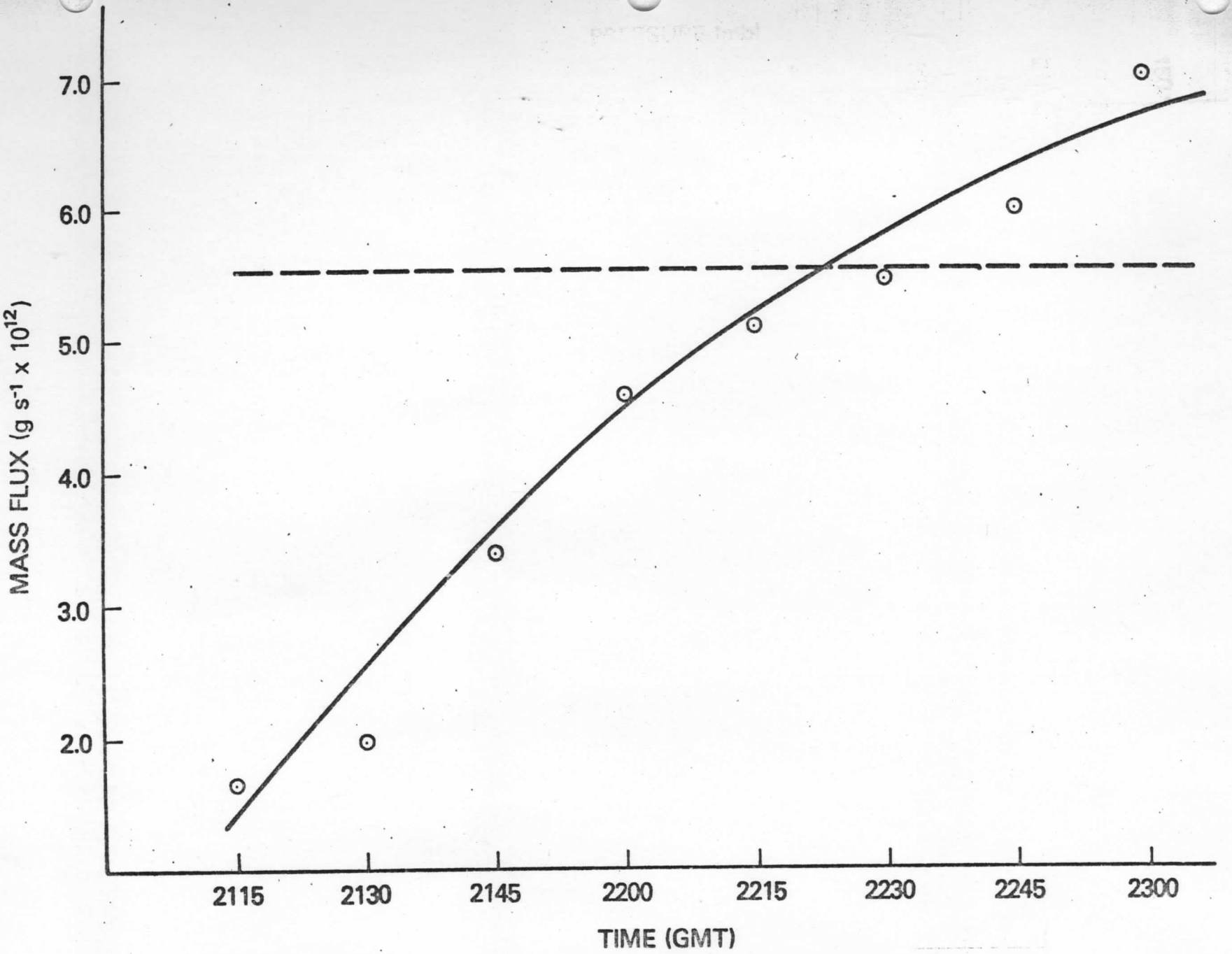

Fig. 21. The total mass flux into the outflow layer as derived by the model (Case III) plotted versus time. The curve is subjectively drawn. Dashed line indicates the mass flux estimated from the isotherm contour measurements.

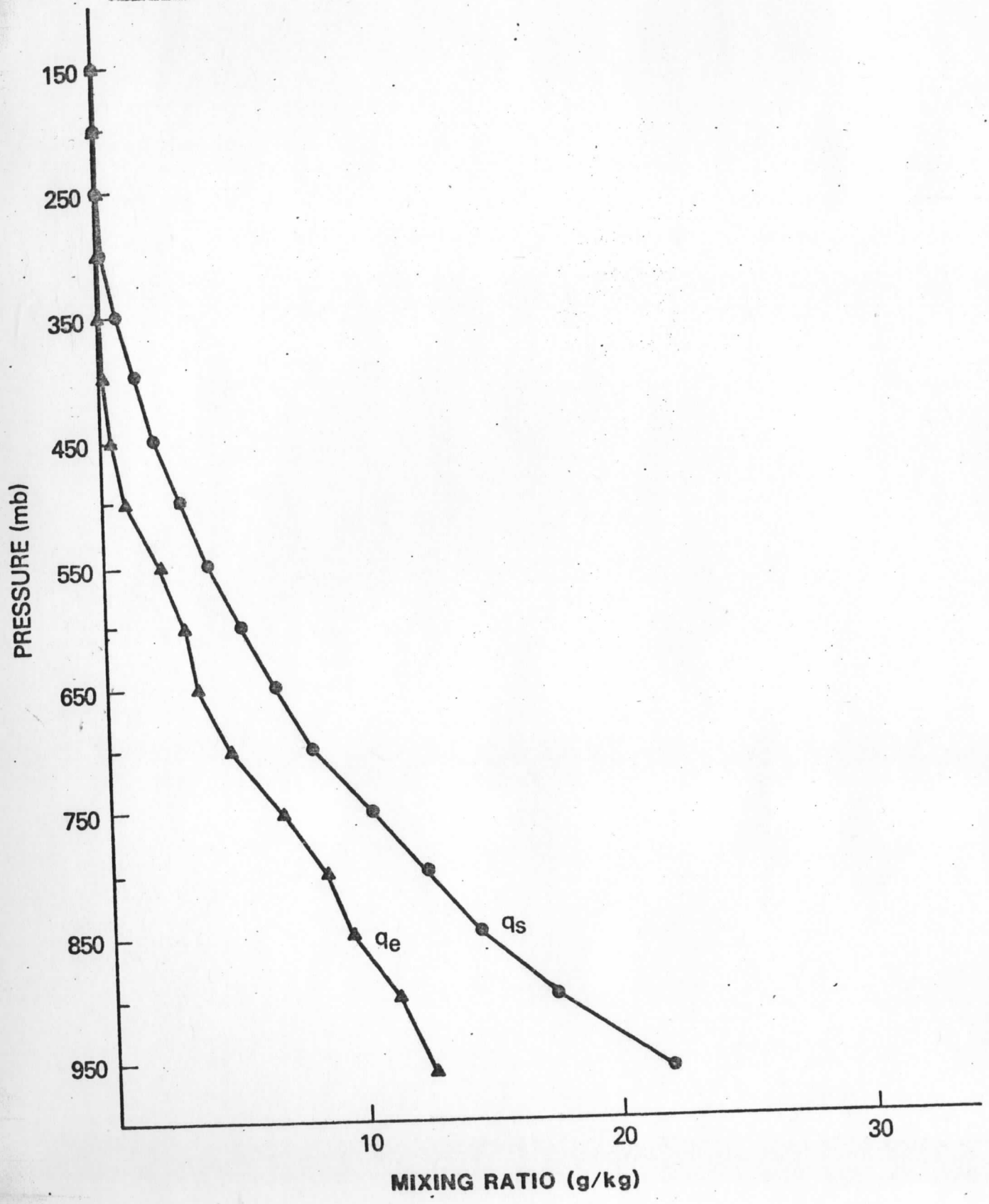

Fig. 22. The average actual mixing ratio, q_e, and saturation mixing ratio , q_s, at 2200 GMT (Case III).

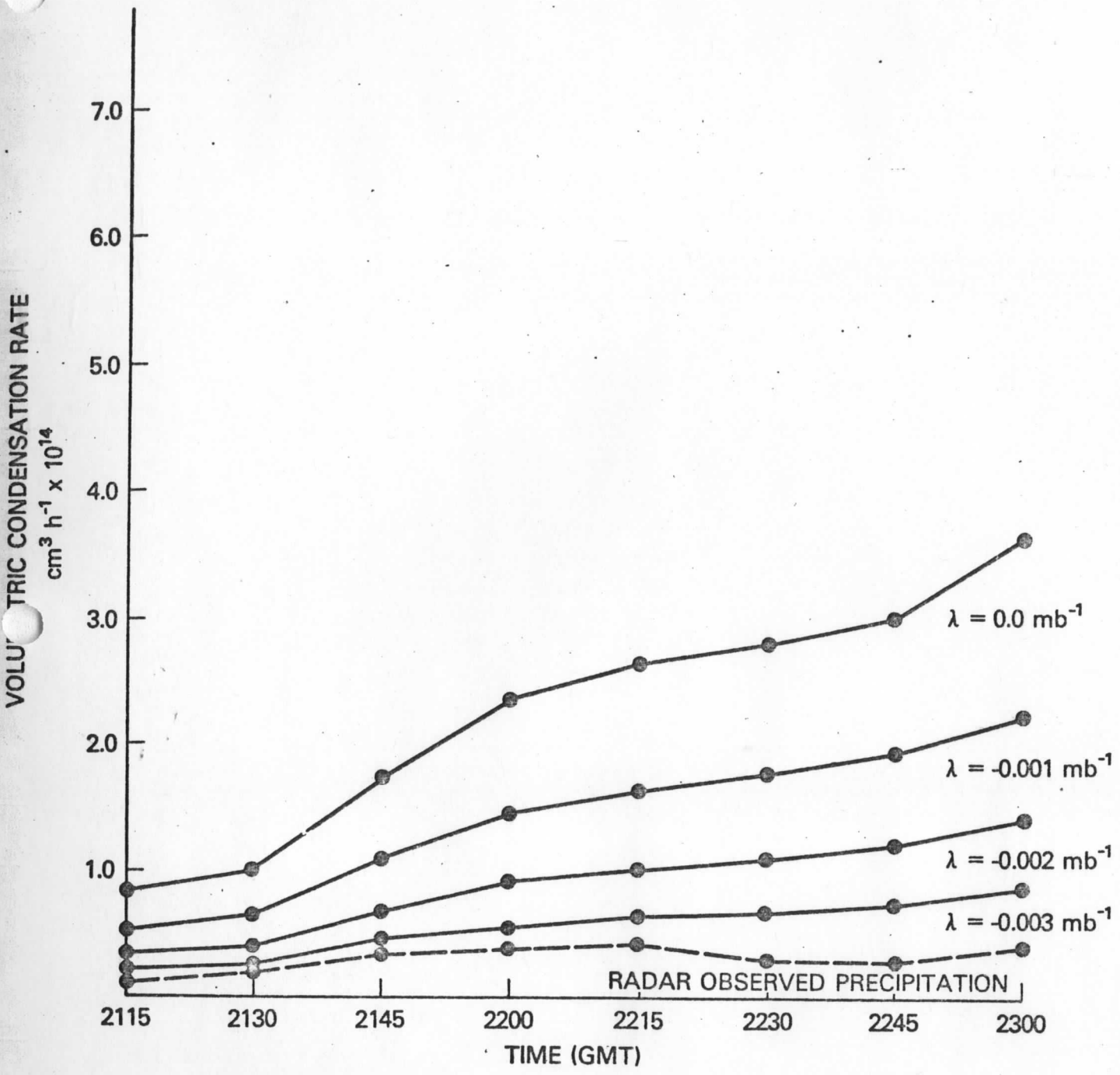

Fig. 23. The volumetric condensation rates produced by the model (Kinematic method only) for different entrainment rates and the radar derived volumetric rainfall (dashed line) plotted versus time.

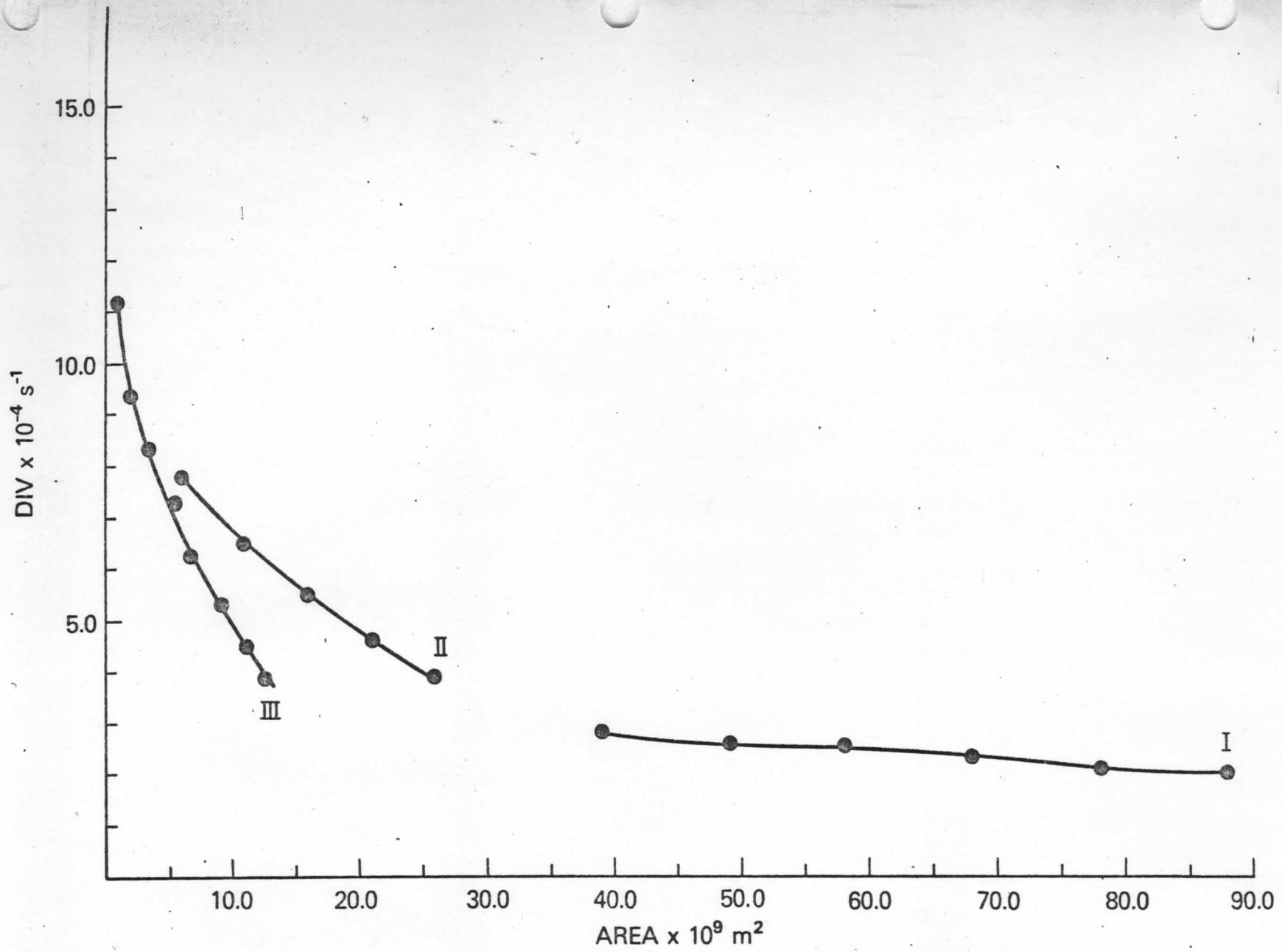

Fig. 24. The divergence derived from the motion vectors for each storm case plotted versus anvil area.

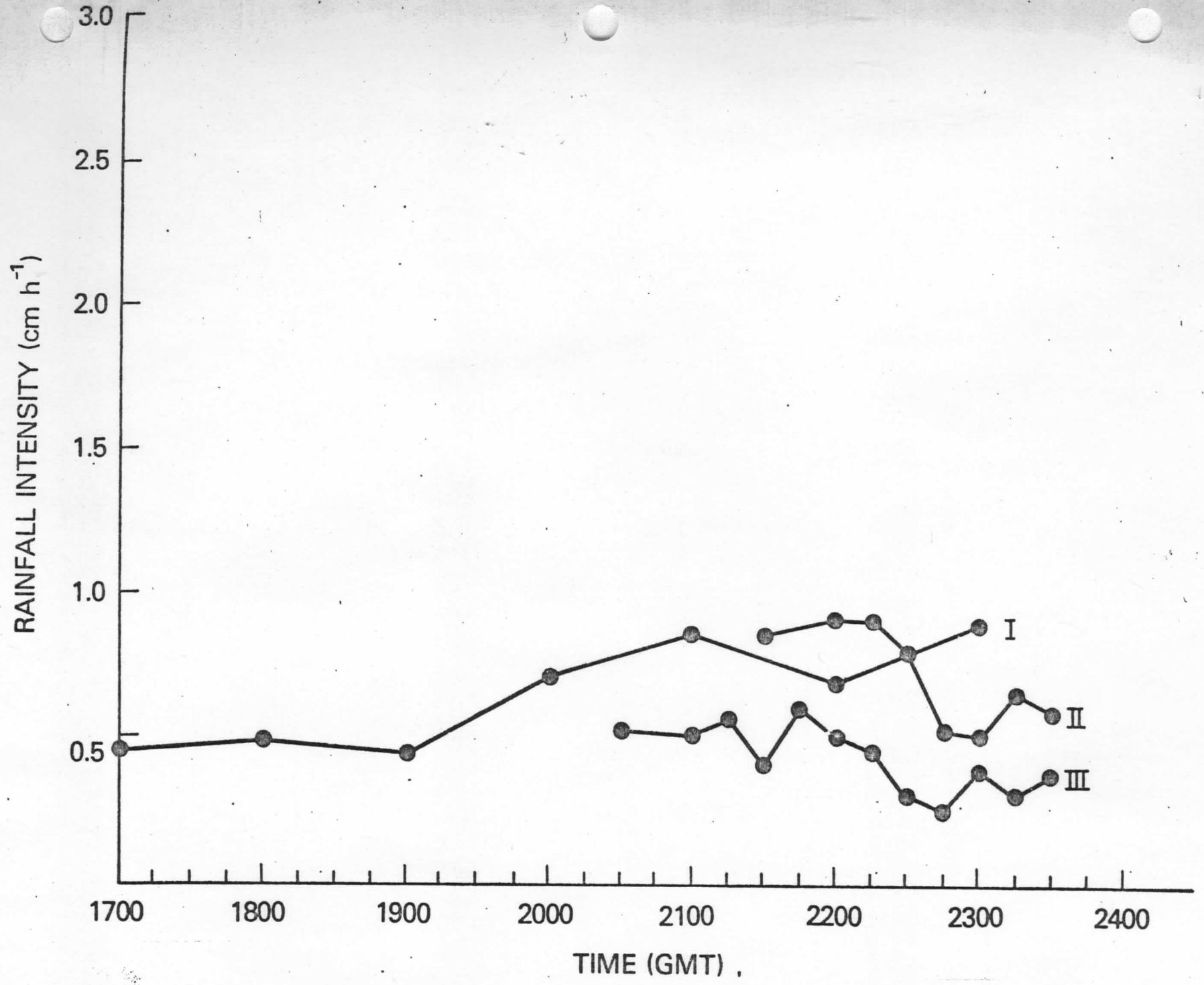

Fig. 25. The rainfall intensities for each storm case plotted versus time. Case I was derived from hourly synoptic rain gauges

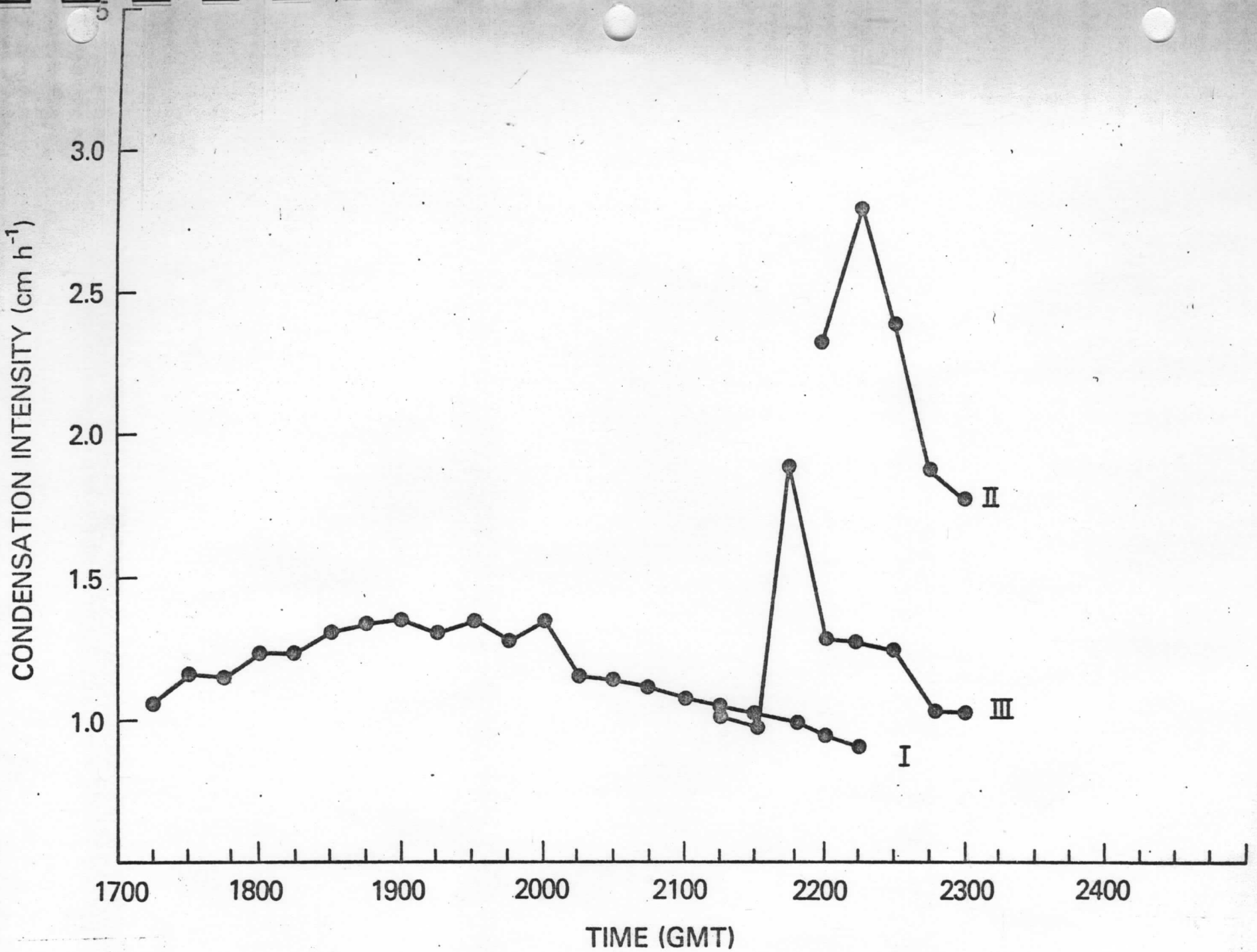

Fig. 26. The condensation rate derived from the model with an entrainment of -0.002 expressed as an intensity (cm hr^{-1}) plotted versus time for each case.